

Interpixel Capacitive Coupling

by

Linpeng Cheng

B.S. Beijing Normal University, Beijing, China (1999)

M.S. Chinese Academy of Sciences, Beijing, China (2002)

A thesis submitted in partial fulfillment of the requirements for the degree of
Master of Science in the Chester F. Carlson Center for Imaging Science
Rochester Institute of Technology

January 2009

Signature of the Author _____

Accepted by _____

Coordinator, M.S. Degree Program

Date

Chester F. Carlson Center for Imaging Science
College of Science
Rochester Institute of Technology
Rochester, New York

Certificate of Approval

M.S. Degree Thesis

The M.S. Degree Thesis of Linpeng Cheng has been examined and approved
by the research committee as satisfactory for the thesis
requirements for the Master Degree in Imaging Science

Dr. Stefi A. Baum, Thesis Advisor

Dr. Donald F. Figer

Dr. Zoran Ninkov

Date

Thesis Release Permission Form

Chester F. Carlson Center for Imaging Science
College of Science
Rochester Institute of Technology
Rochester, New York

Title of Thesis: Interpixel Capacitive Coupling

I, Linpeng Cheng, hereby grant permission to the Wallace Memorial Library of Rochester Institute of Technology to reproduce my thesis in whole or in part. Any reproduction will not be for commercial use or for profit.

Signature of the Author

Date

Interpixel Capacitive Coupling

Linpeng Cheng

A thesis submitted in partial fulfillment of the requirements for the degree of Master of Science in Imaging Science in the Center for Imaging Science, Rochester Institute of Technology

Abstract

Interpixel coupling (IPC) is an electronic crosstalk where a pixel couples signal charges to its neighbors capacitively. It is a deterministic process, whereas diffusion crosstalk is stochastic. It will smooth normal image signal as well as Poisson noise. As a result, the conversion gain will be underestimated by the photon transfer method. However, the capacitive coupling has not received much attention until Andrew Moore and Gert Finger recently studied its potential effect on the measurement of responsive detective efficiency of image detector arrays in both theory and observation.

This thesis continues to investigate this electronic effect. The potential impact of capacitive coupling on the photometric measurement is first simulated. Methods based on inverse filter and Wiener filter are tested to correct this coupling impact. It appears that the signal loss can be restored to reasonable accuracy by applying the pseudo-inverse filter, provided that we have full knowledge of interpixel coupling.

New methods to measure the IPC value are proposed and tested based on the cosmic ray events and hot pixels, where the dark frame data sampled up-the-ramp are used. By these two methods, the coupling effect of a hybrid HgCdTe array is studied. The coupling magnitude is measured at different detector temperatures. It shows that the IPC magnitude decreases with increasing temperature. The IPC dependencies on the center pixel intensity and background are also checked: the magnitude becomes smaller when the target pixel event gets stronger, while the trend reverses with the change of

background level. Finally, the possible impact on read noise, i.e. noise correlation with adjacent pixels, is examined based on the dark frames from the infrared HgCdTe and Si-PIN arrays. The initial results indicate that the read noise component is not affected by the capacitive coupling between pixels, in the sense that read noise is uncorrelated to neighboring pixels, as compared to the neighbor-correlated Poisson noise due to interpixel capacitance.

Acknowledgements

My graduate study in Center for Imaging Science includes some of the most fun and valuable times in my life. I am very happy to the opportunity to learn imaging-related knowledge and skills with the help and encouragement of many people.

First, I would like to thank my advisors, Dr. Stefi Baum and Dr. Don Figer, for their careful guidance and inspiring advice. They envisioned a great research project, taught me the skills I needed to complete my M.S. degree. Thanks also go to my committee member, Dr. Zoran Ninkov, for his patient discussion and helpful suggestions in my research.

I would also like to thank my parents and girl friend for their care and support. I could not come to this point without their unselfish support materially and spiritually.

I would like to thank all the people at Rochester Image Detector Laboratory (RIDL). Thanks to you all for the good times and suggestions. A special note of thanks goes to Brandon, Qingfeng. Final thanks go to NASA JWST NIRCAM team for the financial support through grant NAS5-02105. It has been a very valuable experience.

TABLE OF CONTENTS

1	Background	1
1.1	Monolithic CMOS array	2
1.2	Hybrid CMOS array	5
1.3	Crosstalk	8
1.3.1	Optical crosstalk	8
1.3.2	Diffusion	10
1.3.3	Interpixel capacitive coupling	13
1.3.4	Basic mechanism of interpixel capacitance	18
2	Methodology on the measurement of interpixel coupling	24
2.1	Autocorrelation	25
2.2	Optical spot illumination (Spotomatic)	26
2.3	Single pixel reset	28
2.4	F55 bombardment	29
2.5	Reset bias V_{reset}	30
2.6	Cosmic ray event (CRE)	31
2.7	Hot pixels	34
3	Impact of IPC on astronomical photometry	36
3.1	Photometry in astronomy	36
3.2	Modeling IPC's impact on photometry	39
3.3	Simulation of the impact of IPC on photometry	40
3.4	Simulation of the impact of IPC on SNR	46
3.5	Summary	49
4	Interpixel coupling and read noise	51
4.1	Read noise	51
4.2	Modeling of read noise and IPC	52
4.3	Autocorrelation of read noise	55
4.4	Summary	65
5	Variations of interpixel capacitance	67
5.1	Capacitor and capacitance	68
5.2	Identification of cosmic ray events and hot pixels	72
5.3	IPC dependency on temperature	74
5.3.1	Data analysis and results	74
5.3.2	Discussion	79
5.4	IPC dependency on single event intensity	81
5.4.1	Overview	81
5.4.2	Data analysis and results	82
5.4.3	Discussions	87
5.5	IPC dependency on background	90
5.5.1	Data analysis and results	90
5.5.2	Discussion	97
5.6	Summary	98
6	Summary and conclusions	100

6.1	Summary	100
6.2	Conclusions	101
6.3	Future research	103
Appendix A: Convolution and deconvolution		104
A.1	Linear shift-invariant system	104
A.2	Convolution.....	106
A.3	Filtering theorem.....	107
A.4	Deconvolution: inverse and Wiener filters	108
Appendix B: Sampling techniques in astronomical imaging.....		112
B.1	Correlated double sampling	112
B.2	Fowler sampling.....	113
B.3	Up-the-ramp sampling	114
Bibliography		116

LIST OF FIGURES

Figure 1.1 Left: cross section of a MOS capacitor (buried channel); right: p-n junction photodiode.....	3
Figure 1.2 Architecture of monolithic CCD image sensors.....	4
Figure 1.3 Sense node (photodetector) and the associated readout components in CMOS sensors. Left: photodiode (3T); right: Pinned photodiode or photogate (4T).....	4
Figure 1.4 Architecture of monolithic CMOS image sensor.....	5
Figure 1.5 Cross section of typical IR hybrid CMOS detectors (per-pixel depleted) and Si multiplexer.....	6
Figure 1.6 Cross section of Si-PIN detector array and associated the Si multiplexer.....	8
Figure 1.7 A simple illustration of optical crosstalk occurring in image detectors. Photons incident on a target pixel finally may be absorbed in the neighbors due to inclined incident angle, multi-reflections, refraction in the image sensor, etc.....	9
Figure 1.8 Illustration of diffusion crosstalk occurring in FSI image detectors.....	11
Figure 1.9 Illustration of diffusion crosstalk occurring in BSI image detectors.....	11
Figure 1.10 Absorption depth of photons in Si at different wavelengths. Absorption depth is defined as the distance where the incident radiation is reduced by 1/e (Bruggemann et al. 2002).....	12
Figure 1.11 Capacitive coupling in more typical per-pixel depleted detectors occurs in the space between the multiplexer and detectors between In bumps.....	14
Figure 1.12 Major coupling in fully depleted detectors occurs in the detector bulk, in addition to the coupling in the space between the detectors and multiplexer.....	15
Figure 1.13 Sketch of electric fields in detector arrays from top view (left: HgCdTe; right: Si-PIN). White area denotes regions with electric fields and is free of charge carriers. Shaded areas are p or n type regions of equal potential. Depletion regions in HgCdTe arrays are separated by conducting n-type detector bulk. The bulk of Si-PIN array is fully depleted with capacitive coupling between pixels inside the photodiode array.....	15
Figure 1.14 Layout of detector nodes and interpixel capacitance. Photocurrent enters a detector node $C_{0,0}$, which collects photocharges. The signal can still appear on adjacent nodes that are not exposed to photons (Moore et al. 2006).....	20
Figure 2.1 A sample image of an optical spot projected onto the detector (left) and the surface plot of the pixel levels around the optical spot.....	27
Figure 2.2 A portion of a frame illuminated by the Fe55 X-ray source with Al foil attenuation.....	30
Figure 2.3 Right: Up-the-ramp readouts for a typical pixel (plus sign); right: histogram	

mode.....	32
Figure 2.4 Left: up-the-ramp samplings for a typical pixel hit by CRE (histogram mode); right: Pixels around the pixel hit by CRE in a difference frame.....	33
Figure 3.1 Illustration of aperture photometry for an astronomical object.....	37
Figure 3.2 Illustration of photometric image suffering from interpixel coupling.....	39
Figure 3.3 Workflow of the simulation process.....	41
Figure 3.4 Left: image of ideal airy pattern; right: image of re-sampled airy pattern with a size of 19×19 pixels (zoomed in).....	42
Figure 3.5 Comparison of signal change after the inverse and Wiener filters are applied. Relative signal change after deconvolution is referred to signal without IPC, i.e. F3 to F1_rd.....	43
Figure 3.6 Relative signal change in the aperture at different input signal levels after inverse filter was applied. Seven deconvolution kernels of different coupling amounts were tried at each input signal levels, including the true IPC. Relative signal change after deconvolution is referred to the signal w/o the IPC effect, i.e. F3 to F1_rd. See flowchart for descriptions.....	45
Figure 3.7 Comparison of SNR change after applying the inverse and Wiener filters. Relative SNR change after deconvolution is referred to signal w/o IPC, SNR3 to SNR1_rd.....	47
Figure 3.8 Relative SNR change at different signal levels after inverse filter was applied. Relative SNR change after deconvolution is referred to signal w/o IPC, SNR3 to SNR1_rd.....	49
Figure 4.1 Left: autocorrelation of an ideal Gaussian noise image with zero mean and σ = 5 DN; right: autocorrelation of same noise image but convolved with a low-pass filter.....	54
Figure 4.2 A mean-subtracted bias frame from the dark experiments of H2RG IR array at 37 K. The regions chosen are [140:500, 1070:1325], [520:1015, 1100:1380], [1025:1545, 1400:1680], and [1550:1980, 830:1180], as shown by the boxes.....	56
Figure 4.3 2-D autocorrelation of mean-subtracted bias, data taken from H2RG IR, regions of good uniformity used. Same dataset as in Figure 4.2.....	57
Figure 4.4 1-D autocorrelation of individual mean-subtracted columns. The resulting functions were averaged and scaled to 100 in the center. Test image data are from H2RG IR array. Same dataset as in Figure 4.2.....	58
Figure 4.5 1-D autocorrelation of individual mean-subtracted rows. The resulting functions were averaged and scaled to 100 in the center. Test image data are from H2RG IR array. Same dataset as in Figure 4.2.....	59
Figure 4.6 A mean-subtracted bias frame: patch of good uniformity chosen chosen, from H4RG Si-PIN array taken at 110 K. The regions chosen are [2560:2688, 2425:2690],	

[2690:2815, 2535:2695], [3840:3970, 2720:2900], [3970:4095, 2720:2900], and [3460:3584, 2445:2660], as marked by the boxes.	61
Figure 4.7 2-D autocorrelation of mean-subtracted bias, data taken from H4RG SiPIN array, regions of good column bands used.	62
Figure 4.8 1-D autocorrelation of individual mean-subtracted columns. The resulting functions were averaged and scaled to 100 in the center. Test image data are from H4RG Si PIN array.	63
Figure 4.9 1-D autocorrelation of individual mean-subtracted rows.	64
Figure 5.1 Illustration of photodiode capacitance (C_0) and interpixel capacitance (C_c) (Bai et al. 2007).	68
Figure 5.2 Pixel node capacitance C_0 and interpixel capacitance C_c . Only nearest neighbors are considered.	71
Figure 5.3 IPC variation with the detector temperature. Data taken at temperature ranging from 27.7K to 50 K. IPC is measured through cosmic ray events.	76
Figure 5.4 IPC variation with detector temperature. Data taken at temperature ranging from 27.7K to 50 K. IPC is measured via hot pixels.	78
Figure 5.5 IPC variation with the detector temperature, where measurements via CREs and hot pixels are put together.	79
Figure 5.6 IPC vs. CREs intensity, data taken at 37 K. IPC is measured by CREs.	83
Figure 5.7 IPC vs. CRE intensity, data taken at 37 K. IPC is measured by CREs. Same dataset used as in Figure 5.6.	85
Figure 5.8 IPC vs. hot pixel intensity, data taken at 37 K. IPC is measured by hot pixels. Same dataset used as in Figure 5.6.	86
Figure 5.9 IPC vs. event intensity, data taken at 37 K. The graph combines the data from CREs and hot pixels (in Figure 5.6 and Figure 5.8). Same dataset used as in Figure 5.6.	87
Figure 5.10 Depletion region for HgCdTe arrays. Left: before charge collection, right: after charge collection.	89
Figure 5.11 IPC (%) vs. CRE intensity (ADU) for different background labeled with different colors.	92
Figure 5.12 Mean IPC vs. background for different background levels. The IPC measurements were averaged from the same background. Background was determined from the flat field level. Same data as in Figure 5.11.	94
Figure 5.13 Mean IPC vs. difference between mean CRE and background for different background levels. The IPC measurements and CRE intensities were averaged for the same background. Same data as in Figure 5.11.	95
Figure 5.14 Mean IPC vs. ratio of mean CRE to background for different background	

levels. Same data as in Figure 5.11.....97

LIST OF TABLES

Table 3.1 Results of relative change of signal at different levels through inverse filtering.	45
Table 3.2 Results of relative change of signal at different levels through Wiener filtering.	46
Table 3.3 Results of relative change of SNR at different levels through inverse filtering.	47
Table 3.4 Results of relative change of SNR at different levels through Wiener filtering.	48
Table 4.1 Directories and test data for the test detector array H2RG HgCdTe.	55
Table 4.2 Column autocorrelation function with a 10-pixel shift in the -y and +y directions.	58
Table 4.3 Row autocorrelation function with a 10-pixel shift in the -x and +x directions.	60
Table 4.4 Directories and test data for the test detector array H4RG Si-PIN.	61
Table 4.5 Column autocorrelation function with a 10-pixel shift in the -y and +y directions.	63
Table 4.6 Column autocorrelation function with a 10-pixel shift in the -y and +y directions.	65
Table 5.1 Directory and test data for the test detector array H2RG HgCdTe.	76
Table 5.2 Results of IPC measurement at different temperature by CREs in the HgCdTe array.	76
Table 5.3 Results of capacitive coupling magnitude at different temperature estimated by hot pixels in the HgCdTe array.	77
Table 5.4 Results of capacitive coupling magnitude at different event intensities estimated by cosmic rays in the HgCdTe array.	84
Table 5.5 Results of capacitive coupling magnitude at different event intensities estimated by hot pixels in the HgCdTe array.	86
Table 5.6 Continued.	86
Table 5.7 Directories and test data for the test detector array H2RG HgCdTe.	91
Table 5.8 Results of capacitive coupling magnitude at different flat field levels estimated by cosmic rays in the HgCdTe array, data from BL1_J+PK50-2 photon transfer experiments.	93
Table 5.9 Continued. Results based on data from BL1_H+PK50-2 photon transfer experiments.	93

Table 5.10 Continued. Results based on data from K+PK50-2_BL2 photon transfer experiments.....	94
---	----

1 Background

Astronomy is a subject that seeks to understand the universe not only from physical theories, but observational experiments, where high performance imagers are essential components. Astronomers usually deal with imaging applications under special environments. Low noise and high precision are required to sense very weak signals over a broad spectral range, which almost covers the entire electromagnetic spectrum, e.g. optical, infrared (IR), X-rays, radio, etc. In the past 20 years, image sensor technology has experienced dramatic advancement. The combination of near-ideal performance and implementation has made the charge-couple device (CCD) a highly successful imaging sensor. State-of-the-art CCDs have dominated most visible astronomy applications. However, the majority of CCDs suffer from high-energy radiation environments, serial readout operation, and large support electronics. As a result, complementary metal oxide semiconductor (CMOS) imagers are displacing CCDs in some astronomical applications, especially for space telescope projects. CMOS imagers are more tolerant to high-energy radiation environments. In addition, CMOS arrays read pixels primarily in a parallel, random access fashion, allowing high-speed operation and low noise performance, whereas only a very small portion of CCDs operate in the parallel mode. The technology advancement from monolithic CMOS to hybrid CMOS array has made CMOS image detectors comparable with CCDs in nearly every performance category, i.e. sensitivity, noise, quantum efficiency, dark current, and modulation transfer function. This chapter will survey these two types of image detectors, including monolithic CMOS image

detectors and hybrid CMOS arrays, e.g. per-pixel depleted IR and fully depleted silicon PIN (Si-PIN) arrays.

1.1 Monolithic CMOS array

CMOS imaging devices use the conventional fabrication process for computer chips, as compared to the specialized techniques required for CCD fabrication. Therefore, the cost of CMOS sensors is significantly reduced. In addition, more on-chip elements can be integrated, reducing system size, complexity, and power consumption. These features make CMOS devices a promising alternative to replace CCD imagers.

Most CMOS detectors are based on the p-n junction concept, where each p-n junction is a photodiode (photodetector), while CCD devices are referred to as voltage-induced p-n junctions because the applied gate voltage generates a potential well, causing the MOS capacitor (photogate) to behave like a p-n junction. In both imagers, incident photons striking the photoactive area of a detector array produce electron-hole pairs. For those pairs generated in the depletion region, they are then separated by the electric field there. Electrons and holes created outside the depletion region can diffuse into the depletion region, and these charge carriers also contribute to the collected signal. Besides the generic photodiodes, photogates and pinned-photodiodes also can be employed to sense photons in some CMOS sensors. The diagram in Figure 1.1 below illustrates the photo-sensing components in CCD and CMOS devices. Figure 1.2 shows the typical architecture of a CCD camera including readout and related functions.

Several major components are needed to measure the signal charge collected in a

CMOS pixel. In the photodiode pixel, three Metal-oxide-semiconductor field effect transistors (MOSFET) are used to read out the charge on the diode: (a) a source follower MOSFET, which converts charge signal to an output voltage signal, (b) a reset MOSFET, which resets the photodiode and clear off the residual charges before an integration begins, and (c) a row-select MOSFET, which selects a row for scanned readout (Janesick 2004). This structure is the widely used 3T CMOS image sensors in consumer applications. In the photogate or pinned-photodiode pixel, in addition to the three MOSFETs described above, one more MOSFET is employed to transfer signal charge from the collection diode to the sense node, floating diffusion. This is widely referred to as the 4T structure. The diagrams below in Figure 1.3 show these two types of CMOS sensors. In some 4T CMOS image sensors, the pinned-photodiode is replaced by the photogate used in CCDs. Figure 1.4 presents the typical block diagram of CMOS image sensors.

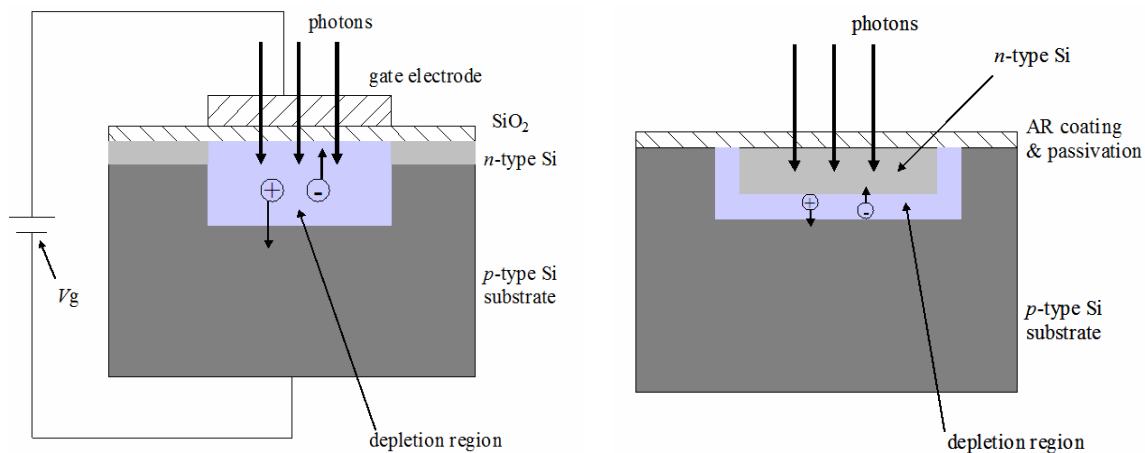


Figure 1.1 Left: cross section of a MOS capacitor (buried channel); right: p-n junction photodiode

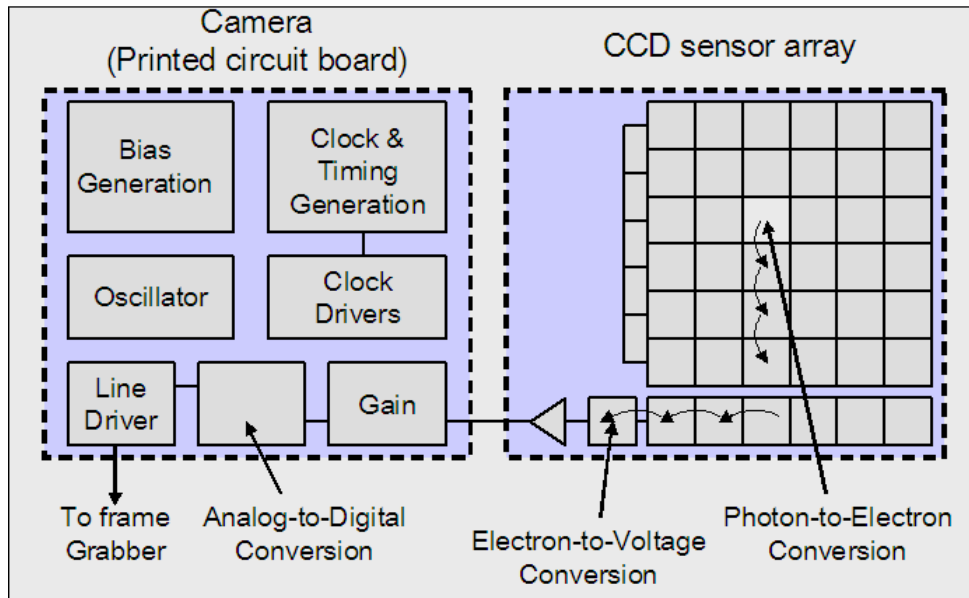


Figure 1.2 Architecture of monolithic CCD image sensors.

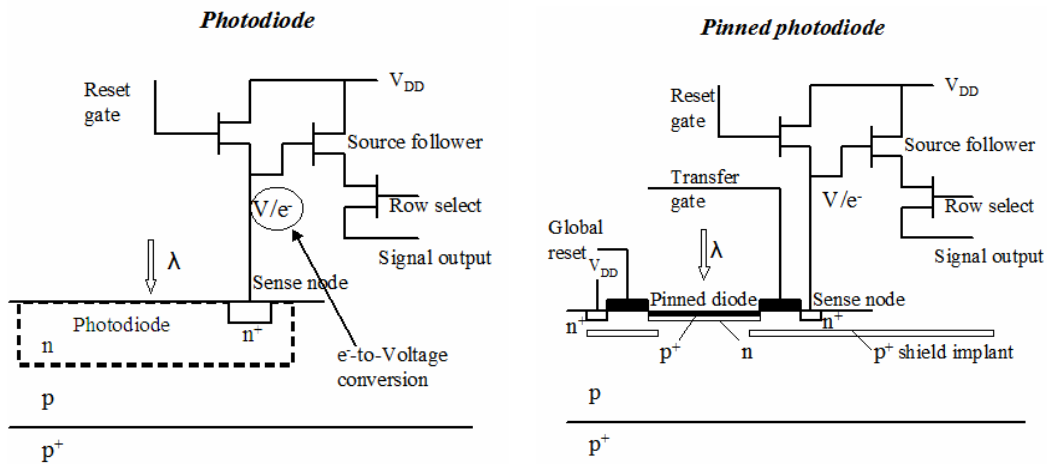


Figure 1.3 Sense node (photodetector) and the associated readout components in CMOS sensors. Left: photodiode (3T); right: Pinned photodiode or photogate (4T).

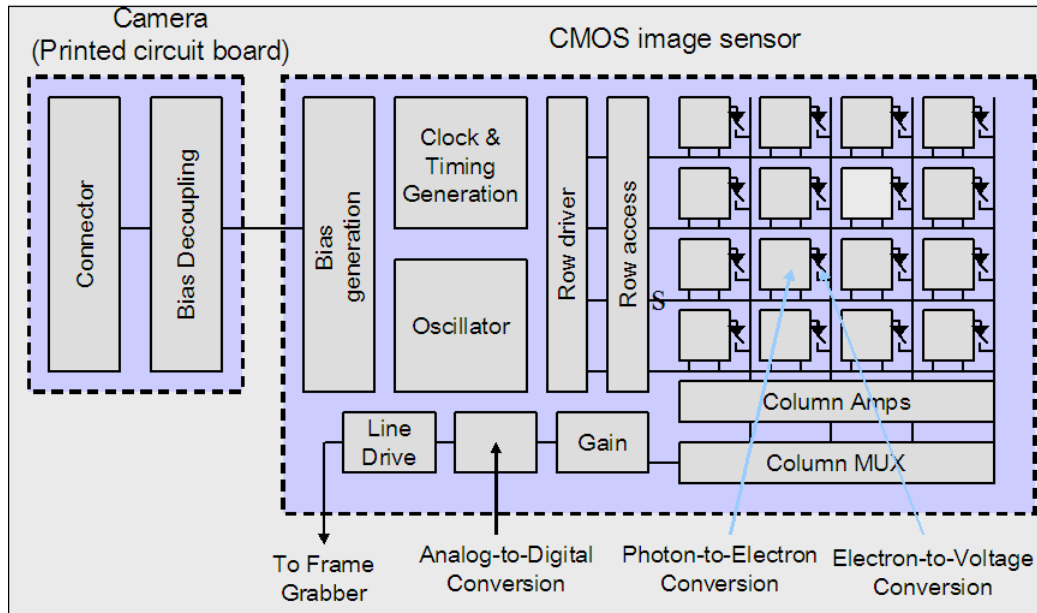


Figure 1.4 Architecture of monolithic CMOS image sensor.

In a monolithic CMOS array, the photosensitive detector array and readout components for each pixel, e.g. the 3T or 4T structures in Figure 1.3, are built on the same piece of silicon wafer, as indicated in Figure 1.4. Therefore, monolithic imagers offer high integration, small volume, less power consumption, low cost, etc. However, the image quality of monolithic array is not good enough for astronomical applications, especially for space telescopes due to the design tradeoff between the pixel array and readout circuitry. Therefore, the system-on-chip imagers are only popular in consumer cameras.

1.2 Hybrid CMOS array

Most CMOS imagers currently employed in astronomical applications are hybrid CMOS

arrays. A hybrid sensor array is composed of two components: a detector array and readout integrated circuit (ROIC). The detector array is usually a photodiode array and responsible for photon-to-charge conversion. The ROIC is a multiplexer and functions as a charge-to-voltage converter and signal processor. Two components are built separately, and then precisely aligned and bonded together through indium bumps. Figure 1.5 illustrates the structure of a typical hybrid CMOS array. The unique feature of this hybrid is that both components can be optimized independently to maximize the detector sensitivity and ROIC functionality. Due to the extra fabrication steps required for interconnection components, this hybrid approach can cost much more than the monolithic counterparts, but the special design and structure make it potentially an ideal candidate for space applications.

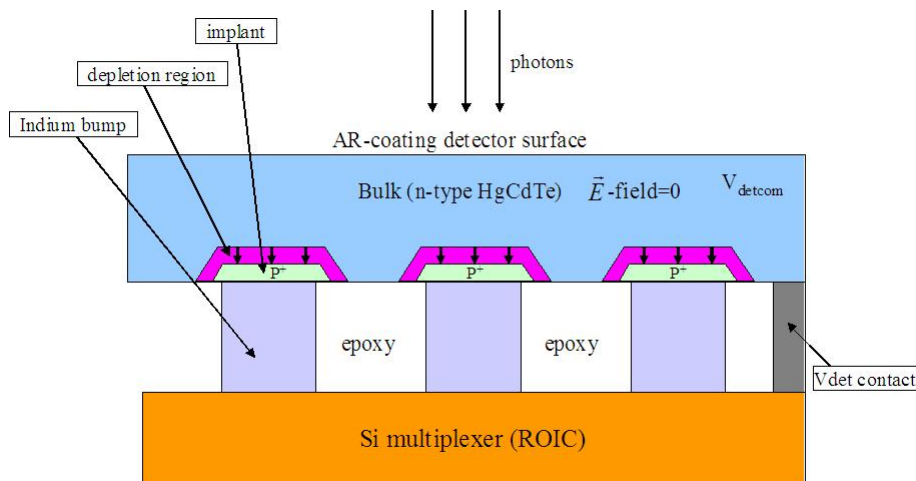


Figure 1.5 Cross section of typical IR hybrid CMOS detectors (per-pixel depleted) and Si multiplexer.

In astronomical applications, there are mainly two types of hybrid detectors, IR and Si-PIN arrays. In the mid-IR spectral range from 8 μm to 28 μm , blocked impurity band Si: As are widely used. In the near-IR range from 1 μm to 5 μm , the two technologies, namely

InSb and HgCdTe, are competing in both ground and space-based astronomical applications. InSb is the simpler compound with the cutoff wavelength of $5.2\mu\text{m}$ and has been used for applications including the L and M band atmospheric windows (Finger and Beletic 2003). The alloy $\text{Hg}_{(1-x)}\text{Cd}_x\text{Te}$ allows to tune the cutoff wavelength to the specific application by varying the stoichiometric composition x (Long and Scmit 1970). This unique feature makes HgCdTe popular in the near-IR applications. In the IR detectors, the pixel array is typically per-pixel depleted. Both the two types of near-IR detectors employ the similar hybrid structure as shown in Figure 1.5.

The hybridized Si-PIN array, silicon PIN diode array as illustrated in Figure 1.6, is somewhat unusual with the detector bulk fully depleted and electric fields existing throughout the entire bulk, in comparison with the per-pixel depleted IR detectors. It can operate in the range from the optical to UV band, may even in the X-ray band. Both the IR and Si-PIN arrays can employ the same ROIC, e.g. HAWAII-class multiplexers (H1RG, H2RG, etc.). The near-IR detector is the pioneer of hybrid arrays in astronomy. This type of detector is per-pixel depleted and the bulk is conductive. Due to the band gap limitation of silicon, most near-IR detectors are based on HgCdTe (MerCad) and InSb. The Si-PIN detectors are operated at very high bias compared to IR detectors, producing high electric fields. The high field strength means that one can expect good charge collection efficiency and low diffusion crosstalk. Hence, Si-PIN detectors have good quantum efficiency (QE) in both red and blue wavelengths. In the image detector array discussed below, we will focus on the two types of hybrid CMOS arrays, i.e. the near-IR HgCdTe and Si-PIN detectors.

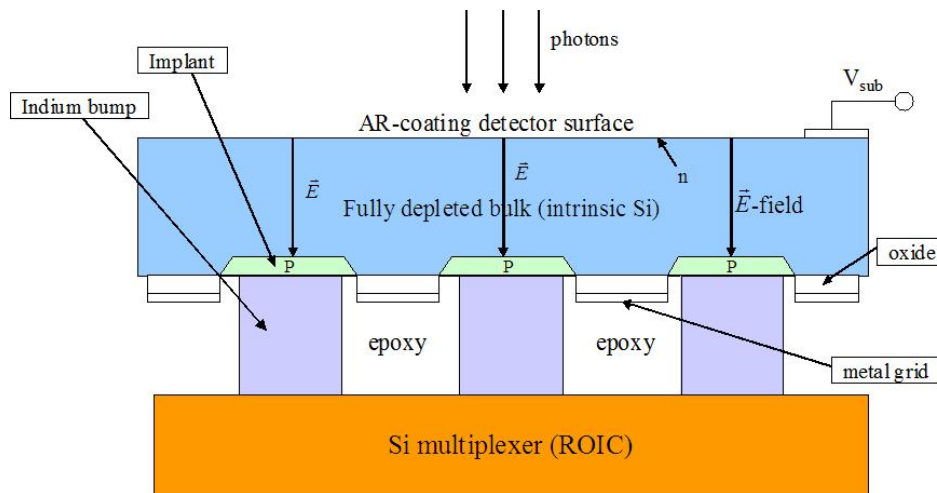


Figure 1.6 Cross section of Si-PIN detector array and associated the Si multiplexer.

1.3 Crosstalk

Crosstalk is a phenomenon where photons strike a target pixel but the photo charges are collected by a different pixel. In typical imaging applications, signal electrons generated in a photo detector should remain in the target pixel. However, optical and electrical mechanisms can drive the charge carriers away such that they are collected by a neighboring pixel. The signal distortion causes modulation transfer function (MTF) loss, and thus damages the sensor sharpness. Crosstalk is highly unwanted in image applications. Generally there are three mechanisms causing crosstalk, i.e. optical, diffusion, and interpixel capacitance.

1.3.1 Optical crosstalk

Solid state imagers are based on the photoelectric effect. Photoelectrons are generated by photovoltaic reaction of photons colliding into silicon or other detector materials.

However, just because an electron is released doesn't mean that it will be collected by the pixel well, it could be reabsorbed and recombine in the pixel or wander into adjacent pixels. When a photon intersects at an angle with a pixel surface, it is possible for that photon to enter the adjacent pixel's photodetector (photodiode) and not the photodetector under the incident surface. This will lead to contamination of the adjacent pixel's charge packet—called optical crosstalk. For instance, consider light going through a red filter area of a color filter array (CFA) at such an angle that it hits the photodetector under the adjacent green pixel. This will result in serious artifacts in the color image. As can be seen in Figure 1.7, optical crosstalk is dependent on the incident angle of light and pixel pitch. The larger the incident angle, the bigger the optical crosstalk.

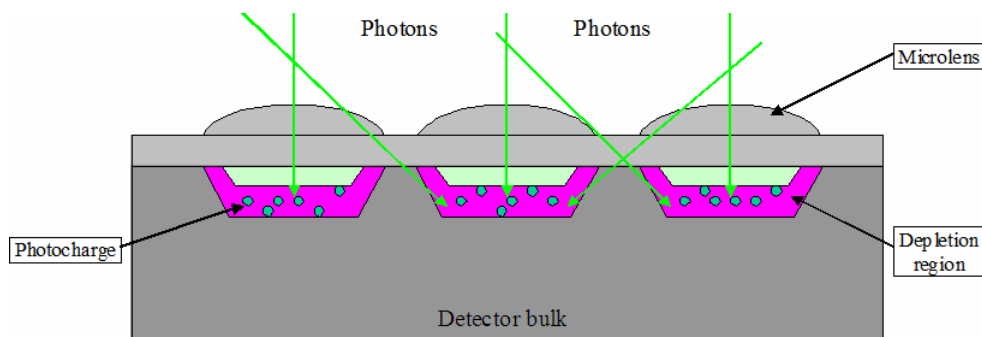


Figure 1.7 A simple illustration of optical crosstalk occurring in image detectors. Photons incident on a target pixel finally may be absorbed in the neighbors due to inclined incident angle, multi-reflections, refraction in the image sensor, etc.

When optical crosstalk exists, it is difficult to correct by image processing techniques. However, it can be controlled to a certain extent by adding barriers between pixels. For example, some manufacturers use black boundaries on the CFA to generate an optical shield to separate the different color pixels (Rhodes et al. 2004). Other approaches include using metal light shields usually below the CFA, air gaps in the pixel boundaries, light

guide, etc (Hsu et al. 2004 and 2005). The metal shield method is more reliable than the black optical shields, but the metal is more costly, and takes up more space and adds weight.

1.3.2 Diffusion

When photons strike a pixel, the photoelectrons generated have two fates. For those created within the depletion region, they will be collected by the electric field, and accumulate in the potential well. For those created outside the depletion region, they will diffuse via thermal motion. In the course, some of them may recombine with holes and will not contribute to signal charge. Some may diffuse toward the pixel well and are collected as the pixel signal. In addition, many carriers can diffuse laterally into nearby pixels and are collected there. This lateral diffusion is referred to as diffusion crosstalk. Figure 1.8 illustrates the diffusion occurring in the front-side illuminated (FSI) image detector with microlens. Similar problems occur in back-side illuminated (BSI) image detectors where the bulk substrate is thinner (see Figure 1.9). As it is driven by thermal motion of charge carriers, diffusion crosstalk is a stochastic process and is sensitive to the detector temperature.

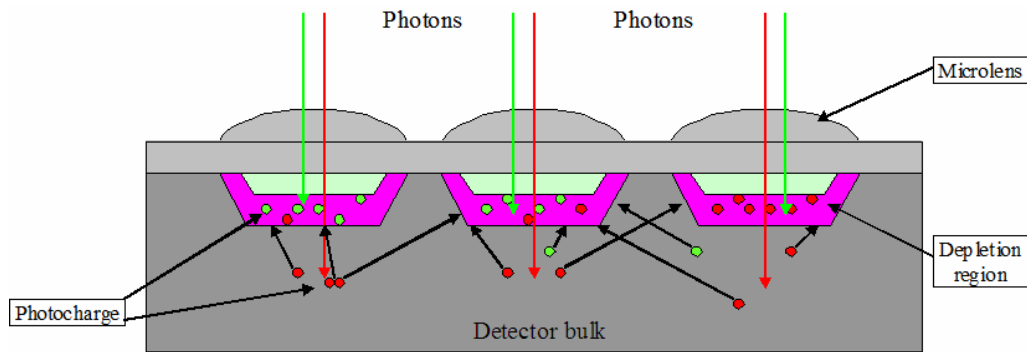


Figure 1.8 Illustration of diffusion crosstalk occurring in FSI image detectors.

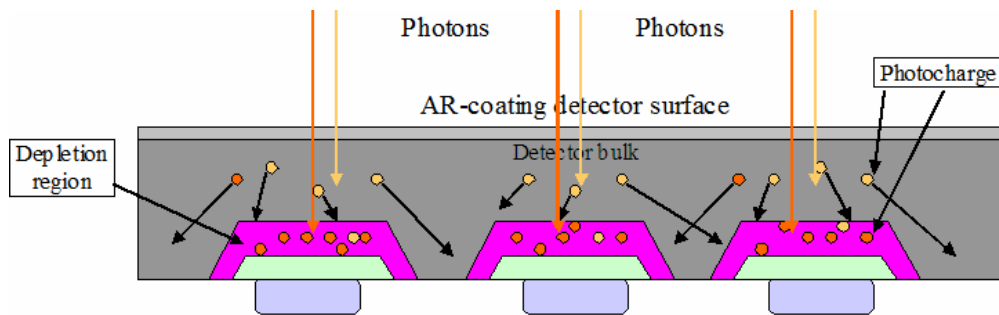
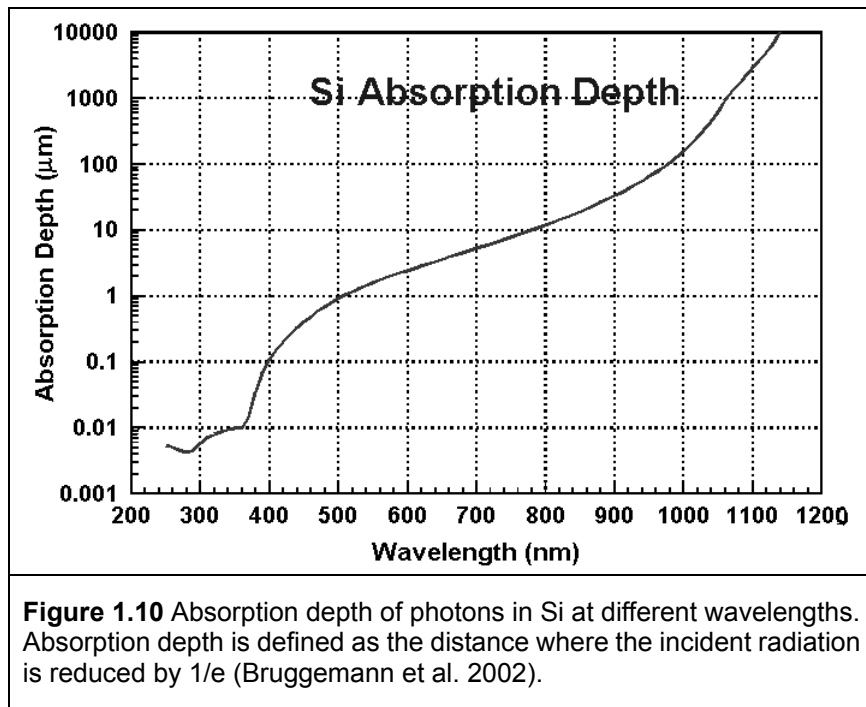


Figure 1.9 Illustration of diffusion crosstalk occurring in BSI image detectors.

The absorption depth of photons in the silicon material is a function of wavelengths as shown in Figure 1.10, where red and infrared light have longer absorption depth than the blue and green light. Therefore, the strength of diffusion strongly depends on the wavelengths of incident photons. As we can see from Figure 1.10, in the optical wavelength range the light of short wavelengths has small absorption depth. The absorption effect means that an image detector cannot be simultaneously optimized for all wavelengths. For a typical optical detector that is optimized for the green-yellow band, red photons can travel further into the silicon substrate before generating electrons, and electrons that are created are more likely to be outside the depletion region in the detector

bulk. These electrons can wander into the wrong nearby pixel. Therefore, red light has higher diffusion crosstalk than the shorter blue and green light. In addition, as stated above, only those photoelectrons created outside the depletion region can cause diffusion, so pixels with a deeper depletion region will have less crosstalk effect. For instance, the Si-PIN detectors are fully-depleted pixels with electric fields throughout, and very few electrons can diffuse into neighboring pixels. Finally, diffusion crosstalk increases as pixel size is reduced as electrons only need to travel a short distance to adjacent pixels.



Like optical crosstalk, diffusion also degrades the MTF of imaging sensors, causing uncorrectable image quality loss by image processing. So the effect needs to be countered by optimized sensor design. For example, the depth of the pixel potential well can be optimally designed to minimize lateral diffusion according to the target wavelengths of

light. Diffusion problem can also be improved by using thinner epitaxial silicon at the expense of losing red sensitivity (Jansick 2003).

1.3.3 Interpixel capacitive coupling

Besides thermal diffusion, the photo charge can also wander into adjacent pixels because of weak electric fields between pixels. This crosstalk is termed interpixel capacitance or capacitive coupling (IPC). As the individual pixel diodes are not electrically independent, a coupling capacitance may exist between adjacent pixels. In fact, the presence of interpixel capacitance in CMOS detector arrays was anticipated in simulations by Kavadias et al. (1994) and measured in a hybrid “Vertex” detector for a supercollider by Caccia et al. (2001). Interpixel capacitance tends to become more pronounced with modern detector arrays. As detector array designers continue to strive for high pixel density (small pixel pitch), low latent image (high fill factor—small gaps between pixel implant), and high sensitivity (low node capacitance), this stray capacitance could be more serious (Moore et al. 2004). However, it has not received much attention until in recent years Moore et al. (2004) found that the conversion gain was overestimated by the “noise squared vs. mean signal” method, which is widely used to estimate the conversion gain and read noise by fitting the plot of noise variance vs. mean signal, and is also called the photon-transfer method. What’s more, interpixel coupling is found to be unusually large in the state-of-art Si-PIN array (Finger et al. 2006; Bai et al. 2007). All of these pose new problems on the characterization and design of image detectors, specifically the hybrid IR and Si-PIN CMOS array.

Theoretically, interpixel capacitive coupling exists in both monolithic and hybrid

CMOS array. However, the complicated layout of photodiodes and the associated readout components in monolithic array make this coupling negligible compared with optical and diffusion crosstalk. Therefore, the effect has not received much attention in the monolithic array. However, the unique interconnection structure in hybrid arrays provides the possibility for a capacitive coupling to be comparable to diffusion. The diagrams in Figure 1.11 and Figure 1.12 below illustrate how interpixel coupling could occur in the IR and Si-PIN arrays. As stated in Section 1.2, an IR array is a per-pixel depleted detector whereas the Si-PIN is a fully-depleted bulk detector. Both arrays can share the same multiplexer.

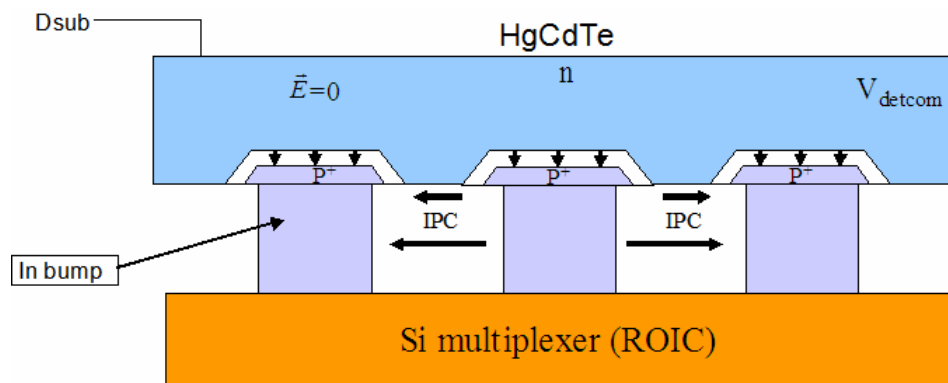


Figure 1.11 Capacitive coupling in more typical per-pixel depleted detectors occurs in the space between the multiplexer and detectors between In bumps.

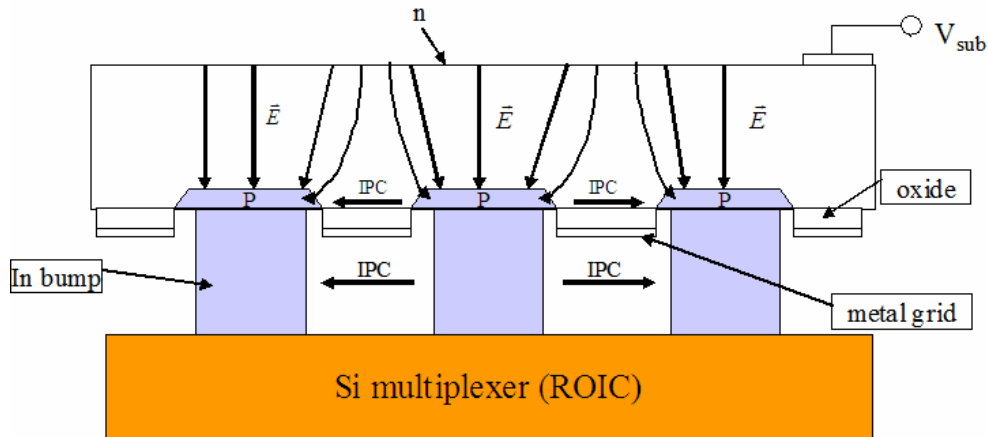


Figure 1.12 Major coupling in fully depleted detectors occurs in the detector bulk, in addition to the coupling in the space between the detectors and multiplexer.

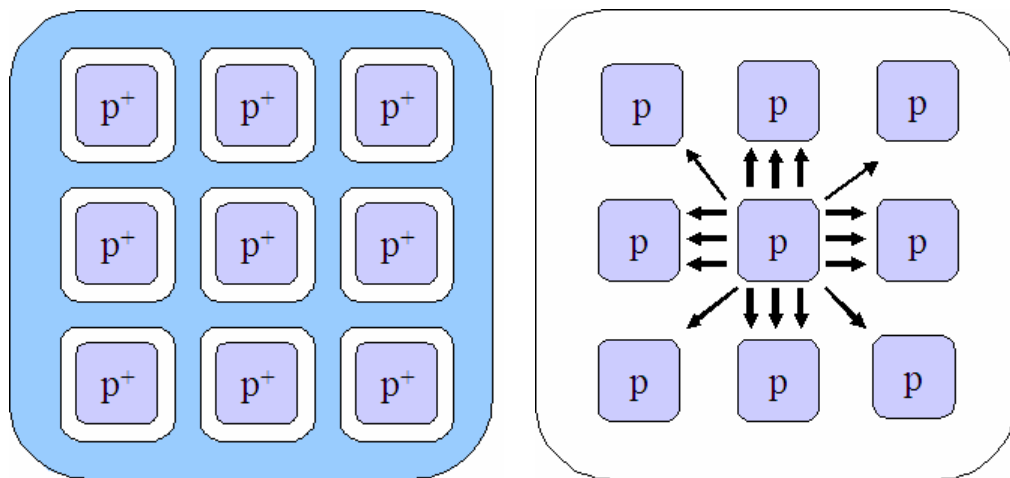


Figure 1.13 Sketch of electric fields in detector arrays from top view (left: HgCdTe; right: Si-PIN). White area denotes regions with electric fields and is free of charge carriers. Shaded areas are p or n type regions of equal potential. Depletion regions in HgCdTe arrays are separated by conducting n-type detector bulk. The bulk of Si-PIN array is fully depleted with capacitive coupling between pixels inside the photodiode array.

The interpixel coupling in Si-PIN diode arrays is much larger than in HgCdTe IR arrays. This is because the detector bulk of Si-PIN diodes are fully depleted, while IR detectors have a separate depletion region close to the pixel implant, in the sense that each

pixel photodiode maintains its own local depletion region as shown in Figure 1.13. Shaded areas in Figure 1.13 have equal potential, either neutral p or n regions or In bumps between the photodiode array and the Si multiplexer. A pixel of IR HgCdTe array is separated from its neighbors by the n-doped bulk of HgCdTe, which is conducting and surrounds the pixel. As there is no electric field between pixels, they are screened from each other (Finger et al. 2006, Bai et al. 2007). The n-doped bulk acts like a protection ring screening adjacent pixels from capacitive coupling. As a result, the interpixel capacitive coupling can hardly occur in the HgCdTe diode array. It likely happens in the space between the HgCdTe diode array and the Si multiplexer between the In bumps. It may even occur within the multiplexer itself (Brown 2007). Analysis and simulation by Moore et al. (2006) indicates that coupling occurs mainly through fringing fields between the edges of adjacent pixels.

On the other hand, the bulk of the silicon in the Si-PIN detectors is fully depleted and the electric fields can build up between pixels, in addition to the space between the diode array and the multiplexes, as indicated in Figure 1.12. This will result in the large observed interpixel coupling. Since the Si-PIN array uses similar indium bumps and exactly the same multiplexer as the IR HgCdTe array, but exhibits much stronger IPC, it may be assumed that the coupling mainly occurs inside the Si-PIN diode array. The coupling can be reduced by decreasing the size of the p implants, which increases the separation between the conducting p regions and decreases the coupling capacitance between adjacent pixels. Because the applied bias, which is usually denoted by V_{SUB} or D_{SUB} , only change the electric field normal to the array surface, and have no effect on the electric field parallel to the surface, i.e. fringing field, in the direction of the interpixel capacitive coupling, the

coupling capacitance supposedly does not depend on these voltages. However, Bai et al. (2007) found that the magnitude of interpixel coupling is a function of detector bias, in the sense that the coupling amount decreases with increasing detector bias. This suggested that the mechanism of capacitive coupling is more complicated than we thought so far. A physical model based on detector material, bump interconnection, and multiplexer is greatly needed to explain capacitive coupling in more detail.

As described above, interpixel coupling and diffusion crosstalk have different mechanisms and thus different properties. Charge diffusion occurs during the charge collection and is dependent on the detector bias, temperature, and wavelengths of incoming light. On the other hand, capacitive coupling between pixels occurs after charge collection, and during the charge-to-voltage conversion process. This coupling strongly depends on the structure of readout circuits. In addition, diffusion is a stochastic process such that Poisson noise is completely uncorrelated to the adjacent pixels. Capacitive coupling is a fully deterministic process: Poisson noise measured with capacitive coupling is correlated to the neighbors (Moore et al. 2006). Therefore, given the full knowledge of capacitive coupling, its effect can be corrected through post-image processing.

Interpixel coupling has two effects: first, a strong signal in a pixel will create a weak signal in its neighbors. This effect is easily mistaken as the more common diffusion crosstalk, which occurs after photoelectrons are created within a pixel, but part of them diffuse to adjacent pixels. As a result, the signal in the center pixel is attenuated and its neighbors' are increased. The signal appearing in the neighboring pixels is the signal that

should have appeared in the central pixel if there were not interpixel capacitance. The image quality is therefore distorted by the coupling. As presented above, interpixel coupling is a deterministic process whereas charge diffusion is a stochastic process. Poisson noise from diffusion crosstalk is not spatially correlated. However, Poisson noise with interpixel capacitance is spatially correlated, which causes the Poisson noise to be attenuated. In this regard, interpixel coupling behaves as a low-pass filter, which not only smooths the signal but the noise. Details will be presented in the next section.

Since the smoothing effect of capacitive coupling leads to underestimation of Poisson noise, conversion gain will be overestimated by the “noise squared vs. mean signal” method (Janesick 2001). This creates extra errors in the measurement of other sensor performance parameters, e.g. quantum efficiency (QE), dark current, and various noises, which strongly depend on the accurate measurement of conversion gain. As Moore et al. (2004, 2006) derived, a capacitive coupling of 1% to each adjacent pixel will result in an error of 8% in the measurement of noise square (variance), and thus an 8% error in the estimated conversion gain, as well as other related parameters.

1.3.4 Basic mechanism of interpixel capacitance

As Moore et al. (2004, 2006) stated, the detector element of an image detector array can be modeled as a capacitor $C[i, j] = C_{\text{node}}$ assuming the array is uniformly fabricated. Each capacitor receives a signal charge $Q[i, j]$ over the integration time Δt . Modeling the array as a discrete linear shift-invariant (LSI) system, the output can be written as below:

$$V[i, j] = \sum_{m=0}^M \sum_{n=0}^N Q[m, n] h_c[i - m, j - n] \quad (1.1)$$

This can be simply rewritten as the convolution of $Q[i, j]$ and $h_c[i, j]$, as shown below.

$$V[i, j] = Q[i, j] * h_c[i, j] \quad (1.2)$$

where $*$ denotes the 2-D convolution and $h_c[i, j]$ is the impulse response or point spread function of the detector array of size $M \times N$. Ideally, there would be no crosstalk across the diode array and $h_c[i, j]$ would reduce simply to a discrete delta function:

$$h_c[i, j] = \frac{\delta[i, j]}{C_{node}} \quad (1.3)$$

Thus the ideal output of the array is a voltage $V[i, j]$ determined only by the signal charge collected locally.

$$V[i, j] = \frac{Q[i, j]}{C_{node}} \quad (1.4)$$

Due to capacitive coupling between pixels, the impulse response $h_c[i, j]$ is no longer a delta function, and the signal charges on each capacitor will redistribute inductively across the detector array. The final signal at a single detector node is dependent on not only the photocharge it collects, but the adjacent detector node and mutual coupling strength. Figure 1.14 shows the layout of the mutual capacitance C_c between detector nodes and node capacitance. Suppose a point light source striking a center pixel (detector node) and an amount of photocharge Q_{point} is collected, whereas the neighbors have no photocharge. Due to capacitive coupling, a portion of center charge Q_{point} will appear on adjacent detector nodes by induction. The resulting charge distribution at each node $Q'[i, j]$ can be expressed as:

$$Q_{point} = \sum_{i=0}^M \sum_{j=0}^N Q'[i, j] \quad (1.5)$$

The impulse response of the array is thus

$$h_c[i, j] = \frac{Q'[i, j]}{Q_{point} C_{node}} \quad (1.6)$$

After normalizing the node capacitance, the impulse response becomes

$$h_{ipc}[i, j] = \frac{Q'[i, j]}{Q_{point}} \quad (1.7)$$

Obviously, the summation of $h_{ipc}[i, j]$ over all the detector nodes is

$$\sum_{i=0}^M \sum_{j=0}^N h_{ipc}[i, j] = \sum_{i=0}^M \sum_{j=0}^N \frac{Q'[i, j]}{Q_{point}} = 1 \quad (1.8)$$

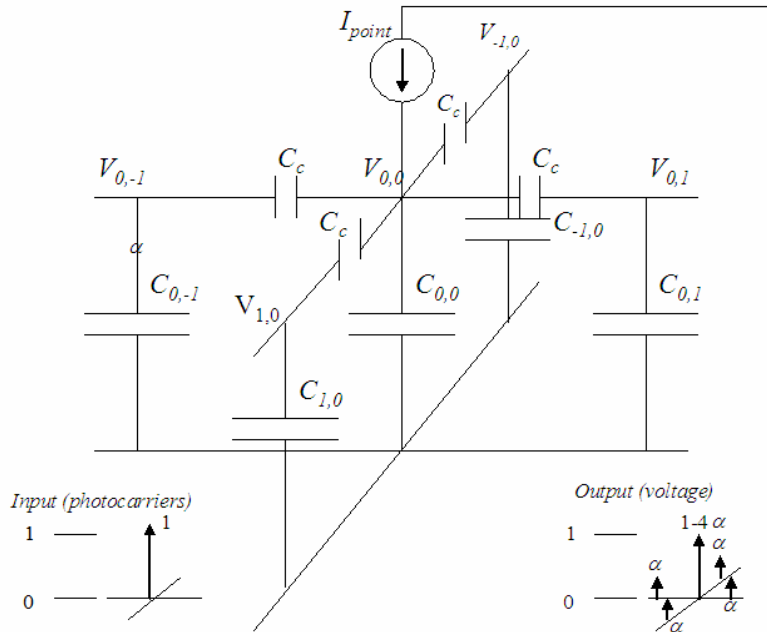


Figure 1.14 Layout of detector nodes and interpixel capacitance. Photocurrent enters a detector node $C_{0,0}$, which collects photocharges. The signal can still appear on adjacent nodes that are not exposed to photons (Moore et al. 2006).

Now interpixel coupling is modeled as a low-pass convolution kernel $h_{ipc}[i, j]$, and a real image $Q'[i, j]$ can be expressed as the convolution of the initial signal $Q[i, j]$ and the coupling response, as indicated below.

$$Q'[i, j] = Q[i, j] * h_{ipc}[i, j] = (M[i, j] + N_{poisson}[i, j]) * h_{ipc}[i, j] + N_{rd}[i, j] \quad (1.9)$$

where $M[i, j]$, $N_{poisson}[i, j]$, and $N_{rd}[i, j]$ are the mean signal component, Poisson noise (shot noise), and read noise, respectively. The difference $D[i, j]$ of two images, $Q'_1[i, j]$ and $Q'_2[i, j]$, captured under identical conditions cancels out the mean signal component and leaves only noise components, which are twice the variance of the original noises.

$$D[i, j] = Q'_1[i, j] - Q'_2[i, j] = (N_{poisson1}[i, j] - N_{poisson2}[i, j]) * h_{ipc}[i, j] + N_{rd1}[i, j] - N_{rd2}[i, j] \quad (1.10)$$

Assuming the images $Q'_1[i, j]$ and $Q'_2[i, j]$ are dominated by Poisson noise, the read noise component in Eq. (1.10) can be negligible. It then becomes

$$D[i, j] = Q'_1[i, j] - Q'_2[i, j] = (N_{poisson1}[i, j] - N_{poisson2}[i, j]) * h_{ipc}[i, j] \quad (1.11)$$

From the Poisson distribution, the variance of a shot noise image in quanta is equivalent to the mean signal M . We have

$$\sigma_{N_{poisson}}^2[i, j] = M[i, j] \quad (1.12)$$

The power spectral density of the difference image, $S_D(\xi, \eta)$, in Eq. (1.11) is

$$S_D(\xi, \eta) = 2\sigma_{N_{poisson}}^2 |H_{ipc}(\xi, \eta)|^2 \quad (1.13)$$

where ξ and η represent the spatial frequency in the horizontal and vertical directions, respectively. Take the inverse Fourier transform of Eq. (1.13) and we obtain

$$FT\{S_D(\xi, \eta)\} = R_D[x, y] = 2\sigma_{N_{poisson}}^2 h_{ipc}[x, y] * h_{ipc}[-x, -y] \quad (1.14)$$

Where $R_D[x, y]$ denotes the autocorrelation function of the difference image and is the Fourier transform of power spectral density (Peebles 2000). As can be seen in Eq. (1.14), the autocorrelation of the difference image is equal to the correlation of the impulse response with itself, scaled by the Poisson noise square. As the impulse has a unit area, its autocorrelation also does. So the summation of Eq. (1.14) is

$$\sum_{i,j} R_D[i, j] = 2\sigma_{N_{poisson}}^2 \quad (1.15)$$

Eq. (1.15) is very important for noise squared estimation because it is different from the conventional variance estimator, as shown below

$$2\hat{\sigma}_{N_{poisson}}^2 = \hat{R}_D[0,0] = \frac{\sum_{i,j} D^2[i, j]}{mn} \quad (1.16)$$

where the image size is $m \times n$. Assuming that most capacitive coupling is to the four nearest neighbors, from Eq. (1.15), Moore et al. (2006) derived an approximate formula to estimate Poisson noise variance $\sigma_{N_{poisson}}^2$ of a flat field scene,

$$\hat{\sigma}_{N_{poisson}}^2 = \frac{1}{2mn} \left[\sum_{i,j} D^2[i, j] + 2 \sum_{i,j} D[i, j]D[i+1, j] + 2 \sum_{i,j} D[i, j]D[i, j+1] \right] \quad (1.17)$$

Supposing the interpixel coupling to immediate neighbors is 1%, from Eq. (1.16) and Eq. (1.17) it can be derived that the traditional estimator will underestimate Poisson noise by about 4%, and result in an 8% error in the measurement of noise squared and thus conversion gain by the photon transfer method.

When the signal is weak enough that readout noise is not negligible, the power spectral density $S_D(\xi, \eta)$ of the difference image $D[i, j]$ becomes

$$S_D(\xi, \eta) = 2\sigma_{N_{poisson}}^2 |H_{ipc}(\xi, \eta)|^2 + 2\sigma_{N_{rd}}^2 \quad (1.18)$$

Take the inverse Fourier transform of Eq. (1.18) and we obtain

$$FT\{S_D(\xi, \eta)\} = R_D[x, y] = 2\sigma_{N_{poisson}}^2 h_{ipc}[x, y] * h_{ipc}[-x, -y] + 2\sigma_{rd}^2 \delta[x, y] \quad (1.19)$$

where $\delta[x, y]$ is the Dirac delta function. The summation of Eq. (1.19) becomes

$$\sum_{i,j} R_D[i, j] - 2\sigma_{rd}^2 = 2\sigma_{N_{poisson}}^2 \quad (1.20)$$

So Eq. 1.17 is replaced with Eq. 1.21 below

$$\hat{\sigma}_{N_{poisson}}^2 = \frac{1}{2mn} \left[\sum_{i,j} D^2[i, j] + 2 \sum_{i,j} D[i, j]D[i+1, j] + 2 \sum_{i,j} D[i, j]D[i, j+1] \right] - 2\sigma_{rd}^2 \quad (1.21)$$

This is a more general formula to estimate Poisson noise from the difference of any two images obtained under identical conditions. The contribution of readout noise is subtracted. When the readnoise is small enough to be negligible, Eq. 1.21 reduced to the simplified equation 1.17.

2 Methodology on the measurement of interpixel coupling

In the past few of years, several methods have been developed to measure interpixel coupling. Generally, they are classified into two categories: direct and indirect approaches. The most straightforward way to measure the electronic crosstalk, capacitive coupling and diffusion, is to illuminate a single pixel with a tiny optical spot and measure coupling to neighboring pixels. Other direct methods include hot pixels (pixels with very high dark current), cosmic ray events, and Fe55 X-ray sources. Interpixel coupling can be also measured indirectly by special reset techniques for the multiplexer, e.g. Hawaii-2RG, used on scientific hybrid arrays, such as single pixel reset test by Finger et al. (2005). In addition, Seshadri et al. (2007) and Hanold et al. (2007) recently did experiments to change the reset bias level, V_{reset} , of some particular pixels to mimic the process of charge carrier collection during the integration. Their results were reasonable. These direct methods depend on isolated single events, which are generated optically or electrically. Since the value of capacitive coupling may change under different operation conditions of image detectors, a certain number of events are required to reduce the measurement uncertainty. The approach, which is independent of single pixel events, is the autocorrelation method developed by Moore et al. (2004). It gives us an average IPC measurement via flat field images. In the thesis, we used autocorrelation, cosmic ray events, and hot pixels to estimate the coupling for specific purposes. In this chapter I will give an overview of different IPC measurement methods.

2.1 Autocorrelation

As discussed in Sec. 1.3.4, the autocorrelation of the difference of two identically acquired flat field images is equal to the correlation of the impulse response $h_{ipc}[x, y]$ with itself. Therefore, by computing the autocorrelation function of the difference of two photon noise dominated images or any mean-subtracted photon noise dominated images, we can estimate an average coupling amount between adjacent pixels. Suppose the interpixel coupling magnitude in percentage to each of nearest neighbors is α . Neglecting second-neighbor and diagonal neighbor coupling, the center pixel will have $1-4\alpha$ of its original voltage signal, 4α appearing in the neighbors. The impulse response can be approximated as follows

$$h_{ipc}[i, j] = (1 - 4\alpha)\delta[i, j] + \alpha\delta[i + 1, j] + \alpha\delta[i - 1, j] + \alpha\delta[i, j + 1] + \alpha\delta[i, j - 1] \quad (2.1)$$

From Eq. (1.14) we get

$$h_{ipc}[x, y] * h_{ipc}[-x, -y] = \frac{R_D[x, y]}{2\delta_{N_{poisson}}^2} \quad (2.2)$$

Neglecting the second-order terms, the correlation of $h_{ipc}[x, y]$ with itself can be approximated below.

$$\begin{aligned} \frac{R_D[0,0]}{2\delta_{N_{poisson}}^2} &= (1 - 4\alpha)^2 + 4\alpha^2 \approx 1 - 8\alpha \\ \frac{R_D[1,0]}{2\delta_{N_{poisson}}^2} &= \frac{R_D[0,1]}{2\delta_{N_{poisson}}^2} = 2\alpha(1 - 4\alpha) \approx 2\alpha \end{aligned} \quad (2.3)$$

In practice, we can normalize the autocorrelation function below,

$$\hat{\alpha} = \frac{1}{2} \frac{R_D[0,1]}{\sum_{x,y} R_D[x,y]} \approx \frac{1}{2} \frac{R_D[0,1]}{R_D[0,0] + 2R_D[0,1] + 2R_D[1,0]} \quad (2.4)$$

From Eq. (2.4), it can be seen that capacitive coupling is just half of the nearest-center terms in the normalized autocorrelation. In addition, the conventional Poisson noise estimator, as indicated in Eq. (1.16), will underestimate Poisson noise squared by 8α , and thus an 8α error in the conversion factor estimation by the photon transfer method.

However, the autocorrelation method is sensitive to damage pixels, e.g. cosmic ray events and defective pixels, and outlying pixels. These special pixels need to be excluded from the difference image before implementing autocorrelation. The effectiveness of identification of these pixels will significantly affect the measurement accuracy. Either dividing the difference image into many small patches free of cosmic events and defects (Moore et al. 2006), or employing a mask to mask out those pixels (Brown et al. 2006) will make the computing of autocorrelation less efficient. What's more, we need to capture a certain number of flat-field frames under exactly the same illumination conditions. This method is not used in this thesis to measure interpixel coupling.

2.2 Optical spot illumination (Spotomatic)

The most straightforward way to measure the crosstalk caused by mutual capacitance between pixels is to illuminate a single pixel with a tiny spot and measure the signal charge distribution surrounding it (that is point spread function, PSF), keeping the rest of the array exposed in the dark. It requires a microscope setup to measure the spot size

precisely before projecting the spot on a specific pixel. In addition, the spot positioning within the target pixel should be adjusted to near the pixel center, which can reduce the asymmetry of the crosstalk due to interpixel capacitance. A sample image under such optical spot illumination is displayed in Figure 2.1 below (Dorn et al. 2006). The coupling amount can be calculated by analyzing the pixel levels around the spot-targeted pixel. Figure 2.1 indicates how the shot image and surface plot of interpixel coupling PSF look. The big issue related to this method is that it requires high-quality instruments to generate an optical spot of tiny size and to position the spot precisely within a pixel. Another problem is charge diffusion and optical crosstalk. What is measured includes the crosstalk contributed not only from capacitive coupling, but also from diffusion and optical crosstalk. The measurement is the total of these three components, so this approach only gives us an upper limit upon the IPC magnitude. Practically, it poses extra requirements in the experiment to reduce the effects of diffusion and optical crosstalk, for instance, a specific wavelength of light can be used to minimize the diffusion effect.

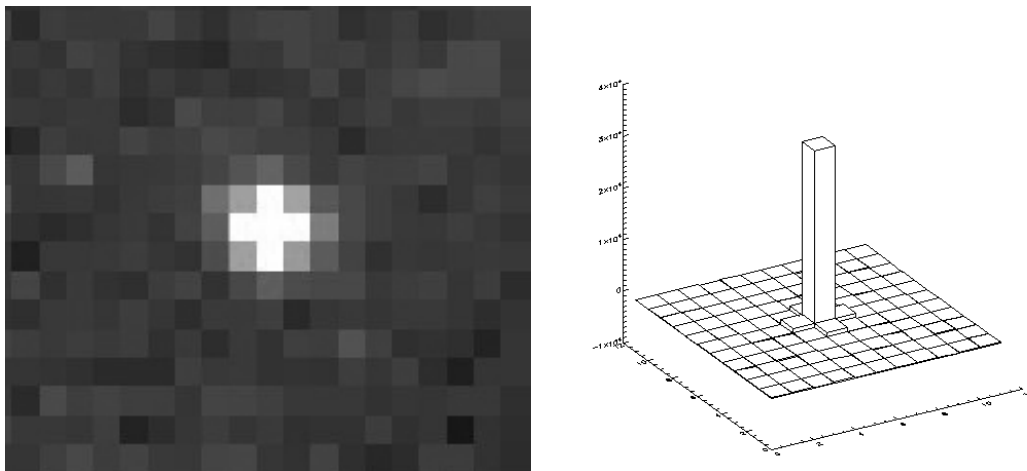


Figure 2.1 A sample image of an optical spot projected onto the detector (left) and the surface plot of the pixel levels around the optical spot.

2.3 Single pixel reset

For hybridized arrays, the HAWAII-RG multiplexers are widely used in the readout circuitry. This type of multiplexer has a unique feature, the guide mode, which is employed for telescope guiding and correction of fast image motion induced by atmospheric turbulence. In the operation of this guide mode, we can read out the full array and a small portion of an array simultaneously at different frame rates. The size of the subarray is changeable by adjusting the guide window. As the reset of the small window can be controlled independently from the full frame, the feature was used to measure interpixel coupling directly (Finger et al. 2006). When the size of the guide window is changed to a single pixel, which is reset at a much higher frequency than the full array, and the full array is uniformly illuminated, the integration time for the guide window pixel is much shorter than the full array and can be almost zero. Therefore, the signal of the guide pixel will be close to zero, whereas all the other pixels will have a large charge signal and be uniform, supposedly. If capacitive coupling did not exist, the pixels close to the guide window pixel will also have the same signal as those far from the guide pixels. In practical cases, these neighboring pixels show different signals. This indicates the existence of a crosstalk, which reduces the signal of those neighboring pixels, and adds to the guide window pixel. As the guide pixel is frequently reset during the integration, the contribution from charge diffusion and optical crosstalk will be significantly reduced and be negligible. The most possible component contributing to the crosstalk is from interpixel coupling. The difference of two images, one captured without resetting the guide window pixel, and one captured with the reset of the guide window

pixel, will be the impulse response induced by capacitive coupling. A sample difference image will be similar to the one displayed in Figure 2.1. This will give us a good direct measurement of interpixel coupling, which is separated from charge diffusion and optical crosstalk as the coupling only occurs after the charge carriers are collected. However, the single pixel reset method is very sensitive to the readout speed. The video signal needs to be settled for sufficient time, which will reduce the residual signal. The experiments performed by Finger et al. (2006) show that the measured value of interpixel coupling was smaller in the fast readout direction than in the slow readout direction. This variation poses extra uncertainty on the IPC measurement.

2.4 F55 bombardment

A Fe55 source is widely used in the characterization of scientific image detectors, e.g. conversion gain and charge transfer efficiency in CCD (Howell 2000). Fe55 is a well-calibrated radioactive X-ray source. It emits a large amount of K_{α} photons with energy of 5.9 keV (80%), and additional K_{β} photons with energy of (20%). Impacting the detectors, the X-ray photon may be absorbed, producing a charge cloud with size proportional to the energy of the X-ray photon. It is experimentally shown that the absorbed 5.9 keV and 6.5 keV X-rays will free 1620 and 1778 electrons, respectively with about 13 electrons Fano noise. As it is difficult for the X-rays to penetrate a fused silica window, the source is usually placed directly in front of detector arrays. A typical image with Fe55 illumination is presented below in Figure 2.2. Pixels are exposed in dark except those absorbing X-ray photons. Therefore, the neighbors of X-ray events are

supposed to have only dark signal. Identifying the isolated single events and analyzing the pixel signal surrounding them, the coupling magnitude can be estimated in the same manner as the single pixel reset and spotomatic methods as stated in Sec. 2.2 and 2.3.



Figure 2.2 A portion of a frame illuminated by the Fe55 X-ray source with Al foil attenuation.

2.5 Reset bias V_{reset}

Seshadri et al. (2007) and Hanold et al. (2007) reported IPC measurements through high reset voltage in the IR and Si-PIN arrays, respectively. The approach is to reset a specific single pixel to a high voltage, e.g. 1 V while its neighbors do not experience such a high reset. In a typical hybrid detector where the substrate bias does not change and is higher than the reset level, the high voltage reset reduces the potential difference across the photodiode. This mimics the process wherein a photodiode collects photoelectrons and the voltage across the photodiode decreases. In other words, the pixel experiencing high

reset is characteristic of collecting signal charge. This mimic charge signal will redistribute around the center pixel by electric induction, and a portion will appear in adjacent pixels if capacitive coupling exists. Like the methods of signal pixel reset and optical spot illumination, the high voltage reset of single pixels also generates single isolated events that have strong signal. The signal in the neighbors gives us information on interpixel coupling. As we can see, one advantage of this approach is that it does not suffer from diffusion effect and optical crosstalk, because there is no photon strike and thus no photocharge generated. The measured crosstalk is all from capacitive coupling. However, this method is only applicable to the arrays with special readout modes, and implementing the experiment is complicated. Therefore, this is not a common method to measure IPC. So far, it is still in the test stage.

2.6 Cosmic ray event (CRE)

Primary Cosmic rays are high-energy radiations and particles from the solar system and beyond, e.g. protons and cosmic ray ions. Near the bottom of the atmosphere genuine cosmic rays consist almost exclusively of relativistic muons produced by secondary meson decay (Groom 2002). When a muon with high energy strikes a pixel, it can generate a huge number of electron-hole pairs such that the pixel reaches a very high level or even saturates suddenly. Depending on the incident angle and energy level, the muon particle may strike through a few pixels and create a cluster of bright pixels. Cosmic rays are a serious problem in space imaging applications, especially for CCD imagers. However, these special events can be used to measure electrical crosstalk, either

diffusion or capacitive coupling. In a similar fashion to the method dependent on single events, we estimate the coupling amount of neighboring pixels identifying isolated single cosmic ray events and analyzing the signal level in adjacent pixels.

In astronomical applications, the sampling up-the-ramp (UTR) is one of the widely-used sampling strategies, see Appendix B. It includes repeated sampling of the pixels. In this technique, the signal levels are read continuously for the entire integration time with the same interval, and then fit to a straight line. Cosmic ray events can be efficiently identified in the fitting process, see the details describing the procedure in Chap. 5. The identified independent cosmic events can be used to measure the IPC magnitude. For a typical pixel, its signal values in the sequence frames appear to form a straight line, as shown in Figure 2.3, where there are eight continuous samplings and the first sampling has been subtracted from each of the following samplings (same for other plots).

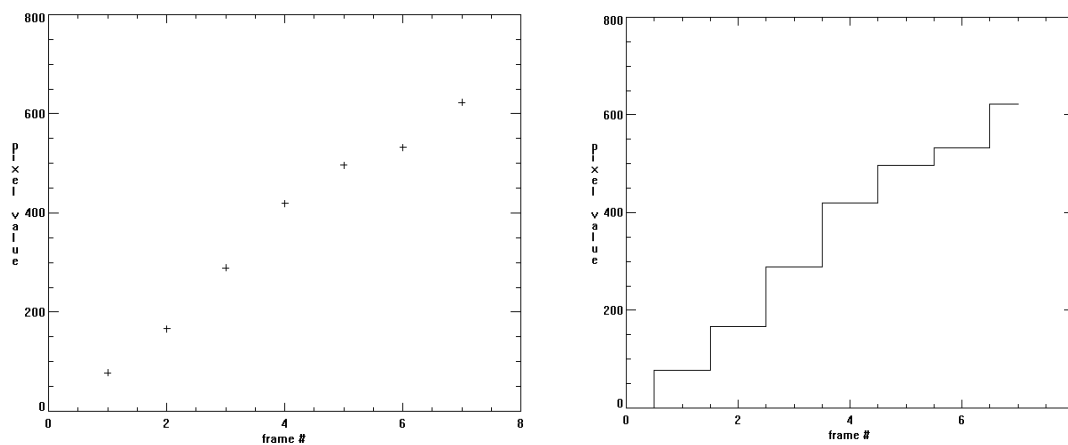


Figure 2.3 Right: Up-the-ramp readouts for a typical pixel (plus sign); right: histogram mode.

However, if a cosmic event hits a pixel, the sampling value will appear quite different.

Figure 2.4 (left) shows the up-the-ramp sampling of a pixel hit by a typical cosmic event, where the pixel signal will jump to a very high level suddenly and keep almost unchanged over the integration. From the dramatic change of pixel level we can determine when the cosmic event hits the detector among the readout sequence. Subtracting the preceding frame from the frame where the cosmic event appears, we would obtain a distribution of pixel values around the pixel hit by the cosmic event, as shown in Figure 2.4 (left). The signals surrounding the central pixel can be used to estimate capacitive coupling. Note that the surface plot of a hot pixel and its surroundings appears not much different from a cosmic ray event, as indicated in Figure 2.4 (right). However, the plot of all the samplings in a hot pixel should look like that in Figure 2.3, except that the increment amount in the sequence is much bigger.

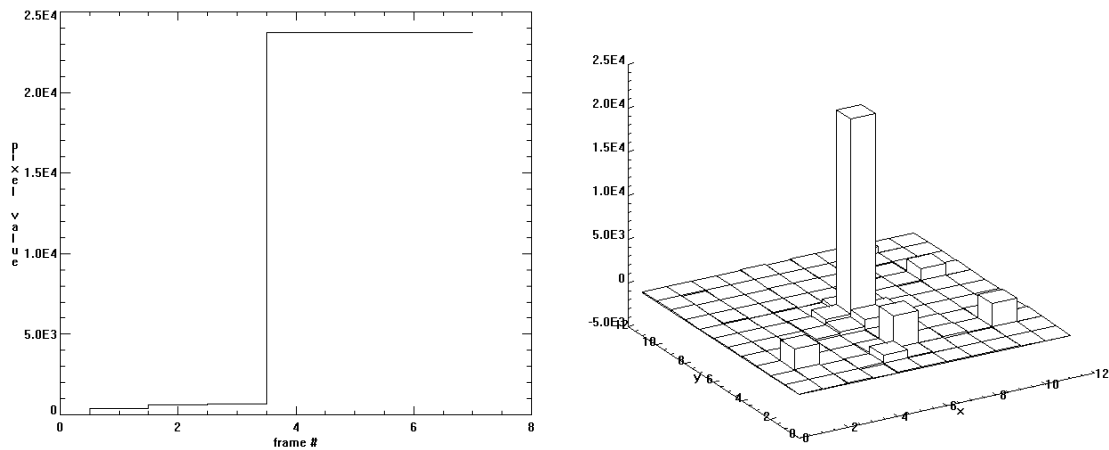


Figure 2.4 Left: up-the-ramp samplings for a typical pixel hit by CRE (histogram mode); right: Pixels around the pixel hit by CRE in a difference frame.

The procedure to measure the IPC is listed below:

- 1) Identify potential hot pixels and cosmic events based on some threshold, e.g. 3σ .
- 2) Identify all the potential hot pixels according to the feature of consistent big

increment in pixel levels and remove them.

- 3) Select non-isolated single cosmic events (events where their neighbors also are potential cosmic events). Keep only isolated single cosmic rays.
- 4) Calculate IPC magnitude using the pixels surrounding each isolated cosmic event. Take average for all the IPC estimates.

The detailed criteria to identify CREs and hot pixels are presented in Chap. 5. One concern for the CRE method is that the coupling amount includes not only interpixel coupling, but diffusion crosstalk. It therefore gives us an upper limit on the coupling magnitude due to interpixel capacitance.

2.7 Hot pixels

Hot pixels are the pixels with very high dark current compared to normal pixels in an image array. Defects or impurities in a semiconductor material, e.g. Si, introduce electronic states in the forbidden gap which acts as steps between the valence and conduction bands, providing paths for valence electrons jumping into the conduction band. The hot pixels increase the mean dark rate and dark signal non-uniformity, and thus degrade image detector performance. For typical detector materials, e.g. Si and HgCdTe, dark current varies depending on the detector temperature. It increases dramatically as the temperature become higher (Theuwissen 1995). At a fixed temperature, dark signal accumulates linearly with integration time. Figure 2.3 shows the relationship of a typical dark signal vs. exposure time. The slope is usually defined as dark current in bits or electrons per second. For a hot pixel, the slope is several times higher than mean dark rate.

Based on this key point, hot pixels can be identified from the dark frames sampled up-the-ramp. The difference from cosmic ray events is that the signal level increase is consistent from frame to frame, whereas cosmic ray event pixels experience a sudden jump or saturation in a short time. The detailed procedure to identify hot pixels and cosmic ray events are described Chap. 5. One big advantage using hot pixels is that they do not suffer from diffusion crosstalk as there is almost no photocharge generated. Furthermore, most of dark signal charges are generated close to the boundaries of the pixel depletion region, so it is easier for those charges to be collected within the pixel where the charges are generated instead of diffusing into neighboring pixels thermally.

3 Impact of IPC on astronomical photometry

3.1 Photometry in astronomy

Astronomical photometry is a technique of measuring the flux, or intensity of an astronomical object's electromagnetic radiation. Usually, photometry refers to measurement over a specific wavelength band of radiation, e.g. near IR, optical, etc; however, when both the amount of radiation and its spectral distribution are measured, it is termed spectrophotometry.

Photometry is conducted by collecting radiation from target objects by a telescope passing through some specialized filters, and then capturing and recording the light energy with a photosensitive instrument, e.g. photometers. Initially, photometry in the near IR through long-wavelength UV bands was done with a photoelectric photometer, an instrument that measured the light intensity of a single object by directing its light onto a photosensitive cell. In the visible spectral range, this technique has almost been replaced with modern digital cameras, e.g. CCD and CMOS imagers, which can simultaneously image multiple objects, though photoelectric photometers are still used in some special situations, such as where high time resolution is required (Sterken and Manfroid 1999, Romanishin 2002).

When using a CCD or CMOS camera to do photometric measurement, there are different ways to extract the photometric measurement (e.g. the magnitude of a star) from the raw image. The observed signal is usually convolved over many pixels by the system

point spread function. This may be due to the point spread in the telescope optics, the detector array, astronomical seeing, etc. When measuring the total flux from a point source, we need to add up all the light from the object and subtract off the sky background. The simplest technique, adding up the pixel counts within a circle entered on the target object and subtracting off an average sky count, is known as aperture photometry, as illustrated in Figure 3.1. When doing photometric measurement in a very crowded field, such as in a globular cluster, where the profiles of stars overlap significantly, one must use deconvolution techniques, such as point spread function fitting, to determine the individual fluxes of the overlapping sources (Sterken 1999, Romanishin 2002).

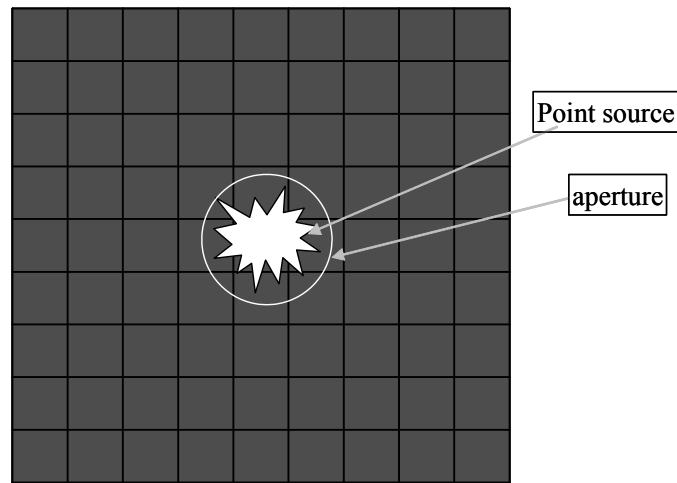


Figure 3.1 Illustration of aperture photometry for an astronomical object.

After determining the flux of an object in digital counts, astronomy researchers usually calibrate the measurement such that the photometry is differential, relative, or absolute. Differential photometry is the measurement of changes in the brightness from an object over time; These measurements are compiled into a light curve of the object.

Relative photometry is the measurement of the apparent brightness of multiple objects relative to each other. Absolute photometry is the measurement of the apparent brightness of an object on a standard photometric system. These measurements should be consistent with other absolute photometric measurements obtained with different telescopes or instruments. The absolute photometric measurement can be combined with the inverse-square law to estimate the luminosity of an object if its distance is known.

To get the total flux of a source, the missing flux outside the aperture needs to be corrected through calibration. Ideally, no flux is missing outside the specified aperture, and the aperture covers all the flux from a source. Several mechanisms can cause the flux spreading around a source, e.g. optical aberration, diffusion, interpixel coupling. If interpixel coupling exists, a portion of the total signal within a specified aperture will flow out into its neighbors, thus reducing the measured flux in the aperture. The measurement appears smaller than the real value. An extreme example is illustrated in Figure 3.2 below, where the aperture encloses only the central pixel, which encloses a point source, and the surrounding region is dark. When the image passes through a capacitive coupling, this causes a measurement error in the total signal within the aperture. The filter $h_{ipc}[x, y]$ from interpixel coupling is written as follows:

$$h_{ipc}[x, y] = \begin{bmatrix} 1 & 2 & 1 \\ 2 & 88 & 2 \\ 1 & 2 & 1 \end{bmatrix} \times \frac{1}{100}$$

The point source image before and after the IPC filter will appear as shown in Figure 3.2 below. It is obvious that the total flux measured in the aperture drops from 100 ADU to 88 ADU. There is a 12% percent error though the coupling amount to nearest neighbors is

only 2%. In practical cases, the error should be smaller, but we should correct this uncertainty for precise photometric measurement.

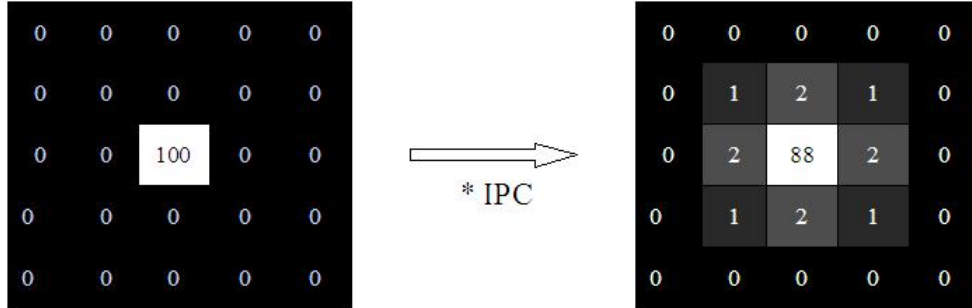


Figure 3.2 Illustration of photometric image suffering from interpixel coupling.

3.2 Modeling IPC's impact on photometry

The effect of interpixel coupling can be modeled as a convolution process as it is deterministic. Applying linear filtering theory, the IPC can simply be taken as another component of the total point spread function (PSF) of the detector array—a strong point source will spread out somewhat. Assume the IPC component of PSF is $h_{ipc}[x, y]$ and the original signal image is $f[i, j]$ where i and j denote the pixel position, the resulting signal $f'[i, j]$ will be the convolution of $f[i, j]$ with $h_{ipc}[x, y]$, ignoring the readout noise.

$$f'[i, j] = f[i, j] * h_{ipc}[i, j] \quad (3.1)$$

$$H_{inv}[\xi, \eta] = \frac{1}{FT^{-1}\{h_{ipc}[i, j]\}} \quad (3.2)$$

So we can accurately correct the measured image signal as well as the photometrical

measurement by applying an inverse filter $H_{inv}[\xi, \eta]$ if the magnitude of interpixel coupling is well known. However, when the image signal-to-noise ratio (SNR) is low and thus read noise is not negligible, the inverse filter may not be a good choice to deconvolve the blurred image. Instead, a Wiener filter $H_{wiener}[\xi, \eta]$ is supposed to restore the blurred image better as it was derived by minimizing the total squared error of the recovered image signal $f'[i, j]$ compared to the correct signal $f[i, j]$ (Helstrom 1967). When the additive noise (read noise) is negligible, the Wiener filter reduces to the inverse filter as indicated in Eq. 3.4.

$$f'[i, j] = f[i, j] * h_{ipc}[i, j] + N_{rd}[i, j] \quad (3.3)$$

$$H_{wiener}[\xi, \eta] = \frac{H^*[\xi, \eta]}{|H[\xi, \eta]|^2 + \Gamma[\xi, \eta]}, \Gamma[\xi, \eta] = \frac{|N_{rd}[\xi, \eta]|^2}{|F[\xi, \eta]|^2} \quad (3.4)$$

3.3 Simulation of the impact of IPC on photometry

Based on the model described above, we simulate the filtering process that interpixel coupling introduces. The flowchart in Figure 3.3 shows how the simulation is conducted. The input source image is a re-sampled airy pattern. We measure the signal within the aperture that encloses most flux in the airy disk ($\sim 80\%$ of total flux). This flux is the true signal, F0. After shot noise and dark current are added to the source image, the measured signal in the aperture is F1; F1_conv is the signal when the noisy image passes through the IPC filter; then read noise is added to the convolved image and signal F2 is obtained. Finally, the image is deconvolved by an inverse and wiener filter and the signal in this

stage is denoted as F3. We can see if the signal can be recovered to the stage before the smoothing effect due to interpixel coupling.

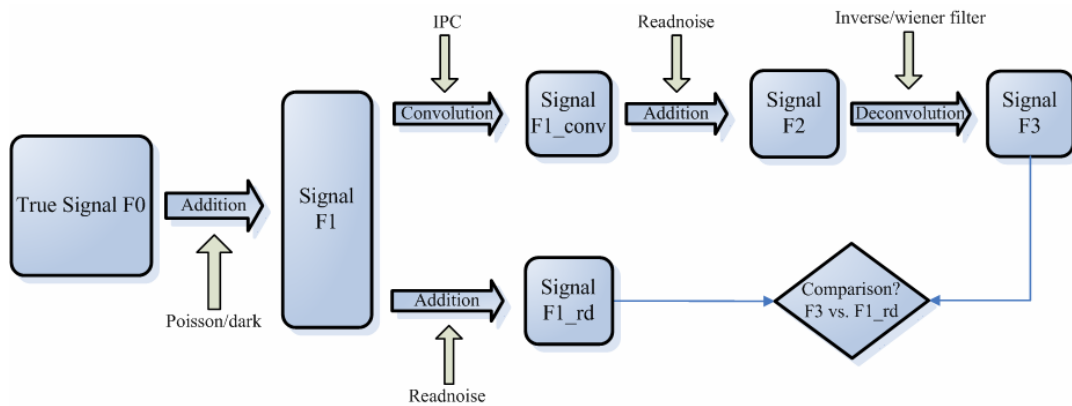


Figure 3.3 Workflow of the simulation process.

The simulation was coded in Interactive Data Language (*IDL*) (Stern 1977). Figure 3.4 (left) below shows the ideal airy pattern. This pattern is re-sampled to a size of 19×19 pixels as shown in Figure 3.4 (right), where the airy disk takes approximately the central 4×4 pixels. The re-sampled pattern is the input image of the whole simulation process. The aperture is selected to surround the airy disk center and has a size of 3×3 pixels. True signal F0 is obtained by summing the pixel signals within the aperture, which accounts for most energy ($\sim 80\%$) from the airy pattern.

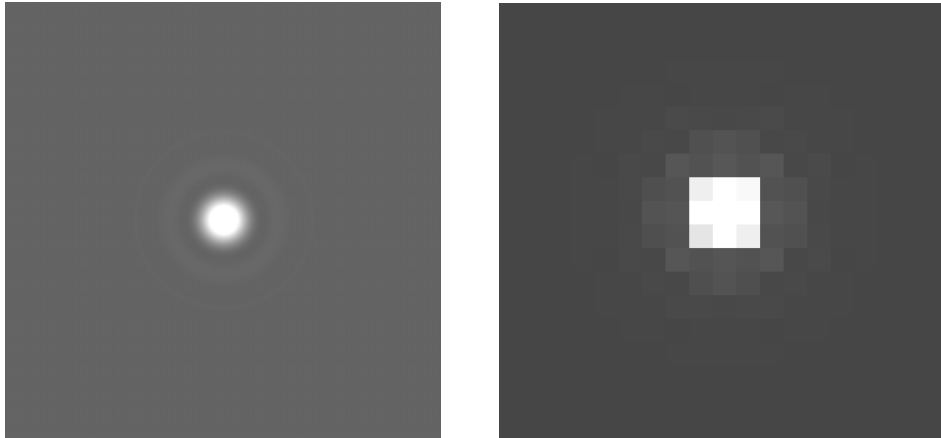


Figure 3.4 Left: image of ideal airy pattern; right: image of re-sampled airy pattern with a size of 19×19 pixels (zoomed in).

In the simulation, the re-sampled pattern was scaled such that the true signal F_0 varied in the range from 4000 to 10 digital counts (ADU). We need to see how the deconvolved signal F_3 changes with respect to the signal without IPC filtering F_{1_rd} over these signal levels. Besides the true IPC h_0 , six error IPC kernels were tried in the deconvolution. The error IPCs are chosen according to Eq. 3.5 below. Both inverse and Wiener filters were used to deconvolve the blurred image pattern. All the results are listed in Table 3.1 and Table 3.2. However, in Figure 3.5 only the results from deconvolution kernels h_0 , $h_{0.5}$, and h_1 are presented. h_{0inv} and $h_{0Wiener}$ mean the true IPC magnitude is employed in the deconvolution, with the inverse and Wiener filter, respectively.

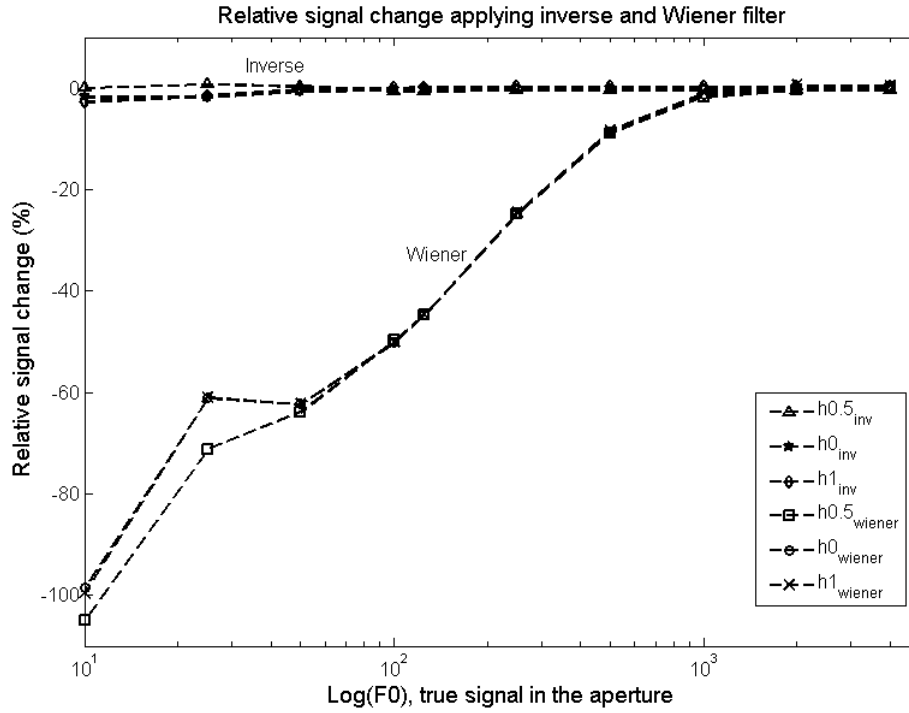


Figure 3.5 Comparison of signal change after the inverse and Wiener filters are applied. Relative signal change after deconvolution is referred to signal without IPC, i.e. F3 to F1_rd.

$$h_i = \begin{matrix} x_1 & x_0 & x_1 \\ x_0 & 100 & x_0, x_0 = i, x_1 = \frac{i}{2} \\ x_1 & x_0 & x_1 \end{matrix} \quad (3.5)$$

$$\text{So } h_{0.5} = \begin{matrix} 0.25 & 0.5 & 0.25 \\ 0.5 & 100 & 0.5 \\ 0.25 & 0.5 & 0.25 \end{matrix}, \text{ and } h_1 = \begin{matrix} 0.5 & 1 & 0.5 \\ 1 & 100 & 1 \\ 0.5 & 1 & 0.5 \end{matrix}$$

Throughout the simulation, the input IPC h_{ipc} stays unchanged, as shown below. The level of input Airy pattern is adjustable and scaled such that the signal F0 in the aperture is 4000, 2000, 1000, 500, 250, 125, 100, 50, 25, and 10 ADU. The dark current used is 3 ADU per pixel and read noise is 10 ADU per pixel (for simplicity, I assume a conversion

gain of 1 e⁻/ADU).

$$h_{ipc} = h_0 = \begin{bmatrix} 0 & 1.3 & 0 \\ 1.5 & 100 & 1.5 \\ 0 & 1.3 & 0 \end{bmatrix}$$

Figure 3.5 indicates that both filters work very well at high signal levels, however, the Wiener filter performs much worse than the inverse filter at low signal levels. Therefore, we just consider the inverse filter in our simulation presented in the following.

At each level of the true signal F3, seven deconvolution kernels, $h_{0.5}, h_0, \dots, h_5$, were attempted to deblur the noisy image, as shown in Figure 3.6 and Table 3.1. These kernels are defined in Eq. 3.5 above. Figure 3.6 shows how the recovered signal changes relative to the sampling signal if there were no IPC effect. It can be seen that the signal can be recovered very well if the magnitude of IPC is accurately measured. With the increase of the coupling amount in the deconvolution filters, the restored signal gets stronger and will surpass the input signal finally. That is expected as a deconvolution kernel here is used to restore the smoothing effect due to interpixel coupling. The signal out of the aperture due to interpixel coupling is supposed to be pulled back into the aperture after the deconvolution. A deconvolution kernel having a large coupling amount to neighboring pixels will pull more signal back into the aperture than it actually is. Therefore, the relative signal change becomes larger and larger when the kernel changed from $h_{0.5}$ to h_5 , where the coupling amount increases continuously. However, there is a steep decrease in the relative signal change when the input signal becomes very small, e.g. 10 and 25 ADU, where the read noise dominates the signal and thus noise is pulled back into the aperture after deconvolution. The zero-mean noise makes the signal in the

aperture small. This may explain this trend at low signal levels.

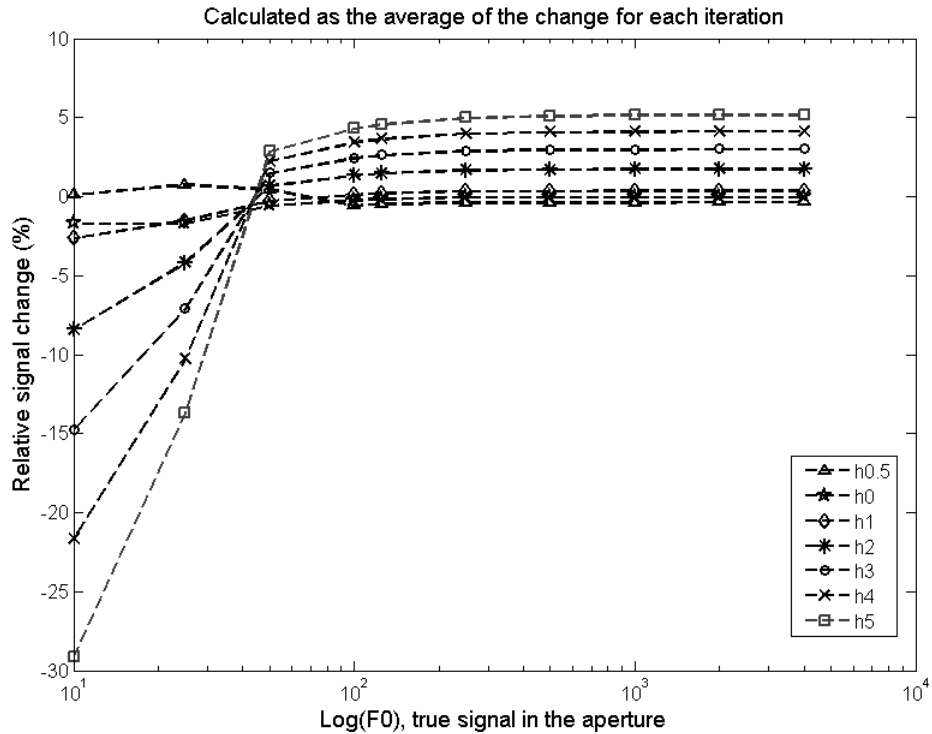


Figure 3.6 Relative signal change in the aperture at different input signal levels after inverse filter was applied. Seven deconvolution kernels of different coupling amounts were tried at each input signal levels, including the true IPC. Relative signal change after deconvolution is referred to the signal w/o the IPC effect, i.e. F3 to F1_rd. See flowchart for descriptions.

Table 3.1 Results of relative change of signal at different levels through inverse filtering.

F0 (ADU)	$h_{0.5}$ (%)	h_0 (%)	h_1 (%)	h_2 (%)	h_3 (%)	h_4 (%)	h_5 (%)
4000	-0.34	0.00	0.39	1.76	3.01	4.15	5.19
2000	-0.34	0.00	0.39	1.76	3.01	4.15	5.19
1000	-0.34	0.00	0.39	1.75	3.00	4.14	5.18
500	-0.35	-0.01	0.38	1.73	2.97	4.10	5.12
250	-0.36	-0.03	0.35	1.68	2.90	4.00	5.00
125	-0.45	-0.12	0.24	1.50	2.63	3.65	4.57
100	-0.54	-0.22	0.14	1.37	2.47	3.45	4.32

50	0.48	-0.53	-0.23	0.70	1.52	2.25	2.89
25	0.78	-1.68	-1.49	-4.17	-7.10	-10.27	-13.68
10	0.12	-1.70	-2.61	-8.40	-14.74	-21.64	-29.10

Table 3.2 Results of relative change of signal at different levels through Wiener filtering.

FO (ADU)	$h_{0.5}$ (%)	h_0 (%)	h_1 (%)	h_2 (%)	h_3 (%)	h_4 (%)	h_5 (%)
4000	-0.19	0.17	0.57	2.02	3.36	4.61	5.77
2000	-0.20	0.19	0.60	2.12	3.54	4.88	6.15
1000	-1.70	-1.33	-0.93	0.54	1.91	3.21	4.44
500	-8.88	-8.64	-8.33	-7.24	-6.22	-5.28	-4.40
250	-24.83	-24.66	-24.51	-23.97	-23.49	-23.04	-22.64
125	-44.73	-44.67	-44.62	-44.44	-44.29	-44.14	-44.02
100	-49.65	-50.08	-50.05	-49.93	-49.82	-49.73	-49.65
50	-63.81	-62.26	-62.24	-62.17	-62.11	-62.05	-61.99
25	-71.19	-60.99	-60.93	-60.53	-60.17	-59.85	-59.57
10	-104.96	-98.50	-99.50	-102.07	-104.51	-106.81	-108.98

3.4 Simulation of the impact of IPC on SNR

As a byproduct of the simulation on how IPC affects photometric measurement, the change of signal to noise ratio (SNR) was also studied. Equation 3.6 presents the formula used to calculate SNR. Similar to Figure 3.5, Figure 3.7 shows the performance comparison of inverse and Wiener filters in terms of SNR change for three tested filters $h_{0.5}$, h_0 , h_1 . The results of all attempted filters are listed in Table 3.3 and Table 3.4. It appears that inverse filter works much better than Wiener filter as the inverse filter

introduces less SNR change.

$$SNR = \frac{S_{Aperture}}{\sqrt{S_{Aperture} + N_{pix} \cdot \sigma_{rd}^2 + N_{pix} \cdot dark}} \quad (3.6)$$

where $S_{Aperture}$ is the total signal with the selected aperture; σ_{rd} is readout noise per pixel; $dark$ is dark current signal per pixel; N_{pix} is the number of pixels in the aperture.

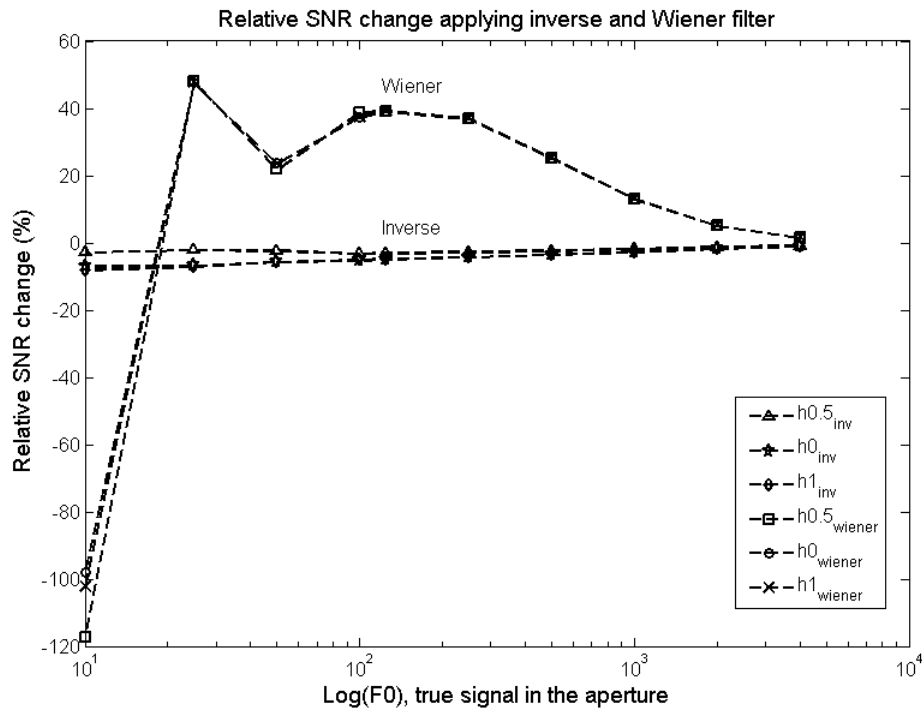


Figure 3.7 Comparison of SNR change after applying the inverse and Wiener filters. Relative SNR change after deconvolution is referred to signal w/o IPC, SNR3 to SNR1_rd.

Table 3.3 Results of relative change of SNR at different levels through inverse filtering.

F0 (ADU)	$h_{0.5}$ (%)	h_0 (%)	h_1 (%)	h_2 (%)	h_3 (%)	h_4 (%)	h_5 (%)
4000	-0.76	-1.06	-0.90	-1.27	-1.76	-2.38	-3.11

2000	-1.16	-1.77	-1.62	-2.66	-3.82	-5.10	-6.50
1000	-1.66	-2.65	-2.52	-4.34	-6.26	-8.26	-10.33
500	-2.17	-3.54	-3.44	-6.02	-8.63	-11.25	-13.89
250	-2.59	-4.26	-4.18	-7.34	-10.46	-13.53	-16.54
125	-2.95	-4.82	-4.77	-8.36	-11.84	-15.23	-18.51
100	-3.10	-5.02	-4.98	-8.67	-12.25	-15.71	-19.07
50	-2.25	-5.55	-5.56	-9.67	-13.59	-17.33	-20.91
25	-2.03	-6.76	-6.88	-14.22	-21.14	-27.67	-33.84
10	-2.72	-6.84	-8.00	-18.09	-27.68	-36.82	-45.55

Table 3.4 Results of relative change of SNR at different levels through Wiener filtering.

FO (ADU)	$h_{0.5}$ (%)	h_0 (%)	h_1 (%)	h_2 (%)	h_3 (%)	h_4 (%)	h_5 (%)
4000	1.50	1.46	1.57	1.67	1.70	1.66	1.57
2000	5.10	5.08	5.18	5.25	5.27	5.27	5.23
1000	13.06	13.05	13.16	13.36	13.54	13.70	13.84
500	25.17	25.26	25.38	25.69	25.98	26.25	26.49
250	36.94	36.99	37.08	37.28	37.46	37.62	37.76
125	39.23	39.10	39.13	39.06	38.98	38.91	38.83
100	38.79	37.35	37.36	37.21	37.06	36.91	36.77
50	21.82	23.68	23.67	23.42	23.20	23.01	22.83
25	48.00	47.70	47.86	49.06	50.09	50.95	51.62
10	-117.16	-98.19	-102.20	-111.76	-120.69	-129.00	-136.69

Figure 3.8 presented a similar plot to Figure 3.6 except that the signal change was replaced with SNR. The recovered SNR was compared with the SNR with Poisson, dark current, and read noise added, no IPC filtering. As can be seen, the SNR changes at different signal levels and with different deconvolution kernels. The deconvolution kernel

with a big coupling always made the relative SNR change large, as shown in Figure 3.8. This may be explained as the deconvolution is a sharpening process according to those kernels we used. The operation of deconvolution sharpened not only the image but the noise. Bigger coupling would cause a larger noise sharpening and thus a smaller SNR.

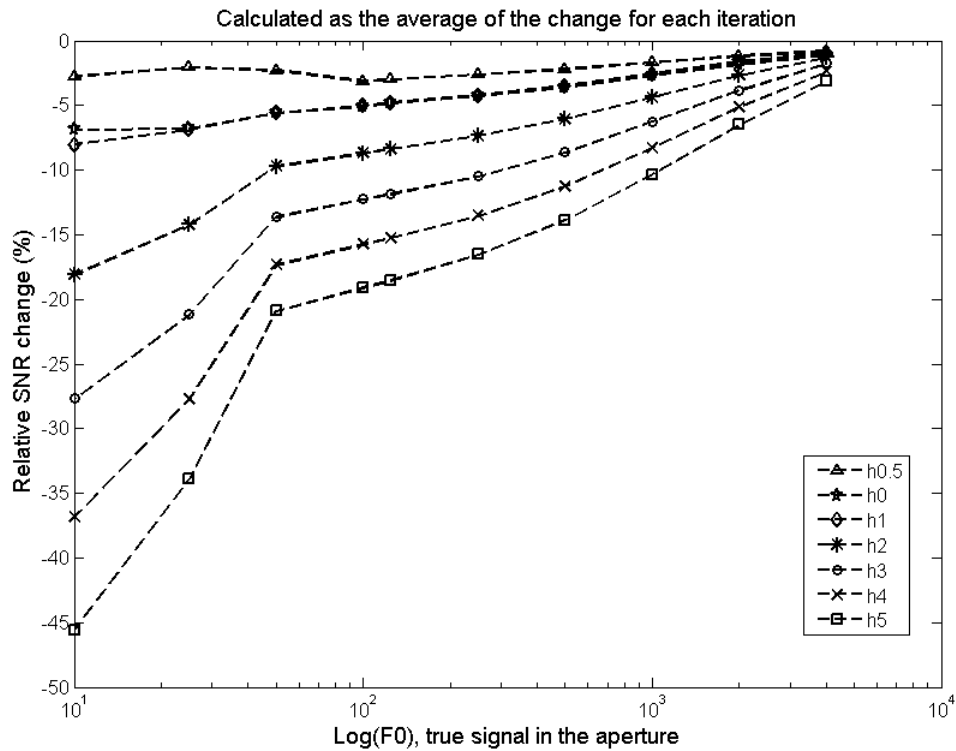


Figure 3.8 Relative SNR change at different signal levels after inverse filter was applied. Relative SNR change after deconvolution is referred to signal w/o IPC, SNR3 to SNR1_rd.

3.5 Summary

In this chapter we simulate the impact of interpixel coupling on astronomical photometry as well as signal-to-noise ratio. With both inverse and Wiener filters attempted to deblur the smoothed image by capacitive coupling, we find that inverse filter performs better,

though Wiener filter is more often used in the restoration of noisy blurred images (Easton 2005). Applying the inverse filter, we calculate the relative change of flux within the aperture at different signal levels while the read noise and dark current keeps constant. That is to say, the performance of recovering flux measurement through inverse filter is studied at various signal-to-noise levels. The results indicate that the flux measurement can be restored within an uncertainty of 2%, provided that we have full IPC knowledge. In the recovered image, the SNR can reach a loss of 6% at low signal level, and less than 1% at high signal level.

4 Interpixel coupling and read noise

It is widely believed that IPC occurs in the space between the detector array and multiplexer between indium bumps (Finger et al. 2006, Brown et al. 2006, Bai et al. 2007). In Si-PIN detectors, coupling can also exist in the diode array between photodiodes. Both of the two mechanisms suggest that interpixel coupling occurs before read noise is introduced. Besides the detector array and the space between indium bump interconnects, mutual capacitance may also occur inside the readout integrated circuit (ROIC), where the noise signal may couple capacitively to their neighbors (Brown et al. 2007). If this occurs, the readout noise would be attenuated in a similar fashion to Poisson noise, and become spatially correlated. This chapter will address the read noise related coupling.

4.1 Read noise

Read noise is a noise component associated with each signal read. It is a temporal noise and introduced during the signal readout. Read noise is the minimum noise level that an image detector usually can reach. Typical sources are from pixel sense node (reset noise), source followers (thermal and 1/f flicker noises), and column amplifier (thermal noise) (Theuwissen 1995). Read noise can be measured in the total dark, where other temporal noises are negligible, e.g. Poisson noise. As compared to Poisson noise or photon noise, which is inherent of photons and electrons and is unavoidable, read noise is closely

related to the measuring systems since any instrument has certain uncertainties. Therefore, readout noise can be reduced to an acceptable level by optimized design.

4.2 Modeling of read noise and IPC

To investigate the read noise related coupling, we focus on images that are dominated by read noise. To this end, bias frames, dark frames with minimum exposure, are used. A bias frame can be expressed as follows if the read noise is not polluted by capacitive coupling.

$$bias[i, j] = offset[i, j] + dark_{\min}[i, j] + readnoise[i, j] \quad (4.1)$$

where the signal of each pixel is composed of the offset, minimum dark signal, and readout noise. Ideally, read noise is spatially uncorrelated between adjacent pixels. If interpixel coupling affects read noise in the same manner to photon noise discussed in Chap. 1 and 2, readout noise will be smoothed. Thus Eq. 4.1 is rewritten as follows.

$$bias[i, j] = (offset[i, j] + dark_{\min}[i, j] + readnoise[i, j]) * h_{ipc}[i, j] \quad (4.2)$$

Interpixel coupling is modeled as a low-pass convolution kernel $h_{ipc}[i, j]$ as discussed in previous sections. Note that the coupling magnitude here should be smaller than interpixel coupling measured by cosmic ray events or hot pixels as only the coupling from within the multiplexer and even post-readout circuitry is considered, whereas the coupling discussed before comes from the space between photodiode array and

multiplexer between In bumps, and between neighboring photodiodes. Neglecting minimum dark signal and differencing two bias frames, we obtain

$$D[i, j] = bias1[i, j] - bias2[i, j] = ([readnoise1[i, j] - readnoise2[i, j]] * h_{ipc}[i, j]) \quad (4.3)$$

where $D[i, j]$ is the difference of two bias frames. The difference of any two bias frames cancels out the offset, leaving only the difference of read noise, whose variance is twice the variance of the original readout noise component.

The autocorrelation of the difference image is equal to the correlation of impulse response with itself, scaled by the variance of read noise component in the bias frames, as shown below.

$$R_D[x, y] = 2\sigma_{RD}^2 h_{ipc}[x, y] * h_{ipc}[-x, -y] \quad (4.4)$$

If interpixel coupling does not exist among read noise, $h_{ipc}[x, y]$ equals an ideal 2-D delta function $\delta[x, y]$. The resulting autocorrelation function will not present any term in the neighbors, except a peak in the center, which corresponds to the correlation without any shift, as shown below in Figure 4.1. Simulation shows this result and the one smoothed by a small low-pass filter.

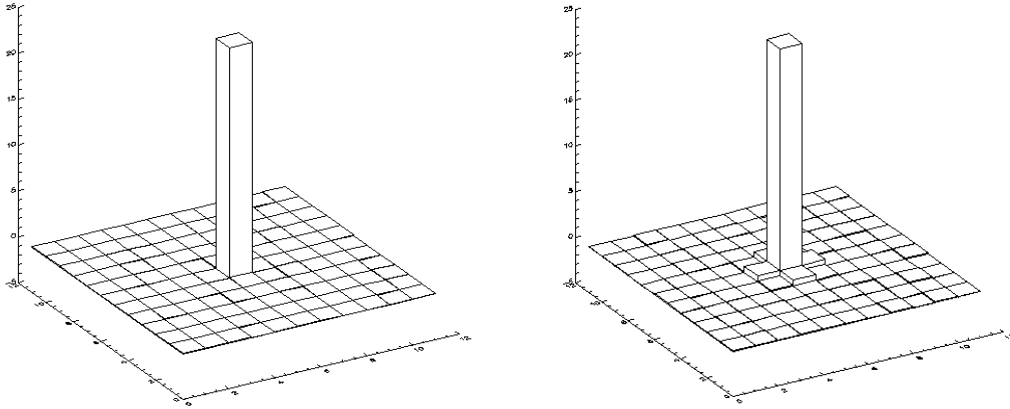


Figure 4.1 Left: autocorrelation of an ideal Gaussian noise image with zero mean and $\sigma = 5$ DN; right: autocorrelation of same noise image but convolved with a low-pass filter.

To check whether the read noise is affected by capacitive coupling, we analyzed the bias frames taken from two types of arrays, H2RG HgCdTe IR and H4RG Si-PIN detectors (Figer et al. 2004, Simms et al. 2007). Bias frames from Si-PIN arrays may be better to test this effect as the Si-PIN detector has a much larger IPC magnitude than the IR counterpart, and thus we can see the effect more easily if IPC has some coupling effect on read noise. In the up-the-ramp read mode of dark frames, where the sampling interval is the read time of a frame, the first sample is the pedestal frame and the second is the dark frame with minimum dark exposure. A bias frame can be obtained by differencing the second and first frames. The data we used were a series of bias frames reduced from the test data in total dark. At each detector temperature, there were usually several up-the-ramp dark experiments, each of which would give us one bias frame. Averaging N bias frames, we get a mean bias frame, the noise of which is reduced to $\frac{1}{\sqrt{N-1}}$ of the original read noise. The mean bias is subtracted from each individual bias, leaving almost

only the read noise component due to minimum dark exposure (The read noise from both H2RG HgCdTe IR and H4RG Si-PIN is about 100 times the dark signal). By evaluating the autocorrelation function of this mean-subtracted bias frame, we can see the effect of IPC on the read noise component. Below are the results based on test data from the H2RG IR and H4RG Si-PIN detector arrays.

4.3 Autocorrelation of read noise

H2RG IR HgCdTe array

The format of this array is 2048×2048. All the test frames were located at the directory shown in Table 4.1. These data were captured at the detector temperature of 37K. At this temperature, there were six up-the-ramp experiments under dark exposures, each of which included 250 readouts with a time interval of 10.75 sec. This is the read time of one frame and the minimum interval between two consecutive reads. The mean bias was obtained by averaging the six bias frames. A typical mean-subtracted bias frame is shown as follows in Figure 4.2.

Table 4.1 Directories and test data for the test detector array H2RG HgCdTe.

Detector	H2RG HgCdTe
Directory	Rockwell4\H2RG-015-5.0mu\cold1\dktest.9May03\
Data file	initial_dark_*.fits, where * is from 1 to 20

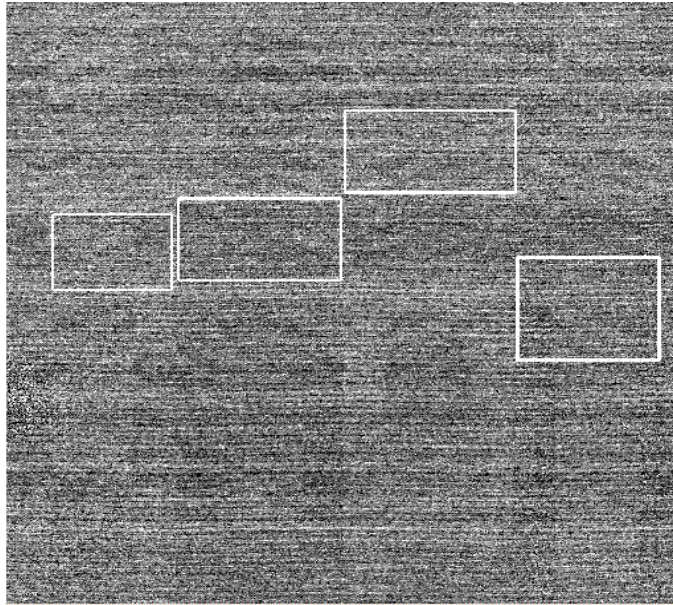


Figure 4.2 A mean-subtracted bias frame from the dark experiments of H2RG IR array at 37 K. The regions chosen are [140:500, 1070:1325], [520:1015, 1100:1380], [1025:1545, 1400:1680], and [1550:1980, 830:1180], as shown by the boxes.

As can be seen, there are obvious non-uniform patterns or fixed patterns, such as column banding structures and row-by-row differences, so calculating the autocorrelation in the whole image will give us misleading results. Instead, several patches of good uniformity were picked out to correlate with themselves. The uniformity of each patch was checked visually. After the autocorrelation of each patch was obtained, an average was taken. Figure 4.3 below presents the resulting autocorrelation function with a size of 21×21 (This means a 10-pixel shift on each direction, i.e., left, right, up, and down).

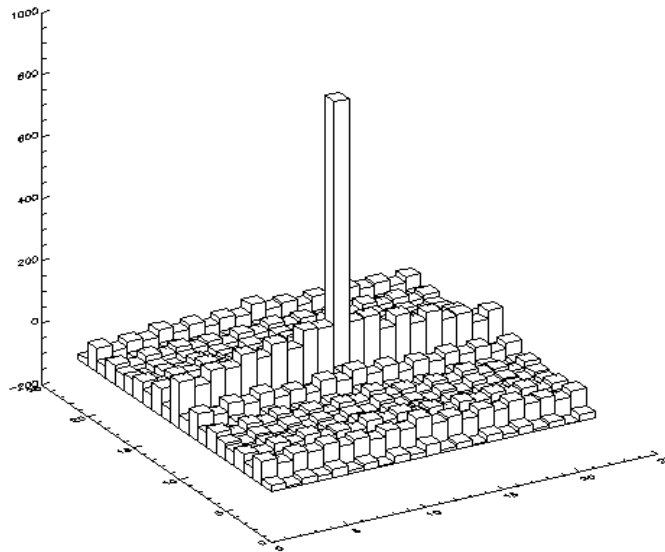


Figure 4.3 2-D autocorrelation of mean-subtracted bias, data taken from H2RG IR, regions of good uniformity used. Same dataset as in Figure 4.2.

As can be seen from the figure above, this autocorrelation function is quite different from what we expect in the ideal case, as indicated Figure 4.1. This may be caused by the residual structures from row to row and column bandings in the mean-subtracted bias image. That made it difficult to get a good 2-D autocorrelation function as each row has quite different means. The column banding also caused some problems in the calculation when the regions chosen spanned across the bandings. To address these problems, we performed 1-D autocorrelation instead, correlating each row or column with itself, then averaged the row and column autocorrelation, respectively. Since the average of each row is quite different, the mean of each row was subtracted before performing the autocorrelation. A similar approach was applied to the columns. All the rows and columns were still from those regions of good uniformity described above. Figure 4.4

below shows the resulting 1-D autocorrelation of the mean-subtracted columns. It is clear that there is no obvious coupling in the neighbors. This verified that IPC does not affect read noise at least in one direction.

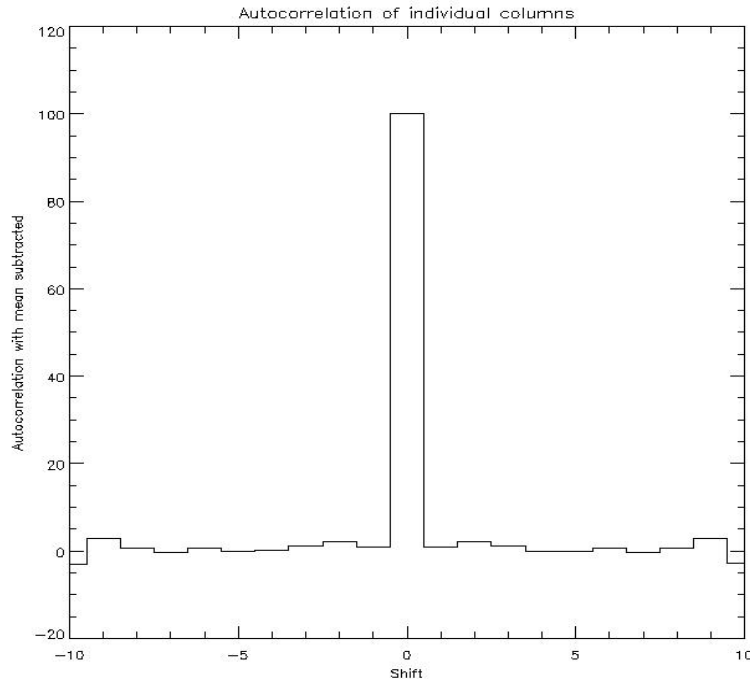


Figure 4.4 1-D autocorrelation of individual mean-subtracted columns. The resulting functions were averaged and scaled to 100 in the center. Test image data are from H2RG IR array. Same dataset as in Figure 4.2.

The column autocorrelation result after being normalized to the peak shown in Figure 4.4 is below.

Table 4.2 Column autocorrelation function with a 10-pixel shift in the -y and +y directions.

Shift (pixel)	value									
-10->-1	-2.91	2.93	0.67	-0.21	0.69	-0.13	0.08	1.26	2.23	0.88
0	100									
1->10	0.85	2.22	1.28	-0.01	-0.11	0.66	-0.23	0.69	2.82	-2.83

After subtracting the DC level, we estimate the correlation is **1.45%** and **1.46%** on the

upper and lower (average of first three in each direction) directions, respectively. From the correlation coefficients, the possible coupling magnitude is just about **0.73%** and **0.78%** according to Eq. 2.4, which gives the lower limit on the IPC magnitude. However, the correlation terms do not decrease smoothly as shown in Figure 4.1 (left). Therefore, this tiny amount of coupling between adjacent pixels cannot be seen as a strong evidence of mutual capacitance within ROIC.

The 1-D autocorrelation result of the mean-subtracted rows is presented in Figure 4.5. As we can see, there is a weak coupling in the neighbors. Also, the correlation does not go down to zero even at 10-pixel shift from the center. This means that there are still residual patterns in the mean-subtracted rows. Good uniformity bias frames, especially row-to-row, may be needed to test the effect further in the horizontal direction.

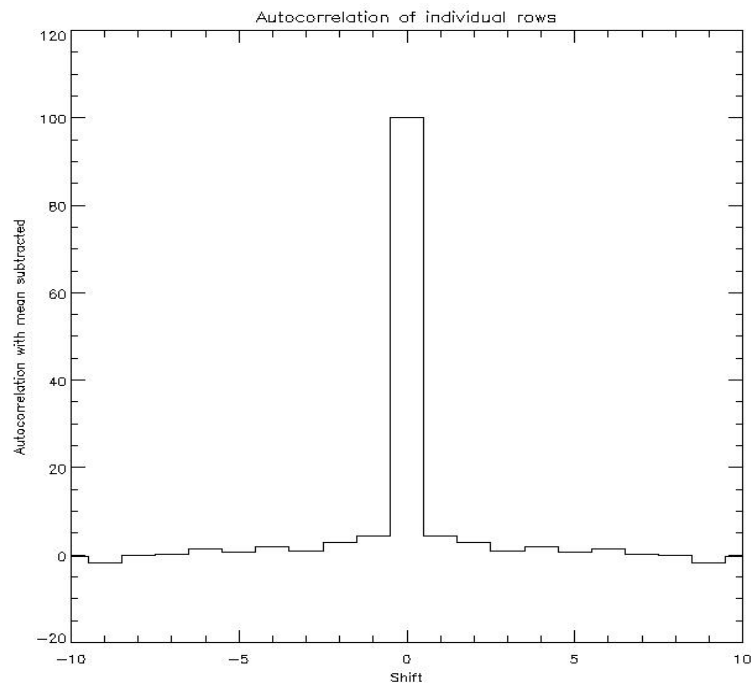


Figure 4.5 1-D autocorrelation of individual mean-subtracted rows. The resulting functions were averaged and scaled to 100 in the center. Test image data are from H2RG IR array. Same dataset as in Figure 4.2.

Table 4.3 Row autocorrelation function with a 10-pixel shift in the -x and +x directions.

Shift (pixel)	value									
-10->-1	-0.30	-1.87	-0.09	0.16	1.39	0.71	1.94	0.89	2.93	4.28
0	100									
1->10	4.27	2.94	0.90	1.91	0.72	1.43	0.19	-0.11	-1.86	-0.28

The row autocorrelation result after normalized to the peak is shown in Table 4.3 and Figure 4.5 above. With the DC level removed, we estimate the correlation is **4.28%** and **4.27%** on the left and right, respectively. From them, the IPC coupling is about **2.14%** and **2.13%** according to Eq. 2.4. The correlation terms from the center goes down gradually, which is similar to that of a theoretically simulated autocorrelation as shown in Figure 4.1 (left). This reasonable 1-D correlation may predict some coupling occurring within the ROIC. However, the coupling amount is even larger than the total crosstalk measured by cosmic ray events or hot pixels, which is around 1.7%. It seems there are other unknown sources contributing to the horizontal correlation. Therefore, we still cannot make any conclusion on the issue. Further experiments and analysis need to verify it.

H4RG Si-PIN array

The format of this array is 4094×4096. The test dark frames we used were taken at 109 K, located at the directory shown in Table 4.4. There were 20 up-the-ramp experiments in total dark exposure, each of which included 8 readouts with a time interval of 5.24 sec.

This is the read time of one frame and the minimum interval between two consecutive reads. We retrieved a bias frame from each of the twenty fits files. The mean bias was obtained by averaging the twenty bias frames. A typical mean-subtracted bias frame is shown as follows, as well as the regions of good uniformity selected for autocorrelation evaluation.

Table 4.4 Directories and test data for the test detector array H4RG Si-PIN.

Detector	H4RG Si-PIN
Directory	RAID1\H4RG-10-007\cold2\ASIC\darkcurrent_test.22Jul07\
Data file	initial_dark_*.fits, where * is from 1 to 20

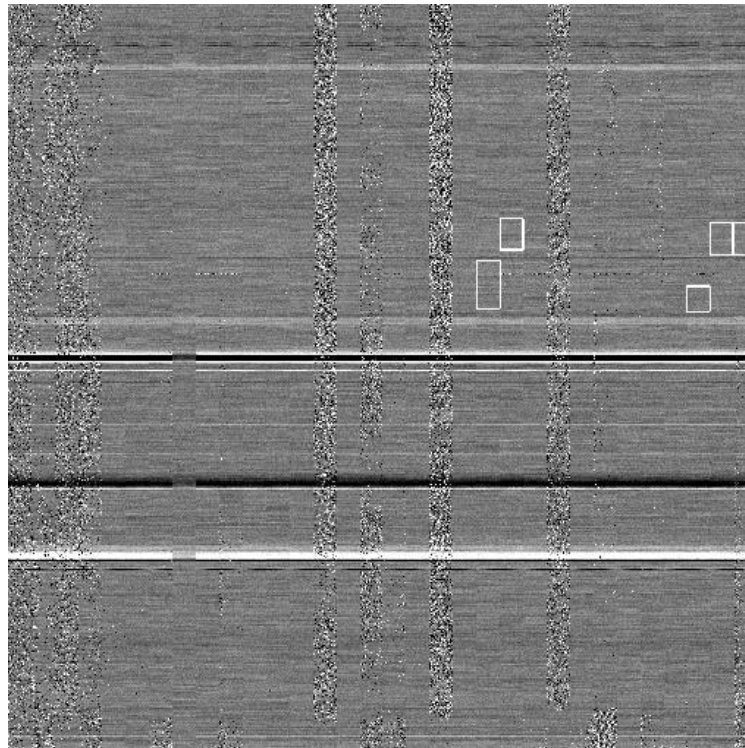


Figure 4.6 A mean-subtracted bias frame: patch of good uniformity chosen chosen, from H4RG Si-PIN array taken at 110 K. The regions chosen are [2560:2688, 2425:2690], [2690:2815, 2535:2695], [3840:3970, 2720:2900], [3970:4095, 2720:2900], and [3460:3584, 2445:2660], as marked by the boxes.

As we can see, there are non-uniform patterns, such as column banding structures and row-by-row differences, so calculating the autocorrelation of the whole image is not good. Similar to that for H2RG IR array, several regions of good uniformity were selected. The uniformity of each patch was checked visually. Each region resided in only one column band. After the autocorrelation of each patch was obtained, we took an average. Figure 4.7 below presented the resulting autocorrelation with a size of 21×21 .

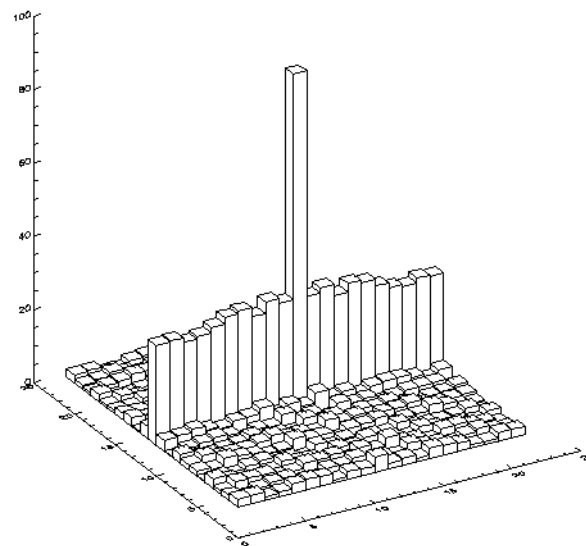


Figure 4.7 2-D autocorrelation of mean-subtracted bias, data taken from H4RG SiPIN array, regions of good column bands used.

In the vertical direction, the function does not change and there is no coupling except a mean level applied to each location. In the horizontal direction, there is a strong coupling, which does not change over various correlation shifts. These strange results may be caused by the distinct residual structures from row to row. So we took the same approach as before to calculate the 1-D autocorrelation of individual rows and columns. The mean

of these individual rows or columns has been subtracted before the correlation operation.

The results are presented in Figure 4.8 and Figure 4.9 as follows.

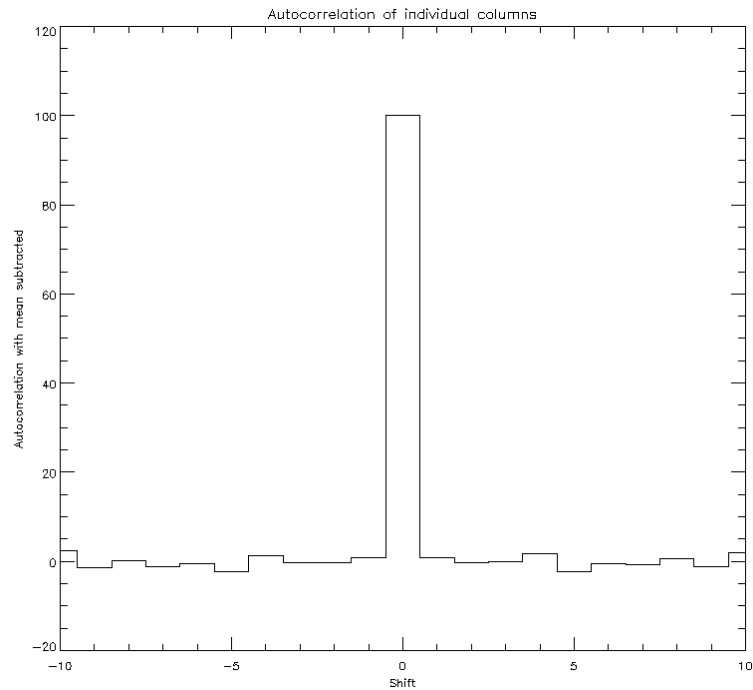


Figure 4.8 1-D autocorrelation of individual mean-subtracted columns. The resulting functions were averaged and scaled to 100 in the center. Test image data are from H4RG Si PIN array.

The column autocorrelation results after normalized to the peak are shown in Table 4.5 and Figure 4.8.

Table 4.5 Column autocorrelation function with a 10-pixel shift in the -y and +y directions.

Shift (pixel)	value									
-10->-1	2.36	-1.44	0.20	-1.25	-0.43	-2.30	1.31	-0.25	-0.39	0.76
0	100									
1->10	0.94	-0.33	-0.17	1.64	-2.20	-0.61	-0.68	0.65	-1.13	2.06

Subtracting the DC level, we estimated the correlation is **0.76%** and **0.94%** on the upper

and lower, respectively. From this, the possible IPC coupling is about **0.38%** and **0.47%**. It gives us a small lower limit on the IPC measurement. However, the correlation terms do not decrease gradually as the theoretical autocorrelation function illustrated in Figure 4.1. Therefore, this small amount of coupling among neighboring pixels cannot be seen as a strong evidence of interpixel coupling in the vertical direction within the readout circuitry.

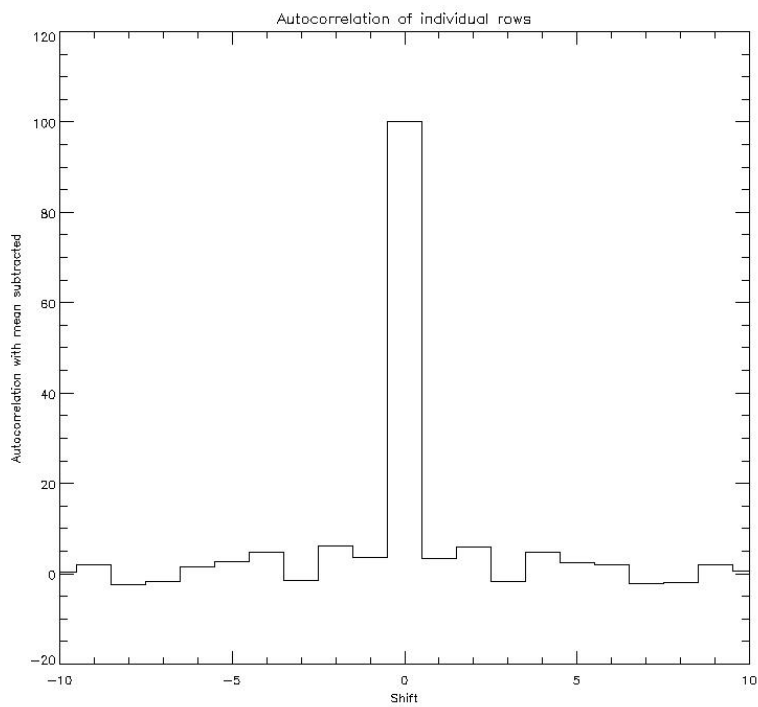


Figure 4.9 1-D autocorrelation of individual mean-subtracted rows.

The 1-D autocorrelation of individual rows is shown in Figure 4.9.

Table 4.6 Column autocorrelation function with a 10-pixel shift in the -y and +y directions.

Shift (pixel)	value									
-10->-1	0.83	2.46	-1.82	-1.21	2.02	3.29	5.20	-1.03	6.53	4.15
0	100									
1->10	3.90	6.47	-1.20	5.17	2.99	2.53	-1.67	-1.43	2.41	1.09

The 1-D autocorrelation result is presented above. After subtracting the DC component, the estimated correlation is **5%** and **4.9%** on the left and right (average of first three in each direction), respectively. The resulting IPC coupling is around **2.5%** and **2.35%**, which gives a much bigger lower limit of IPC magnitude than in the vertical direction. However, the terms away from the center do not go down gradually as it is supposed to be due to interpixel coupling. Therefore, it is difficult to make any conclusion from the correlation analysis.

4.4 Summary

In this chapter we checked whether interpixel coupling exists in the readout IC and thus read noise is affected by interpixel coupling. Due to the offsets and fixed patterns in the data we obtained, it is hard to get real images dominated by read noise. Instead there are always some fixed structures in the bias frames. Therefore, we can't run autocorrelation calculation on the whole image and turn to compute 1-D autocorrelation on single rows and columns. After that, we add up these autocorrelation functions to obtain an estimate in either horizontal or vertical direction. Even in this way, there is still some offset in the rows or columns, so the non-zero mean offset is removed from each row or column

before implementing autocorrelation, which supposes to leave just random noise with zero mean. This is very important as the correlation result including non-zero mean will mislead us. Dark image data are taken from IR HgTeCd and Si-PIN arrays where the same type of multiplexers are employed, i.e. HAWAII-RG multiplexer. Based on the correlation analysis, there is no strong evidence to show that interpixel coupling occurs within the readout multiplexer for both types of detectors in the vertical direction. However, there is evidence that there may be a coupling effect at about 2% level in the horizontal direction, and further experiments are needed to understand its origin. If possible, this approach should be repeated with additional clearer data optimized for this test.

5 Variations of interpixel capacitance

As discussed in previous sections, capacitive coupling is a result of the capacitance between photodiodes or indium bump, as illustrated in Figure 5.1. Thus the coupling magnitude is directly related to the ratio of interpixel capacitance and pixel node capacitance. As it is well known, the capacitance of a p-n junction is a function of several factors, including the bias voltage, dielectric constant, junction cross area, and doping density. Since the voltage across a photodiode decreases in the integration of photons, the capacitance of the p-n junction changes. Interpixel capacitance depends on the gaps between pixels in a per-pixel depleted detector, which are conductive and can shield pixels from each other somewhat, but not completely (Moore et al. 2006). As the gaps vary with the diode bias, this suggests that interpixel capacitance varies, and the resulting coupling magnitude in a per-pixel depleted detector is nonlinear. In addition, the operational detector temperature may have an effect on the coupling. It is known that the resistivity of silicon decreases with temperature rise, and thus the depth of depletion region of a p-n junction should shrink (Janesick 2003). This predicts that interpixel capacitance may be a function of detector temperature. In addition, as discussed in previous sections, capacitive coupling in a per-pixel depleted detector is strongly dependent on the interconnection between the diode array and multiplexer. This means that different types of interconnects in hybrid detectors may cause variations of interpixel capacitance (Brown et al. 2006). In this chapter, we investigate the variations of

interpixel coupling with different factors, including detector temperature, single event intensity, and background level.

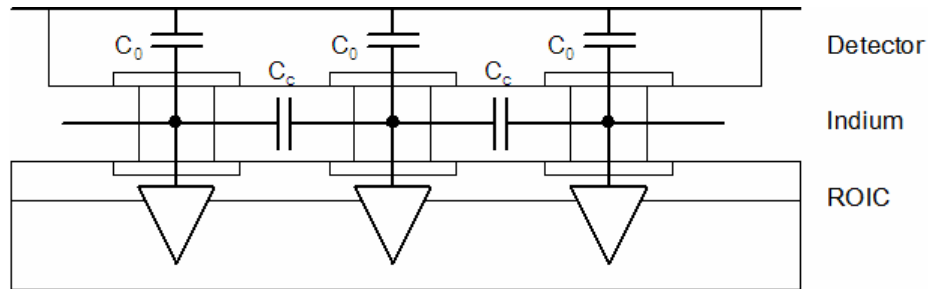


Figure 5.1 Illustration of photodiode capacitance (C_0) and interpixel capacitance (C_c) (Bai et al. 2007).

5.1 Capacitor and capacitance

A capacitor is an electrical/electronic device that can store energy in the electric field between a pair of conductors. The process of storing energy in the capacitor is referred to as charging, and involves electric charges of equal magnitude but opposite polarity building up on each plate. Capacitors are often used in electrical and electronic circuits as energy-storing and charge-collecting devices. They can be also used to differentiate high-frequency and low-frequency signals. Sometimes they can be employed to sample voltage signals. Practically, capacitors more or less have series resistance, internal leakage of charge, series inductance, and other non-ideal properties not found in a theoretically ideal capacitor. There are a wide variety of capacitors used in electronic circuitry, including basic parallel-plate capacitors, mechanical variable capacitors, electrolytic capacitor, and many other capacitors.

The capacitance C of a capacitor is a property of measuring charges stored on each plate for a given voltage, defined as follows.

$$q(t) = Cu(t) \quad (5.1)$$

where $q(t)$ and $u(t)$ are the amount of charges stored on either plate and the potential difference between two plates, respectively. For a basic parallel-plate capacitor, the capacitance is a function of the separation, area, and dielectric constant, as expressed in Eq. 5.2 below.

$$C = \epsilon_r \epsilon_0 \frac{A}{d} \quad (5.2)$$

where ϵ is the permittivity of the material between the parallel plates, A is the front area and d is the separation of two plates. In a p-n junction capacitor, the capacitance varies as the bias changes, in addition to doping densities and the area of the p-n junction. The junction capacitance C_j and depletion depth W_j can be written as follows.

$$C_j = \frac{dQ_j}{dV_j} = \frac{A}{2} \left[\frac{2e\epsilon_r\epsilon_0}{V_o - V} \cdot \frac{N_d N_a}{N_d + N_a} \right]^{1/2} \quad (5.3)$$

$$W_j = \left[\frac{2\epsilon_r\epsilon_0}{e} (V_o - V) \cdot \left(\frac{1}{N_d} + \frac{1}{N_a} \right) \right]^{1/2} \quad (5.4)$$

where Q_j and V_j are the amount of charges stored on either side of a p-n junction and the potential difference across the junction; V_o and V are the built-in potential difference

and the applied bias (negative for reverse bias); N_d and N_a are the donor and acceptor densities of a junction, respectively; and A is the front area of the depletion region. As we can see, the capacitance of a photodiode varies during the integration due to the change of voltage across the junction.

During the integration of photocharges, the voltage across a capacitor changes. This potential difference before and after charge collection is measured as the charge signal. When there is no capacitive coupling between adjacent pixels, the charges collected by a photodiode capacitor will stay there, and thus all the charges are counted as the pixel signal. If interpixel capacitance exists, the signal collected in a center capacitor will redistribute around the center capacitor by electric induction, thus the adjacent capacitors appear to have voltage signal, as illustrated in Figure 5.2. For simplicity, only coupling to the nearest neighbors are considered here. Each adjacent node capacitor and the associated interpixel capacitor are arranged in a serial configuration. The four capacitor series and the center node capacitor are then in parallel. Figure 5.2 illustrates the arrangement of the center node capacitor, its neighbors, and interpixel capacitance. Each p-n junction photodiode and interpixel capacitance are denoted as parallel capacitors.

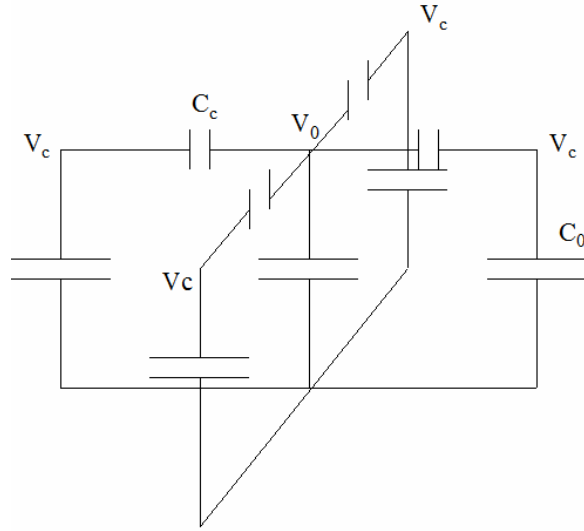


Figure 5.2 Pixel node capacitance C_0 and interpixel capacitance C_c . Only nearest neighbors are considered.

According to the law of capacitors in parallel arrangement, the voltage measured in the center capacitor and the four serial combinations are equal as V_0 . Thus the voltage signal appearing at each of the four neighboring pixels is given below.

$$V_c = \frac{\frac{1}{C_0}}{\frac{1}{C_0} + \frac{1}{C_c}} V_0 \quad (5.5)$$

Applying the capacitance formula of capacitors in series and parallel, the apparent capacitance C_{appr} of the center capacitor including all the four mutual capacitance can be written as follows.

$$C_{appr} = 4 \cdot \frac{1}{\frac{1}{C_c} + \frac{1}{C_0}} + C_0 = \frac{C_0(5C_c + C_0)}{C_c + C_0} \quad (5.6)$$

if $x = C_c / C_0$, then we have

$$C_{appr} = \frac{C_0(5x+1)}{x+1} \quad (5.7)$$

The total charges collected by the center is $Q_{tot} = C_0V_{tot} = C_0(V_0 + 4V_c)$.

The coupling in fraction of total signal α is written below

$$\alpha = \frac{V_c}{V_{tot}} = \frac{V_c}{V_0 + 4V_c} = \frac{x}{1 + 5x} \quad (5.8)$$

For measurement simplicity, the coupling magnitude $\hat{\alpha}$, which is usually expressed as the coupled signal relative to the signal in the center pixel, is given as follows

$$\hat{\alpha} = \frac{V_c}{V_0} = \frac{\frac{1}{C_0}}{\frac{1}{C_0} + \frac{1}{C_c}} = \frac{x}{1 + x} \quad (5.9)$$

As can be seen from both Eq. 5.8 and Eq. 5.9, the coupling magnitude is directly related to the ratio of interpixel capacitance to the detector node (i.e. photodiode) capacitance. This may allow us to estimate interpixel capacitance indirectly from the coupling measurement.

5.2 Identification of cosmic ray events and hot pixels

Throughout this chapter, we report IPC measurements determined from isolated single cosmic ray events and hot pixels. Cosmic rays and hot pixels are highly unwanted events in imaging applications, but these special events can be used to estimate crosstalk between adjacent pixels. As discussed in Sec. 2.6 and 2.7, the different properties

between comic rays and hot pixels make it easy to identify and differentiate them. To measure the coupling between pixels, we focus on the single isolated events. This is because a cluster of events complicates the estimation of pixel crosstalk due to mutual interference within the cluster. The detailed procedure to select good cosmic ray events and hot pixels is presented as follows.

The image data used here are the same as those used for autocorrelation analysis of read noise, as detailed in Chap. 4. For each dark exposure, there are 250 frames sampled up-the-ramp with minimum interval. Candidates of CREs and hot pixels are selected according to the following conditions:

1. 3 sigma criterion: the pixel value of a potential cosmic event or hot pixel is 3σ bigger than the mean of the whole image.
2. If a pixel meets condition 1 in the first five reads, it is recognized as a potential hot pixel; if a pixel meets both condition 1 and 10σ criterion only once among the 250 readouts, it is recognized as a potential cosmic event.
3. No clustering events: there are no other event candidates within a 10-pixel distance from each candidate. Now the remaining hot-pixel candidates are good hot pixels.
4. Threshold: the strength of CRE candidates is between 3000 and 30000 ADU, where the detector operates in the most linear range.
5. Symmetry: the ratio of strongest neighbor to weakest one is smaller than 6. This reduces the asymmetry effect from the input events, leaving the asymmetry coupling mostly from the detector itself. Now the remaining CRE candidates are good cosmic events for IPC measurement.

5.3 IPC dependency on temperature

The interpixel capacitance may be simply modeled as a parallel capacitor, where the separation d is the gap between pixel depletion edges, and ϵ is the permittivity of detector bulk material, e.g. Si and HgCdTe. When the detector temperature varies, both the permittivity and resistivity of bulk materials change. Usually, the permittivity increases with the rise of temperature while the resistivity decreases (Svorcik et al. 2001). The increase of permittivity makes the capacitance larger while the decrease of resistivity makes the electric field depth narrower, and thus increases the gaps between pixels, which will reduce the coupling magnitude. As a result, the two mechanisms may compete when the temperature varies. In the following section, we present the variation of interpixel coupling as a function of different temperatures.

5.3.1 Data analysis and results

According to the criteria of CRE candidates, we first identified isolated CREs from the dark frames captured at a specific detector temperature. Then the coupling magnitude was estimated from each single event in fraction of the event signal, and an average was taken of all the IPC measurements at the specific temperature. Finally, we plotted the average IPC against the temperature. In this way, we hope to see the variation of interpixel coupling with detector temperature.

The test data were captured in 2003 from one of the prototype detectors for the near IR camera of James Webb Space Telescope (JWST), which is a hybrid array with the format of 2048 by 2048. The detector employs HgCdTe and H2RG as the multiplexer

with a cutoff wavelength of $5 \mu\text{m}$ (Figer et al. 2004). All the test images are dark frames taken in the dark test experiments. These data are located in the directory presented in Table 5.1 below. Each fits file stores the frames captured within an exposure, including 250 dark frames with up-the-ramp read mode. There is no time interval from one read to the next one. That is to say, there is a minimum exposure time between continuous samplings. The readout time of each frame is 10.75 sec and the integration time is 2667 sec. The dark frames were taken at different detector temperatures ranging from 27 K to 50 K, each having six exposures. Cosmic events were identified from all the six exposures. Figure 5.3 shows how the coupling magnitude varies with different detector temperatures, where IPC is measured by CREs. At each temperature, more than 300 CREs were identified and used to evaluate interpixel coupling. The coupling magnitude in the graph is the median of those measurements, as listed in Table 5.2. The error at each temperature is evaluated as the standard deviation of IPC divided by square root of the number of measurements, expressed below

$$error = \frac{stdev_{ipc}}{\sqrt{N}} \quad (5.9)$$

A linear fit to these points with regression gives the slope of the relationship as follows.

$$\text{Slope} = -0.0027 \pm 0.00044$$

$$R^2 = 0.83$$

The relative error of the slope is more than 15%, and the value of R squared is not very close to 1. Both suggest that the linear relationship is not strong.

Table 5.1 Directory and test data for the test detector array H2RG HgCdTe.

Detector	H2RG HgCdTe
Directory	Rockwell4\H2RG-015-5.0mu\cold1\dktest.9May03
Data file	dark_*K_250_min_1_*.fits, where 1 st * is from 27, 28, 32, 35, 37, 40, 45, 50, and 2 nd * is from 01 to 06.

Table 5.2 Results of IPC measurement at different temperature by CREs in the HgCdTe array.

Temp (K)	27.7	27.8	28	30	32	35	37	40	45	50
IPC (%)	1.73	1.710	1.711	1.703	1.687	1.706	1.682	1.680	1.676	1.649
Error (%)	0.054	0.072	0.054	0.047	0.036	0.039	0.042s	0.038	0.039	0.037

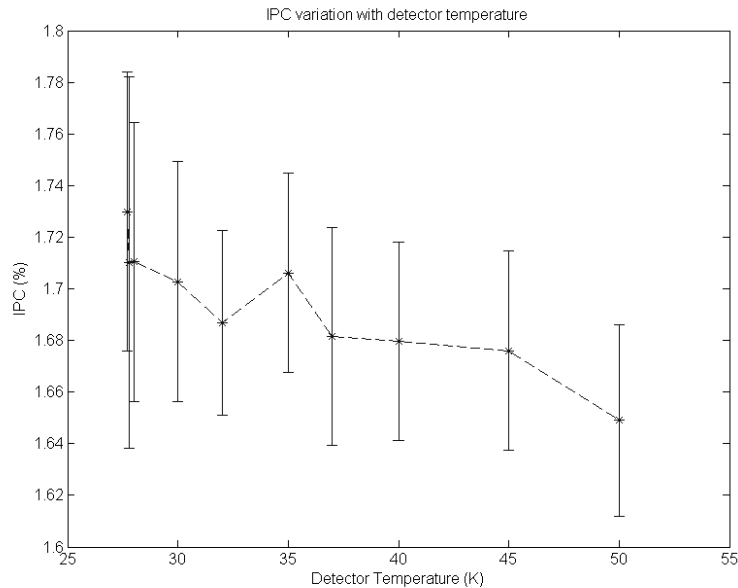


Figure 5.3 IPC variation with the detector temperature. Data taken at temperature ranging from 27.7K to 50 K. IPC is measured through cosmic ray events.

A similar plot is also displayed in Figure 5.4 except that the coupling magnitude was

measured through hot pixels. More than 3000 hot pixels were identified and used. The IPC value of each data point is the median of those IPC measurements at the corresponding temperature, as presented in Table 5.3. The measurement error is evaluated by Eq. 5.9. The linear fit to these points with regression gives the slope and R squared of the linear relationship below. The relative error of the slope is about 7%, and the value of R squared is very close to 1. Both the factors indicate that the linear relationship is strong.

$$\text{Slope} = -0.00625 \pm 0.00044$$

$$R^2 = 0.96$$

Table 5.3 Results of capacitive coupling magnitude at different temperature estimated by hot pixels in the HgCdTe array.

Temp (K)	27.7	27.8	28	30	32	35	37	40	45	50
IPC (%)	1.597	1.596	1.604	1.588	1.583	1.541	1.524	1.518	1.484	1.472
Error (%)	.028	.027	.028	.026	.026	.025	.026	.026	.026	0.026

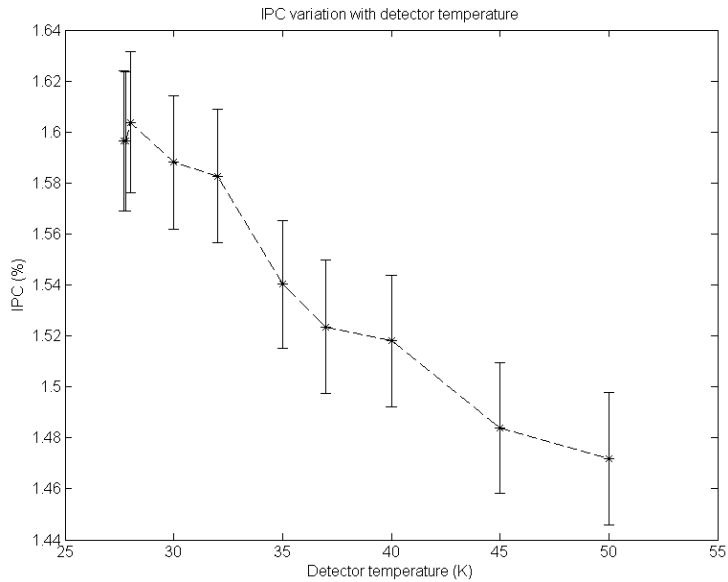


Figure 5.4 IPC variation with detector temperature. Data taken at temperature ranging from 27.7K to 50 K. IPC is measured via hot pixels.

The graph below combines the measurements from CREs and hot pixels at different temperatures, as shown in Figure 5.5. As can be seen, the IPC evaluations from CREs are systematically larger than those from hot pixels, though both show the trend that IPC decreases with the temperature increase. This is reasonable because CRE measurement only gives us an upper limit on IPC due to the contribution of diffusion, whereas hot pixels measure the crosstalk which is close to interpixel coupling. As discussed in Sec. 2.6, cosmic events easily suffer from diffusion crosstalk while hot pixels almost do not. The diffusion adds to the IPC amount measured by CREs. Therefore, the magnitude of IPC estimated from CREs is systematically larger than the IPC estimations from hot pixels. The difference of two measurements will be discussed in more detail in the following section.

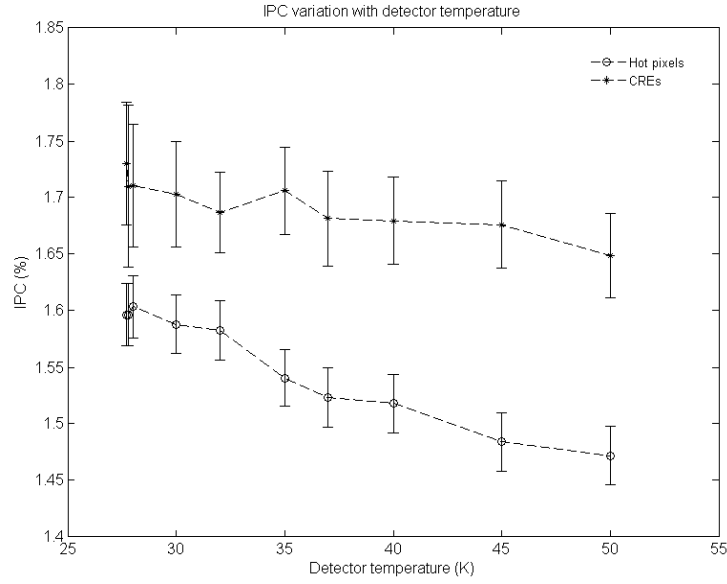


Figure 5.5 IPC variation with the detector temperature, where measurements via CREs and hot pixels are put together.

5.3.2 Discussion

In this section, we study the dependency of IPC magnitude on detector temperature. The coupling is estimated based on cosmic rays and hot pixels. As indicated in Figure 5.3 and Figure 5.4, it is clear that both measurements show the similar trend that the magnitude of interpixel coupling decreases with the increasing temperature. From the discussion in Sec. 5.1, the permittivity and resistivity of the detector material will change with temperature. These two effects compete causing the variation of capacitive coupling. However, as can be seen from Eq. 5.8 and 5.9, the interpixel coupling magnitude in percentage is a function of the ratio of the mutual capacitance C_c to sensor node capacitance C_0 . As both capacitances are proportional to the permittivity, the ratio C_c / C_0 is independent of

the dielectric constant. Therefore, interpixel coupling is expected to vary only due to the gap shrinking between pixel edges when the temperature increases. As the depletion regions of photodiodes shrink, the gaps between depletion regions increase, and thus the interpixel capacitance caused by the fringing fields between pixel implant edges will decrease from the simple capacitance estimation in Eq. 5.2. On the other hand, the capacitance of detector nodes increases with the shrinking of depletion regions. As a result, the capacitance ratio C_c / C_0 will decrease when the temperature increases. From Eq. 5.9, interpixel coupling is a monotonically increasing function of the ratio C_c / C_0 . A smaller ratio will cause a smaller coupling amount. This may explain the IPC variation trend with detector temperature. What's more, due to the fact that thermal diffusion usually increases with increasing temperature, diffusion crosstalk will become worse at higher temperature. This is opposite to the IPC dependency on temperature presented above. However, the IPC estimate is even smaller at higher temperature. This implies that interpixel coupling decreases more than the crosstalk increase due to diffusion with the temperature increase.

In addition, as shown in Figure 5.5, the IPC estimates from hot pixels systematically are smaller than those from cosmic rays, though these are very small. This difference may come from the contribution of diffusion in the cosmic ray events. As mentioned in Sec. 2.6 and 2.7, cosmic rays measure the total crosstalk in the array, and thus only give us an upper limit on capacitive coupling due to charge diffusion, whereas hot pixels can measure the crosstalk which is mainly caused by capacitive coupling. This is because there are few photoelectrons generated under total dark and thermal electrons

are usually created around the boundary of depletion region. The charge carriers generated through thermal agitation seldom wander into neighboring pixels. Thus hot pixels suffer little from lateral diffusion. Therefore, cosmic rays could be expected to show a bigger IPC estimation than hot pixels.

5.4 IPC dependency on single event intensity

5.4.1 Overview

For the two types of hybridized CMOS detector array, per-pixel depleted and full bulk depleted, both are considered to have mutual capacitance between neighboring pixels, but with different field paths, as illustrated in Figure 1.11 and Figure 1.12. In typical per-pixel depleted arrays, e.g. HgCdTe IR array, there is no field between adjacent pixels and IPC is believed to occur in the space between the readout multiplexer and the detector between In-bumps, and to some extent even within the multiplexer. In fully-depleted bulk arrays, i.e. Si-PIN array, the whole bulk is depleted by a high bias, and strong electric fields exist throughout the detector bulk (Finger et al. 2006; Moore 2005). The electric fields built up between pixels may result in the larger observed interpixel coupling than in the per-pixel depleted detector. Since the Si-PIN array also uses the exactly same multiplexer and In-bump connection technique as the HgCdTe array, but shows a much stronger interpixel coupling (Dorn et al. 2006), it may be assumed that the main coupling occurs inside the Si-PIN array. In addition, Bai et al. (2007) found that the coupling in Si-PIN detectors changes with different biases across the PIN diode. A similar

situation may also exist in the HgCdTe IR array. This indicates that the detector bias can affect the magnitude of interpixel coupling.

In addition, interpixel coupling may also vary with the photocharge collection especially in the per-pixel depleted photodiode array, where the gaps between the adjacent pixels are conductive, and should shield neighboring pixels from each other somewhat, but not completely (Moore et al. 2004). As a result, fringing fields may exist between the edges of the pixel depletion regions along the detector surface, as illustrated in Figure 1.11. Since the gap between pixels varies with the detector bias, the mutual capacitance thus changes. This implies that the coupling amount is nonlinear, in the sense that the relative coupling is variable (Moore et al. 2006). As the pixel diode collects photocharges, the depletion region shrinks and the gap between adjacent pixels increases. Thus the interpixel capacitance is expected to decrease. In this section we attempt to verify this idea focusing on single events of different strengths, whereas the background keeps unchanged. The IPC magnitude is estimated through single isolated events, i.e. CREs and hot pixels, assuming the dark current background is negligible relative to cosmic rays and high dark signals.

5.4.2 Data analysis and results

To test the nonlinearity of IPC, we used the same dark frames and procedure as in Sec. 5.3, except that only images captured at 37 K are used. We first select qualified CREs and hot pixels. Secondly, the coupling magnitude is estimated from each individual event. Finally, the relationship of IPC strength vs. CRE intensity or hot pixel strength is plotted.

In this way, we expect to see the variation of IPC with the event strength. The data used are dark frames from the dark test experiments located in the directory given in Table 5.1, where each fits file stores 250 dark frames with up-the-ramp read mode from the H2RG HgCdTe array. There is a minimum exposure time between continuous samplings. The readout time of each frame is 10.75 sec and the total integration time is 2667 sec. The dark frames were taken at temperatures from 27 K to 50 K, each having six exposures. The graphs below show the results for the dark exposures at 37 K. Both CRE and hot pixel methods were used.

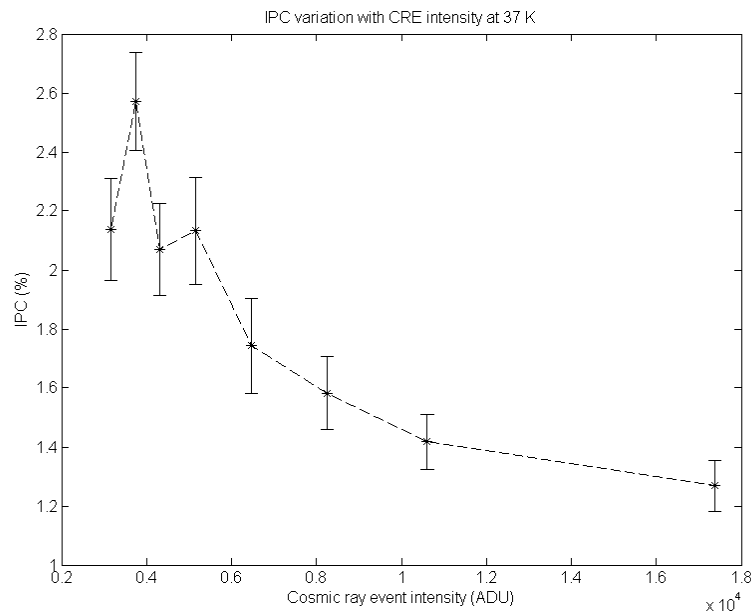


Figure 5.6 IPC vs. CREs intensity, data taken at 37 K. IPC is measured by CREs.

Figure 5.7 shows the intensities of all the cosmic ray events and the measured IPC. There are a total of 320 qualified cosmic ray events and they are separated into eight groups, each of which has 40 events. These grouped data are plotted in Figure 5.7, where each

group is represented by a different symbol. The median CRE intensity and IPC magnitude in each group are marked by green squares. The relation of median CRE strength vs. median IPC magnitude is also presented separately in Figure 5.6. The median data of each group and associated uncertainties are presented in Table 5.4, where intensities of cosmic rays are in units of ADU.

Table 5.4 Results of capacitive coupling magnitude at different event intensities estimated by cosmic rays in the HgCdTe array.

CRE intensity	3157	3757	4303	5147	6474	8251	10610	17381
IPC (%)	2.136	2.571	2.070	2.132	1.743	1.583	1.418	1.268
Error (%)	0.17	0.17	0.16	0.18	0.16	0.13	0.093	0.087

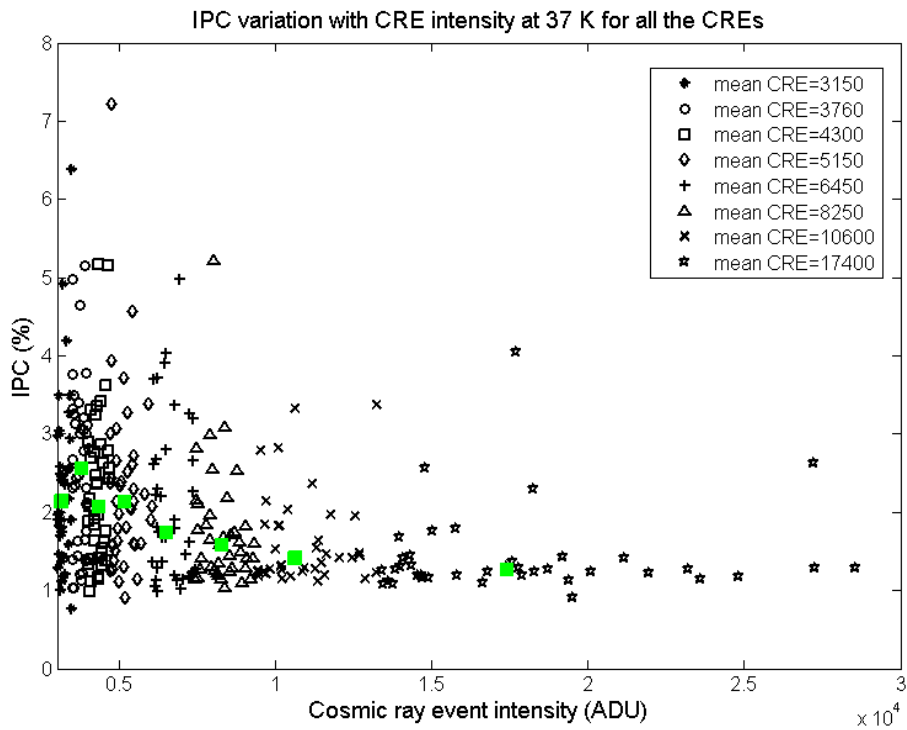


Figure 5.7 IPC vs. CRE intensity, data taken at 37 K. IPC is measured by CREs. Same dataset used as in Figure 5.6.

Similar to the graph in Figure 5.6 above, Figure 5.8 below indicates the IPC variation with hot pixel intensity, where the coupling strength is measured by hot pixels. Each point is the median of the IPC and hot pixel intensities in a group sorted by the event strength. Each group has several hot pixel events used. The median data are listed in Table 5.5, where hot pixel strengths are measured in units of ADU.

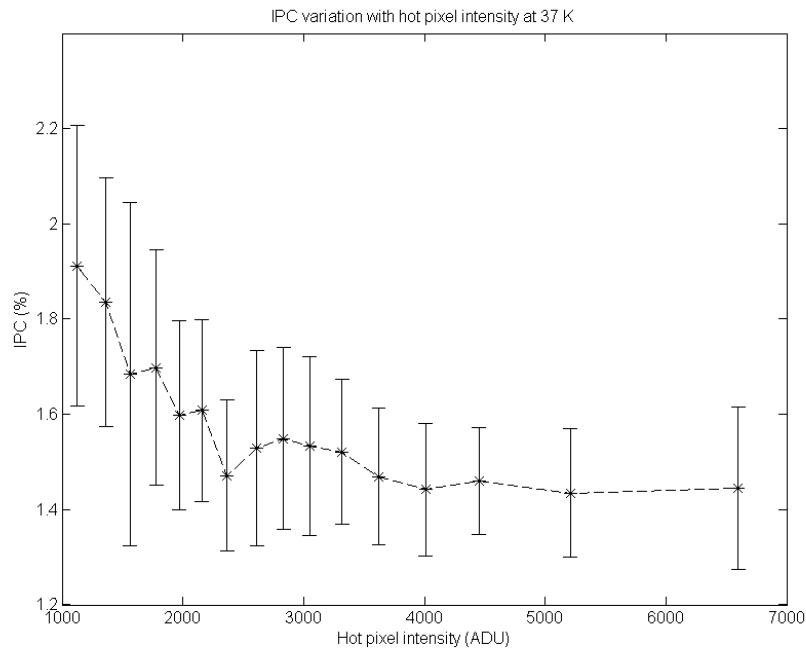


Figure 5.8 IPC vs. hot pixel intensity, data taken at 37 K. IPC is measured by hot pixels. Same dataset used as in Figure 5.6.

Table 5.5 Results of capacitive coupling magnitude at different event intensities estimated by hot pixels in the HgCdTe array.

CRE intensity	1124	1362	1563	1781	1972	2157	2366	2613
IPC (%)	1.912	1.835	1.685	1.699	1.598	1.608	1.471	1.529
Error (%)	0.29	0.26	0.36	0.25	0.20	0.19	0.16	0.21

Table 5.6 Continued.

CRE intensity	2835	3050	3318	3622	4009	4451	5208	6600
IPC (%)	1.549	1.534	1.521	1.470	1.442	1.461	1.435	1.445
Error (%)	0.19	0.19	0.15	0.14	0.14	0.11	0.14	0.17

The combined data from both the cosmic ray and hot pixel measurements are given in

Figure 5.9.

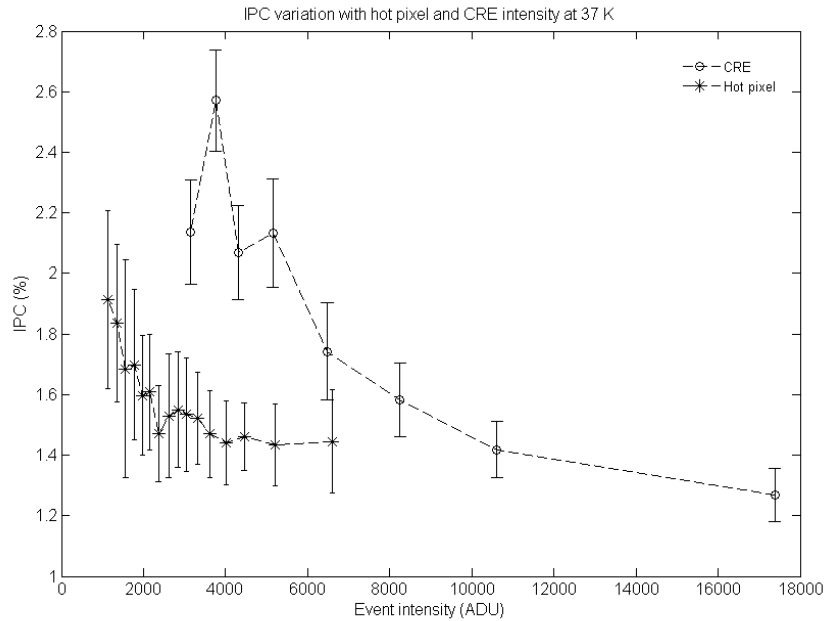


Figure 5.9 IPC vs. event intensity, data taken at 37 K. The graph combines the data from CREs and hot pixels (in Figure 5.6 and Figure 5.8). Same dataset used as in Figure 5.6.

5.4.3 Discussions

In this section we study the variation of IPC magnitude with single event intensity. Isolated events from both cosmic rays and hot pixels are used to estimate the capacitive coupling. For cosmic ray events, all the events are identified from dark experiments at the temperature of 37 K. More than 300 events are found and divided into eight groups according to their intensity. The average of the IPC values and event intensity at each group are evaluated. Thus eight IPC-event intensity pairs are obtained. The result is presented in Figure 5.7. Similar analysis is done for hot pixel events and the result is

indicated in Figure 5.8. As can be seen, both graphs show a similar trend that the magnitude of interpixel coupling decreases as the events become stronger. This is expected from the discussion in Sec. 5.4.1.

As we know, the depletion region of a p-n junction diode shrinks and the voltage across the junction decreases as the diode collects photoelectrons. Eq. 5.4 presents the relationship between the voltage across a junction capacitor and the depletion depth. According to Eq. 5.3 and 5.4, the capacitance and depletion width of the junction for the HgCdTe detector before the photon integration are estimated below.

$$C_j = 8.84 \text{ fF}, \text{ and } W_j = 3.38 \mu\text{m}$$

where a junction face area A of $15 \times 15 \mu\text{m}^2$, the static dielectric constant ϵ_r of 15, donor and acceptor doping densities of 10^{14} cm^{-3} and $5 \times 10^{15} \text{ cm}^{-3}$, a built-in potential V_0 of 0.412 volt, and a reverse bias of 0.263 volt were used. After the signal level reaches 10000 ADU, the voltage across the junction will drop about 0.11 volt assuming the junction potential decreases to about zero at maximum signal level (65535 ADU), i.e. 0.675 volt. The junction capacitance and depletion depth become

$$C_j = 9.68 \text{ fF}, \text{ and } W_j = 3.08 \mu\text{m}$$

The junction capacitance increases by 10%, and the depletion region shrinks $0.3 \mu\text{m}$ or 9%. The gap between the edges of pixel implants increases $0.6 \mu\text{m}$ and thus the mutual capacitance due to fringing fields between pixel edges decreases according to Eq. 5.2. However, this mutual capacitance cannot be calculated as we do not have a good estimate of the face area.

Another capacitive coupling occurs between the parallel faces of the indium bumps. The capacitance should keep constant during the photon integration as nothing is changed. Therefore, the total mutual capacitance between neighboring pixels, the sum of the coupling from implant edges and between indium bumps, goes down. Both the rise of the junction capacitance and the decrease of mutual capacitance will cause the ratio of interpixel capacitance to the photodiode capacitance C_c / C_0 to get smaller with charge collection. According to Eq. 5.8 and 5.9, it is clear that the percentage coupling amount is a function of the ratio, i.e. the smaller the ratio, the weaker the coupling. Therefore, the IPC amount is expected to decrease with charge collection. The experiment results are consistent with the theoretical expectation. Figure 5.10 below illustrates the changes of depletion depth of junction diodes and the gaps between the edges of pixel implants.

In addition, both graphs show that the capacitive coupling becomes weaker as the diode collects photo charges. At the same time, the change rate keeps changing, in the sense that IPC decreases much faster for weak events. Finally, the coupling almost does not change even as the events become stronger. This means that the variation of IPC magnitude with event intensity is nonlinear. That is, the capacitive coupling becomes weaker as the diode collects more charge, and the change rate gets smaller. After collecting a certain amount of charge, the coupling does not vary.

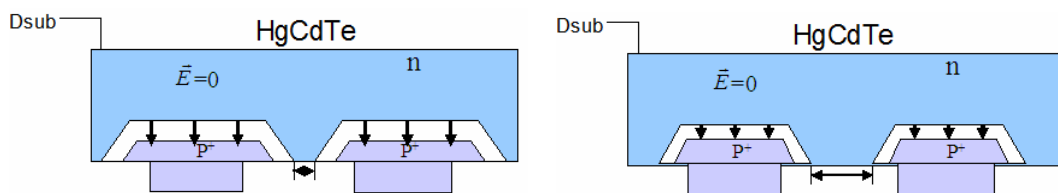


Figure 5.10 Depletion region for HgCdTe arrays. Left: before charge collection, right: after charge collection.

5.5 IPC dependency on background

As we presented in Sec. 5.4, interpixel coupling varies with the event intensity, either cosmic events or hot pixels. The stronger the event, the smaller the coupling, assuming that the background change is negligible. This partly verifies that IPC in per-pixel depleted devices is nonlinear. As the pixel node collects photo carriers, not only the capacitance of junction diode increases, but the depletion region shrinks and thus the gap between adjacent pixels increases. Both effects will cause the ratio of mutual capacitance to junction diode capacitance C_c/C_0 to become smaller. Therefore, the capacitive coupling amount decreases according to Eq. 8 and 9. A similar idea is applied to the situation that the center event intensity is constant, but the background level varies, which also can change the gaps between adjacent pixels. The variation of gaps is expected to change the interpixel capacitance component contributed by the fringing field between the edges of pixel implants, while the junction diode capacitance does not change. Therefore, the coupling amount may change in a similar fashion.

5.5.1 Data analysis and results

The test data used are from the photon transfer experiments and located in the directories given in Table 5.7 below. The detector array is still H2RG HgCdTe IR. The flat fields of different illuminations correspond to different background levels. One problem with the data is that the exposure times are so short that there are not many cosmic events during an exposure. For each dataset, the light source and filter did not change during the experiment. Only the exposure time was changed. There are a total of nine exposures,

including dark frames with minimum integration time. At each exposure, 10 correlated double sampling (CDS) frames are available. From these flat field frames, we identify cosmic events by the criteria similar to those described in section 5.3 as follows:

1. 3 sigma criteria: the pixel value of a potential CRE is 3σ bigger than the mean of the image. Many potential events are selected.
2. No clustering CREs: no other pixels satisfy condition 1 within the distance of 10 pixels from any potential CRE pixel.
3. Threshold: the CRE strength is between 3000 and 30000 ADU.
4. Symmetry: the ratio of highest neighbor pixel value to lowest one is smaller than 6.

Table 5.7 Directories and test data for the test detector array H2RG HgCdTe.

Detector	H2RG HgCdTe
Directory	Rockwell4\H2RG-015-5.0mu\cold1\PhotonXfer_test.8May03\ Rockwell4\H2RG-015-5.0mu\cold1\PhotonXfer_test.9May03\H_data\ Rockwell4\H2RG-015-5.0mu\cold1\PhotonXfer_test.9May03\K_data\ PhotonXfer_BL1_H+PK50-2_37.000K_*.*.fit, where 1 st * is from 0 to 7, and 2 nd * is from 0 to 9.
Data file	

The flat-field levels from the 3 datasets are different from each other. We evaluate the IPC value for each qualified CRE, which corresponds to a background and CRE magnitude. At each background or flat field level, we select a certain number of CREs, each of which had a different magnitude. We plot the IPC vs. CRE strength for several different background levels as shown in Figure 5.11 below. More than 20 flat field levels available are used in the plot, each of which is marked with a different color. As can be seen, there is no obvious trend.

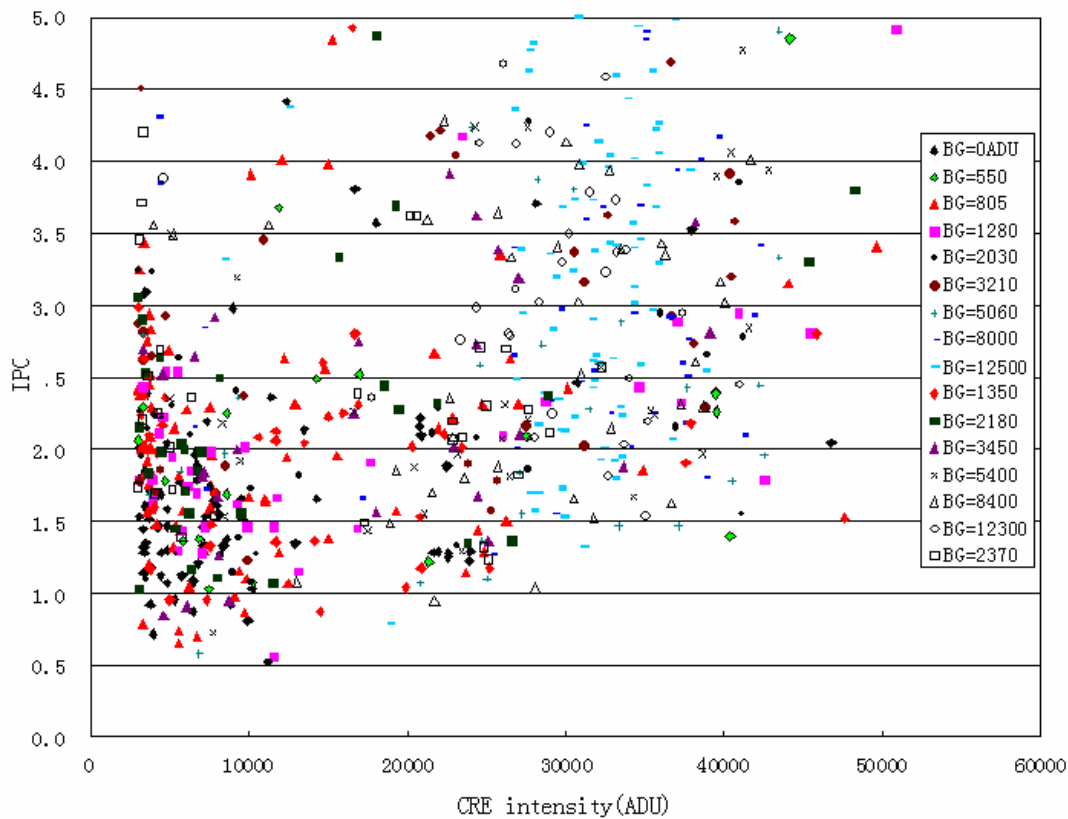


Figure 5.11 IPC (%) vs. CRE intensity (ADU) for different background labeled with different colors.

As we cannot see any obvious trend from the graph above, the CRE measurements of the same background were averaged. The data are given in Table 5.8-Table 5.10, where the CRE value is the median of all the CRE estimations at the individual background level. Then we obtained 25 average CRE-background pair values. The plot of mean CRE vs. background is shown in Figure 5.12. It is clear that the measured IPC increased as the background became higher. Since the CRE magnitude varied significantly even under any background, the relationship of mean CRE vs. background may not reflect how CRE change with background. As we applied 3σ as the initial criteria to identify CRE, the

intensities of CREs identified would be statistically high for a strong background. This is because the sigma is proportional to the square root of the background level based on Poisson noise characteristic. So the mean intensity of the CREs increases with the rising background. In this regard, the variation of IPC is not only related to the background change, but the CRE intensities. Therefore, the mean IPC vs. background plot did not address both the two factors at the same time. To deal with the situation, we plotted mean IPC vs. the difference between mean CRE intensity and background level as shown in Figure 5.13, where each mean CRE is the median of CRE intensities under that specific background.

Table 5.8 Results of capacitive coupling magnitude at different flat field levels estimated by cosmic rays in the HgCdTe array, data from BL1_J+PK50-2 photon transfer experiments.

Exposure time(s)	10.75	15	23.92	37.98	60.17	95.18	150.41	237.54	375
Flat field	0	505	805	1282	2030	3209	5060	7972	12533
IPC (%)	1.612	1.835	1.907	1.968	2.121	2.899	2.391	3.386	3.508
Error (%)	0.176	0.238	0.205	0.242	0.259	0.179	0.487	0.563	0.226
CRE intensity	7735	11541	9717	9888	10104	23047	27382	31128	32186
CRE-background	7735	11036	8912	8606	8074	19838	22322	23156	19653
Background/CRE	0.0	0.04	0.08	0.13	0.20	0.14	0.18	0.26	0.39

Table 5.9 Continued. Results based on data from BL1_H+PK50-2 photon transfer experiments.

Exposure time(s)	10.75	10.8	18	29	46	72	113	175
Flat field	0	809	1349	2179	3452	5408	8396	12955
IPC (%)	1.625	2.088	2.075	2.182	2.497	2.404	3.369	3.383
Error (%)	0.092	0.894	0.337	0.449	0.753	0.286	0.296	1.347
CRE intensity	6482	9058	14214	8214	16917	24314	30919	30232
CRE-background	6482	8249	12865	6035	13465	18906	22523	17277
Background/CRE	0.0	0.09	0.09	0.27	0.20	0.22	0.27	0.43

Table 5.10 Continued. Results based on data from K+PK50-2_BL2 photon transfer experiments.

Exposure time(s)	10.75	10.8	18	29	46	72	113	175
Flat field	0	878	1469	2370	3754	5868	9100	14021
IPC (%)	1.320	1.904	2.208	2.326	2.310	1.984	2.47	3.176
Error (%)	0.151	0.117	0.318	0.163	0.332	0.261	0.152	1.209
CRE intensity	6395	5682	14512	17296	18369	18855	26157	29910
CRE-background	6395	4804	13043	14926	14615	12987	17057	15889
Background/CRE	0.00	0.15	0.10	0.14	0.20	0.31	0.35	0.47

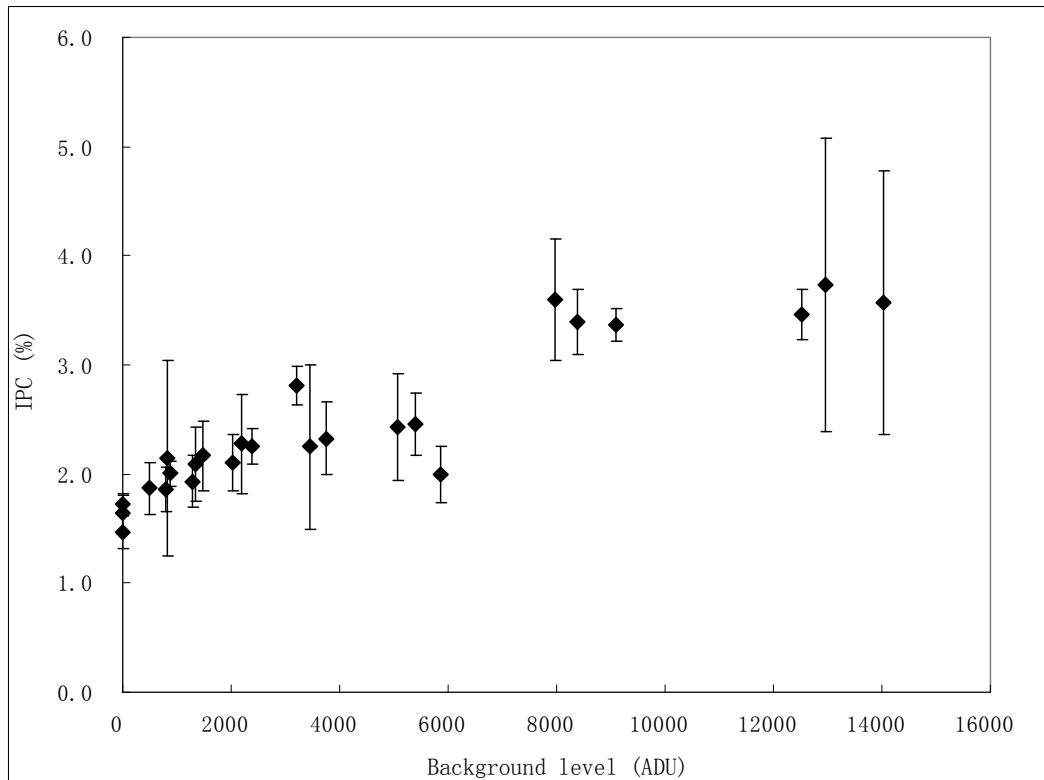


Figure 5.12 Mean IPC vs. background for different background levels. The IPC measurements were averaged from the same background. Background was determined from the flat field level. Same data as in Figure 5.11.

A linear fit to the points in Figure 5.12 with regression gives the slope and R squared of the relationship below.

$$\text{Slope} = 0.000128 \pm 1.52\text{E-}05$$

$$R^2 = 0.75$$

The uncertainty of the slope is about 12%, and the small R squared value indicates that this relationship is not strong.

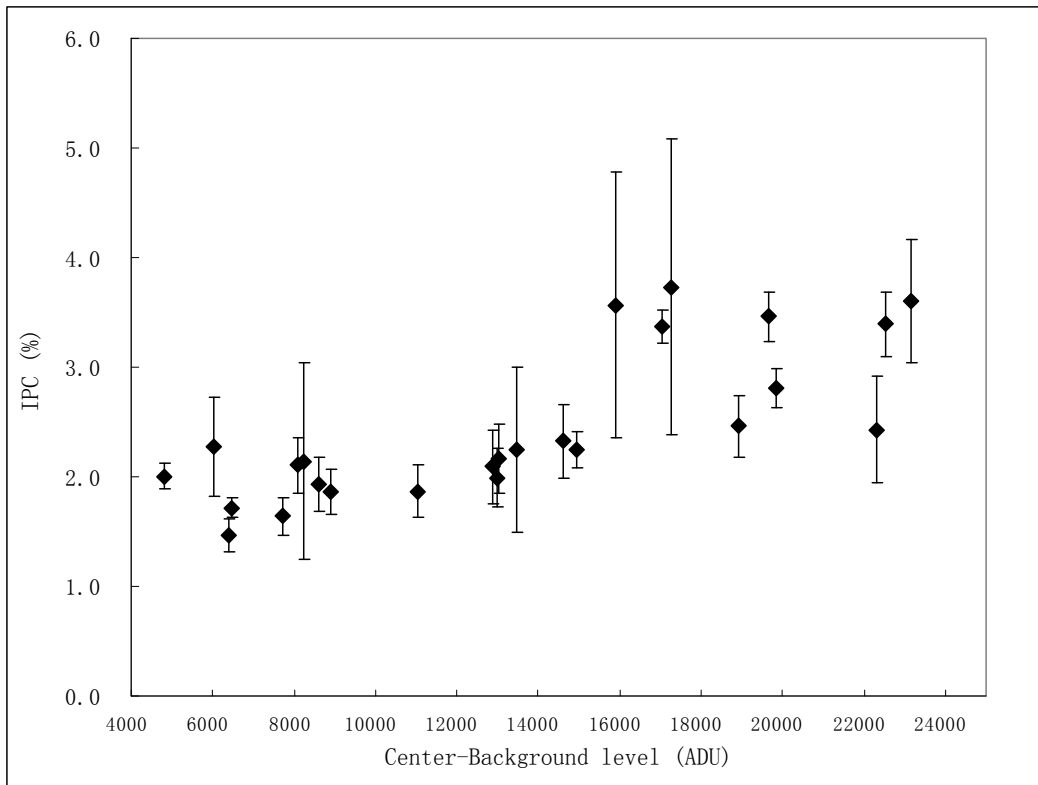


Figure 5.13 Mean IPC vs. difference between mean CRE and background for different background levels. The IPC measurements and CRE intensities were averaged for the same background. Same data as in Figure 5.11.

A linear fit to those points in Figure 5.13 with regression yields the slope and R squared

of the relationship as shown below.

$$\text{Slope} = (8.83 \pm 1.42) \text{ E-05}$$

$$R^2 = 0.63$$

The facts of the large uncertainty of the slope (~16%) and small R squared value indicate that this relationship is weak.

In addition, the IPC magnitude was plotted against the ratio of background level to the CRE intensity. Similarly, IPC measurements and CRE intensities were averaged at each flat field level. In Figure 5.14 we can see how the mean IPC varied with the ratio of background level to the CRE intensity. A linear fit to these points with regression yields the slope and R squared of the relationship as follows.

$$\text{Slope} = 3.82 \pm 0.62$$

$$R^2 = 0.63$$

Similar to the fit to the points in Figure 5.13, the uncertainty of the slope is large and the R squared value is not close to 1. Both the factors indicate that this linear relationship is weak.

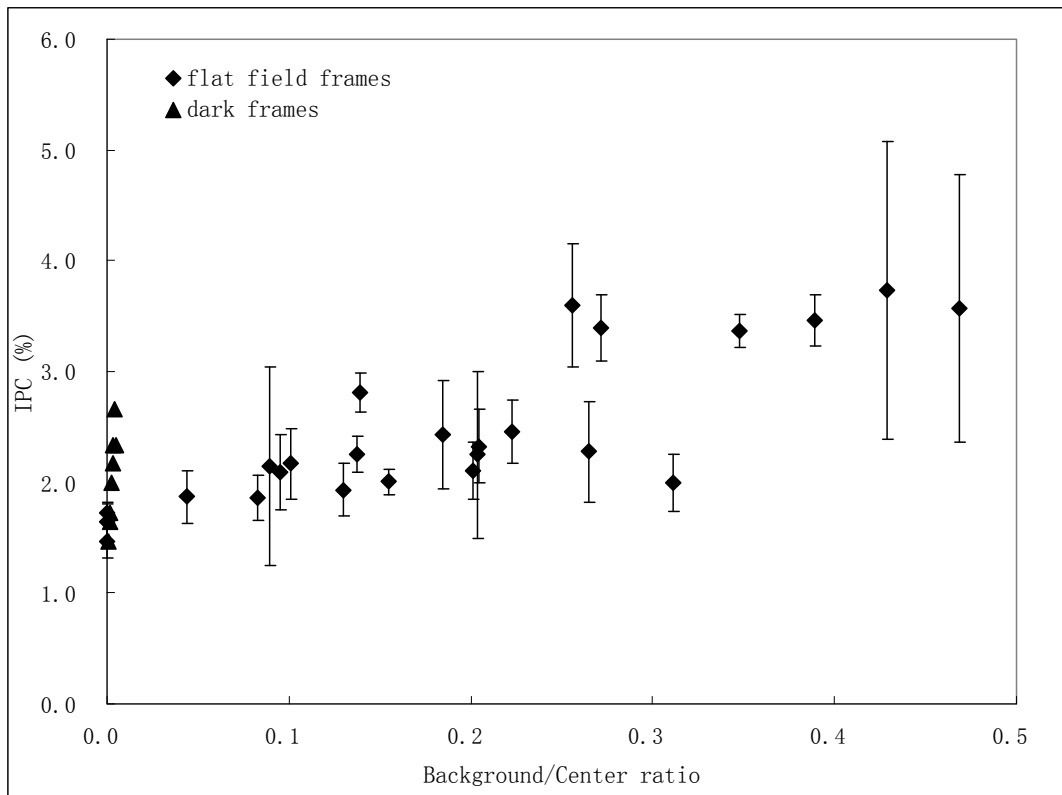


Figure 5.14 Mean IPC vs. ratio of mean CRE to background for different background levels. Same data as in Figure 5.11.

5.5.2 Discussion

In this section, we study the variation of interpixel coupling with the background level. Cosmic ray events are still used to estimate IPC magnitude from different flat-field Fowler-1 frames, whereas the background is determined by the flat-field level. At each flat-field level, a certain number of cosmic rays are selected to estimate IPC, and then the median IPC value represents the coupling strength at that background level. The IPC values are plotted against different flat fields, as shown in the graphs above. As can be seen, the coupling gets stronger with the increase of background. This is opposite to what

we predict based on the theory discussed in previous sections that the capacitive coupling will become weaker when the detector nodes, either the center pixel or the neighbors, collect signal charge. This is because the gap between adjacent pixel edges widens. However, the relationships are not robust due to the large error of the slope and small R squared value of the linear fit with regression. In addition, the uncertainties are big for each data point. Also, there are large uncertainties upon identifying cosmic ray events in the CDS mode in comparison with the UTP mode. Lastly, shot noise adds errors to IPC measurements due to light illumination. Therefore, further IPC measurements are needed to verify the result based on specialized experiments.

5.6 Summary

In this chapter we investigate the variations of capacitive coupling with the detector temperature, single event intensity of target pixels, and the levels of neighboring pixels surround target pixels. The IPC values are estimated through cosmic rays and hot pixels. It is clear that the coupling becomes weaker as the temperature gets higher, which is interpreted based on a simple network of pixel node capacitors and interpixel capacitor. In addition, the coupling is found to decrease with increasing isolated event intensities, as is predicted based on the relationship between interpixel coupling, node capacitance, and interpixel capacitance. Finally, based on the data from photon transfer experiments, the interpixel coupling seems to get stronger at higher background, though the trend is weak. This cannot be explained based on the simple model of interpixel capacitance described in this chapter. Further particular experiments may need to verify this result due to large

measurement uncertainties and insufficient number of events for statistics.

6 Summary and conclusions

6.1 Summary

The potential impact of interpixel capacitive coupling on the astronomical photometry was simulated based on the filter theory. Interpixel coupling was simply modeled as another point spread profile in addition to the diffusion and pixel collection profile. It is obvious that IPC can affect the photometric measurement. Both inverse and Wiener filters were applied to restore the images and thus correct the coupling influence. It appears that inverse filter performed better than Wiener filter in terms of both the signal loss and SNR degradation. Applying the pseudo-inverse filter to different signal levels, it is found that the signal loss can be restored to reasonable accuracy, provided that we have good knowledge of interpixel coupling.

It also was checked whether interpixel coupling exists in the readout IC and thus read noise may be affected by interpixel coupling. This issue was addressed based on the correlation analysis of the read noise component. Due to the offset and fixed pattern in the data image we had analyzed, it was very difficult to get practical images dominated by read noise, instead there were always some fixed patterns. Therefore, we couldn't run autocorrelation calculation on the whole image and turned to compute 1-D autocorrelation on single rows and columns. The non-zero mean levels of individual rows and column were deducted before implementing 1-D autocorrelation. Autocorrelation functions of many rows and columns were added up to get enough statistics. Based on the dark frame data from both IR HgTeCd and Si-PIN arrays where the same type of

multiplexers are employed, i.e. HAWAII-RG multiplexer, the 1-D correlation of read noise was analyzed. There is no strong evidence to show that interpixel coupling occurs within the readout multiplexer for both types of detectors in the vertical direction. However, there is evidence that there may be a coupling effect at about 2% level in the horizontal direction, and further experiments are needed to understand its origin. If possible, this approach should be repeated with additional clearer data optimized for the experiment.

New methods to measure the IPC values were proposed and tested based on the cosmic ray events and hot pixels, where the dark frame data sampled up-the-ramp were used. With these two methods, the variations of capacitive coupling strength were studied for different temperatures. It can be seen that the IPC magnitude decreases with increasing detector temperature, as can be predicted from the IPC model. The IPC dependencies on the center pixel intensity and background were also checked. It appears that the coupling becomes weaker when the target pixel event gets stronger, while the trend reverses with the change of background level. The former is predictable from the theory that the gaps between pixels increase during the charge collection. However, the variation of IPC with different backgrounds contradicts this theory. Further experiment and analysis need to verify and explain this variation.

6.2 Conclusions

As an additional detector point spread profile, interpixel coupling will blur images and thus may introduce photometric errors. Simulations show that interpixel capacitance can

cause extra errors on the photometric measurement as well as impact image quality. To restore the degraded images and correct photometric measurements, inverse filter performed better than the widely-used Wiener filter at either high or low signal levels. Given the knowledge of interpixel coupling, both the photometry and signal-to-noise ratio can be recovered to reasonable accuracy with a pseudo-inverse filter as long as interpixel coupling is well known and stable.

It is widely accepted that interpixel coupling occurs after charge collection. Poisson noise is affected by interpixel capacitance, and thus the polluted photon noise is spatially correlated. Using similar correlation analysis on readnoise-dominated images, it is found that read noise is not spatially correlated with neighbors. This suggests that mutual capacitance does not occur within the readout IC, and thus does not affect readout noise.

Test of methods based on cosmic rays and hot pixels shows that both are effective ways to estimate IPC. Using hot pixel event is a more accurate measure while cosmic rays only give an upper limit on IPC due to the contribution of diffusion. As discussed before, the interpixel coupling magnitude depends on the ratio of interpixel capacitance to the center node capacitance. When either capacitance changes, the coupling measured in percentage will vary. Analysis based on cosmic rays and hot pixels indicates that capacitive coupling becomes weaker at higher temperature. In addition, as the center event gets stronger, the coupling magnitude decreases, provided that the background level does not change. In a similar manner to the variation of center event intensities, the level of adjacent pixels varies while the center pixel does not. The measurement coupling amount becomes bigger as the background get stronger. This is opposite to what the

pixel-gap theory predicts.

6.3 Future research

As discussed in section 5.5, the dependency of interpixel coupling on background level still needs further verification with specialized experiments. Particular test images may be captured under the Fe55-X-ray source at different illumination levels. Fe55 source emits x-ray events with well-calibrated counts, and the illumination background can be easily controlled and adjusted with a standard light source. This would give us enough single isolated events of fixed intensity at different background levels. In addition, better read noise test need to be done to verify that interpixel coupling doesn't happen in the readout circuit.

In this thesis, a simple relationship between interpixel coupling magnitude, and interpixel capacitance and pixel node capacitance was derived. However, there is no physical model to predict the capacitive coupling from the detector basics. For instance, given the key parameters about the detector structure, interpixel capacitance may be estimated and compare with the experimental results. This will help us to understand the capacitive coupling in depth.

In addition, as stated above, the capacitive coupling is much bigger in hybrid Si-PIN arrays than per-pixel depleted arrays. This is a disadvantage of fully-depleted bulk arrays and will damage the imaging performance, such good red QE and low diffusion crosstalk. Therefore, further design work is needed to reduce the capacitive coupling and optimize detector overall performance.

Appendix A: Convolution and deconvolution

A.1 Linear shift-invariant system

Linear shift-invariant system (LTI) is a system that is simultaneously linear and shift invariant. The combination of these two constraints ensures that the system has a particular mathematical description that is applicable to many systems, such as circuits, imaging systems, and control systems.

From the definition of linearity, we can calculate the output amplitude by scaling the output from a normalized input function that is identical for different inputs. The property of shift invariance makes the output function be translated to any location in the domain. The output of a system satisfying these two constraints can be determined by translating, scaling, and summing the output from a special input function. As a result, a LSI system allows the calculation of the output function to be simplified by decomposing the input function into the superposition of the outputs from a set of basis functions. The most commonly used decomposition of the input function is sifting as follows.

$$f[x]\delta[x - x_0] = f[x_0]\delta[x - x_0] \quad (\text{A.1})$$

The output from each of the scaled and translated Dirac delta functions is a scaled and translated replica of the output from a unit-area Dirac delta function located at the origin.

$$\Theta\{\delta[x - 0]\} = \Theta\{\delta[x]\} \equiv h[x] \quad (\text{A.2})$$

where Θ is the action operator of the LSI system; $h[x]$ is the notation of the 1-D impulse response, the response of the system to an impulsive input. The properties of shift-invariant and linear allow the following two operations.

$$\Theta\{\delta[x - x_0]\} = h[x - x_0] \quad (\text{A.3})$$

$$\Theta\{\alpha_0\delta[x - x_0] + \alpha_1\delta[x - x_1]\} = \alpha_0h[x - x_0] + \alpha_1h[x - x_1] \quad (\text{A.4})$$

As shown in Eq. A.4, the response of a LSI system from a pair of shifted and scaled input impulses is the superposition of a corresponding pair shifted and scaled impulse response. The response of a system Θ to an input function $f[x]$ is obtained by applying the operator.

$$g[x] = \Theta\{f[x]\} = \Theta\left\{\int_{-\infty}^{\infty} f[\alpha]\delta[x - \alpha]d\alpha\right\} \quad (\text{A.5})$$

where the input function $f[x]$ is decomposed into a set of weighted Dirac delta functions via the sifting property of Dirac delta function. Applying the linear property, Eq. A.5 can be rewritten as follows.

$$g[x] = \int_{-\infty}^{\infty} \Theta\{f[\alpha]\delta[x - \alpha]d\alpha\} = \int_{-\infty}^{\infty} f[\alpha]\Theta\{\delta[x - \alpha]d\alpha\} \quad (\text{A.6})$$

Applying Eq. A.3, we can obtain the most important expression for the output function $g[x]$ in the following equation.

$$g[x] = \int_{-\infty}^{\infty} f[\alpha]h[x - \alpha]d\alpha \equiv f[x] * h[x] \quad (\text{A.7})$$

Eq. A.7 specifies the output of a LSI system as a specific integral – **convolution** integral of the input $f[x]$ and the impulse response $h[x]$. The asterisk sign denotes the convolution operation. As can be seen, the output of the system from the impulsive input $f[x] = \delta[x]$ is an important descriptor of a LSI system. It is assigned different names by different disciplines. In optics and imaging science, the impulse response $h[x]$ is more often referred to as point spread function (psf), one of the most important parameters of an imaging system.

A.2 Convolution

As stated in Sec. A1, the output of a LSI system is the convolution of the input function and the impulse response. This process of convolution is also called linear filtering of an input signal by the system. The mathematical operation of convolution of two 2-D functions $f[x, y]$ and $h[x, y]$ is expressed in the equation below.

$$g[x, y] = (f * h)[x, y] = \int_{-\infty}^{+\infty} f[\alpha, \beta] h[x - \alpha, y - \beta] d\alpha d\beta \quad (\text{A.8})$$

As can be seen, the output of a convolution computed at a single coordinate, e.g. $g[x_0, y_0]$, is obtained by summing the products obtained by point-by-point multiplication of the input $f[\alpha, \beta]$ and a copy of $h[\alpha, \beta]$ that has been flipped and then translated by the distance x_0 and y_0 in the x and y directions, respectively. The central coordinates of the flipped and translated copy now are placed at $[\alpha, \beta] = [x_0, y_0]$. The inverse of this mathematical relationship is also true: any system that can be described by a convolution

integral must be both linear and shift invariant. The individual steps to compute convolution integral are presented below:

1. Change the domain of $f[x, y]$ and $h[x, y]$ to generate $f[\alpha, \beta]$ and $h[\alpha, \beta]$.
2. Flip the impulse response about the origin to obtain $h[-\alpha, -\beta]$.
3. Translate $h[-\alpha, -\beta]$ by the distance x_0 and y_0 in x and y axis to obtain $h[x_0 - \alpha, y_0 - \beta]$.
4. Multiply the two functions $h[x_0 - \alpha, y_0 - \beta]$ by $f[\alpha, \beta]$ to get the product function.
5. Integrate the product function over the (α, β) domain and the area is obtained.
6. Assign this area to the output amplitude $g[x, y]$ at coordinate $[x_0, y_0]$.
7. Repeat steps 3 for the output at all other coordinates in domain.

The discrete convolution of $f[i, j]$ and $h[i, j]$ is given by

$$g[i, j] = (f * h)[i, j] = \sum_{m, n=-\infty}^{m, n=+\infty} f[m, n]h[i - m, j - n] \quad (\text{A.9})$$

A.3 Filtering theorem

The most important property of the Fourier transform in imaging applications is the relationship between the Fourier spectrum of a convolution and the spectra of the constituent functions. It states that the spectrum of a convolution is the product of the spectra of the constituent function. This is referred to as filtering theorem. The theorem is widely used in imaging systems, especially optical systems that can be modeled as linear

and shift invariant. It provides a very powerful approach to analyze imaging system, e.g. deblurring. Mathematics of the theorem is described below.

$$FT\{g[x, y]\} = FT\{(f * h)[x, y]\} = FT\{f[x, y]\} \cdot FT\{h[x, y]\} \quad (\text{A.10})$$

where FT denotes the Fourier transform from spatial domain to spatial frequency domain.

Eq. A.10 can be simplified as

$$G[\xi, \eta] = F[\xi, \eta] \cdot H[\xi, \eta] \quad (\text{A.11})$$

where capital letter denote the Fourier transform of the corresponding functions. In optical imaging applications, the Fourier spectrum $H[\xi, \eta]$ of the point spread function $h[x, y]$ generally is referred to as the system transfer function. It specifies the effect upon the constituent sinusoids of the input functions as they pass are transferred through the system to the output. As can seen, the theorem provides another way to compute the output of a LSI system, i.e. convolution, as presented below.

$$g[x, y] = FT^{-1}\{G[\xi, \eta]\} = FT^{-1}\{F[\xi, \eta] \cdot H[\xi, \eta]\} \quad (\text{A.12})$$

where FT^{-1} denotes the inverse Fourier transform.

A.4 Deconvolution: inverse and Wiener filters

As discussed above, the output of an optical imaging system is the convolution of the input and the point spread function. That is to say, the image captured from the imaging

system is linearly filtered or smoothed by the psf, which is usually a low-pass filter. As a result, the observed image is blurred somewhat. To restore the smoothed image to its original version, linear filters are often applied to deconvolve the blurred image. Two widely-used deconvolution kernels, inverse filter and Wiener filter, are described in the following.

Inverse filter

As we can see, a linear system can alter the amplitude and/or phase of some or all of the sinusoidal components of the input function. Once the impulse response of the system is known, we can recover the input function through pseudoinverse filter. Rewriting Eq. A.11 we obtain

$$F[\xi, \eta] = \frac{G[\xi, \eta]}{H[\xi, \eta]} \quad (\text{A.13})$$

$$\hat{f}[x, y] = FT^{-1}\{F[\xi, \eta]\} = FT^{-1}\left\{\frac{G[\xi, \eta]}{H[\xi, \eta]}\right\} \quad (\text{A.14})$$

So

$$\hat{f}[x, y] = g[x, y] * FT^{-1}\left\{\frac{1}{H[\xi, \eta]}\right\} \quad (\text{A.15})$$

$$w[x, y] = FT^{-1} \left\{ \frac{1}{H[\xi, \eta]} \right\}$$

$$W[\xi, \eta] = \frac{1}{H[\xi, \eta]} \quad (\text{A.16})$$

where $w[x, y]$ and $W[\xi, \eta]$ are the ideal impulse response and transfer function of the inverse filter, respectively. In the real cases that $H[\xi, \eta] = 0$ at some frequencies, a pseudoinverse filter as shown in Eq. A.17 is obtained instead of Eq. A.16.

$$\hat{W}[\xi, \eta] = \frac{1}{H[\xi, \eta]} \quad \text{if } H[\xi, \eta] \neq 0$$

$$= 0 \quad \text{if } H[\xi, \eta] = 0 \quad (\text{A.17})$$

Wiener filter

The inverse filter stated above estimates the input from complete a priori knowledge of the system, assuming that there is no additive noise in the output. When the output signal is noisy, the well-known Wiener filter supposes to work better. The mathematical descriptions of an imaging system with additive random noise in spatial and frequency domain are as follows.

$$g[x, y] = f[x, y] * h[x, y] + n[x, y]$$

$$G[\xi, \eta] = F[\xi, \eta] \cdot H[\xi, \eta] + N[\xi, \eta] \quad (\text{A.18})$$

The task is to derive the linear filter $w[x, y]$ which is applied to the noisy output signal $g[x, y]$, and produces a better estimate of $f[x, y]$ other than smoothed $g[x, y]$.

Applying the filter $w[x, y]$, Eq. A.19 then becomes:

$$\begin{aligned}\hat{f}[x, y] &= g[x, y] * w[x, y] = (f[x, y] * h[x, y] + n[x, y]) * w[x, y] \\ \hat{F}[\xi, \eta] &= G[\xi, \eta] \cdot W[\xi, \eta] = (F[\xi, \eta] \cdot H[\xi, \eta] + N[\xi, \eta]) \cdot W[\xi, \eta]\end{aligned}\quad (\text{A.19})$$

By minimizing the total squared error ε between the recovered signal $\hat{f}[x, y]$ and the true signal $f[x, y]$ over the entire domain, as indicated in Eq. A.20

$$\varepsilon = \int_{-\infty}^{+\infty} \left| \hat{f}[x, y] - f[x, y] \right|^2 dx dy \quad (\text{A.20})$$

The Wiener filter can be derived as follows:

$$W[\xi, \eta] = \frac{H^*[\xi, \eta]}{|H[\xi, \eta]|^2 + \Gamma[\xi, \eta]}, \quad \Gamma[\xi, \eta] = \frac{|N[\xi, \eta]|^2}{|F[\xi, \eta]|^2} \quad (\text{A.21})$$

When $h[x, y]$ is small enough to be negligible, Eq. A.21 reduces to a simplified equation A.22.

$$W[\xi, \eta] = \frac{1}{1 + \frac{|N[\xi, \eta]|^2}{|F[\xi, \eta]|^2}} = \frac{1}{1 + \Gamma[\xi, \eta]} \quad (\text{A.22})$$

This transfer function defines the optimum filter for estimating the signal in uncorrelated noise under the criterion of minimum mean-squared error (Easton 2005).

Appendix B: Sampling techniques in astronomical imaging

In the imaging applications of astronomy, due to the special observing conditions, such as extremely weak illumination, long integration time, hard radiation effect, etc, it requires not only high-quality imaging instruments, but some specialized readout techniques to achieve the targeted image quality. Three sampling techniques are commonly used in astronomy applications, i.e. correlated double sampling (CDS), Fowler sampling, and up-the-ramp sampling. The details of these techniques are described in the follow sections.

B.1 Correlated double sampling

Correlated double sampling is a nondestructive readout technique that is widely used to remove the reset noise in image detectors. During the sampling, the pixel array is first reset to the bias level b . After reset, the array is read out once immediately. This first read gives the pedestal level p . After an exposure time Δt , the array is read out once again, which provides an estimate of the signal level s . Therefore, Δt is given by the time difference between the start of the read of the pedestal p and the start of the read of the signal level s . The values of individual readouts usually are in units of digital counts (DN). The net source counts over the integration Δt is obtained by the difference between these two levels.

$$S_{net} = s - p \tag{D.1}$$

The estimated source flux I in DN s^{-1} , which includes the contribution from the object, dark current, background, and sky, is then given by

$$I = \frac{S_{net}}{\Delta t} = \frac{s - p}{\Delta t} \quad (\text{D.2})$$

As both the pedestal and signal levels are referenced to the same reset bias, reset noise is mostly removed.

B.2 Fowler sampling

Fowler sampling, also called multiple correlated double sampling, is used in imaging detectors with nondestructive readout to reduce read noise. In a Fowler-N sampling, the array is first read out N times immediately after the reset. These N reads give the mean pedestal level \bar{p} . After an exposure time Δt , the array is read out N times again, which provides an estimate of the mean signal level \bar{s} . Therefore, Δt is given by the time difference between the start of the first read of the pedestal p_1 and the start of the first read of the signal level s_1 . Figure D.1 below illustrates the readouts during the exposure. The values of individual readouts usually are in units of digital counts (DN). The net source counts for the N nondestructive readouts over the integration time Δt is given by

$$S_{net} = \frac{1}{N} \sum_{i=1}^N s_i - \frac{1}{N} \sum_{i=1}^N p_i = \frac{1}{N} \sum_{i=1}^N (s_i - p_i) \quad (\text{D.3})$$

The estimated source flux I in DN s^{-1} , is then obtained by dividing the integration time

$$I = \frac{S_{net}}{\Delta t} = \frac{1}{N\Delta t} \sum_{i=1}^N (s_i - p_i) \quad (\text{D.4})$$

Since Fowler sampling is an extension of the double correlation sampling, the reset noise is removed. In addition, Fowler and Gatley (1990) shows that the read noise σ_{rd} can be reduced to $\frac{\sigma_{rd}}{\sqrt{N}}$.

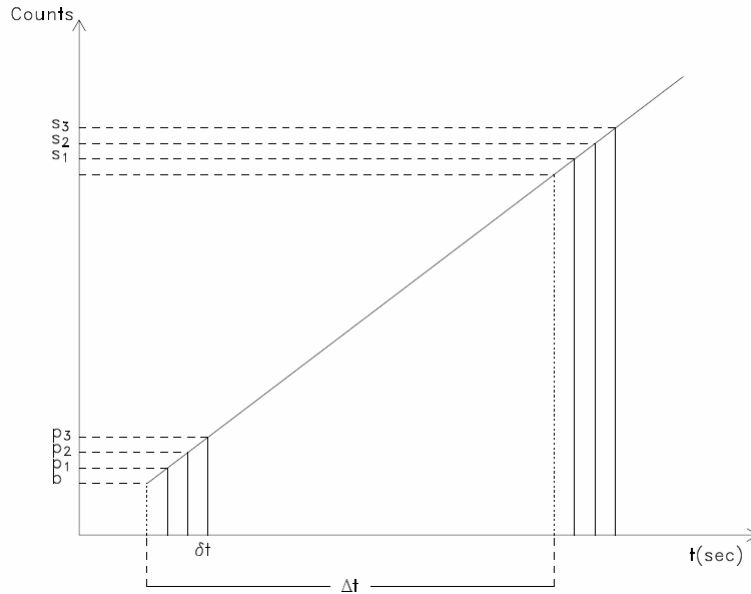


Figure D.1 Schematic of the signal recorded by an integrating node as a function of time with Fowler sampling ($N=3$).

B.3 Up-the-ramp sampling

Up-the-ramp sampling is a nondestructive readout technique with continuous sampling during the exposure. It also refers to the line-fitting readout mode. In this technique, the array is read out repeatedly over the integration time, where each read is obtained at

equally spaced time intervals throughout the entire exposure time, as indicated in Figure D.2. The read values are then fit linearly and the slope gives a measurement of the source flux. For N equally-spaced reads, each of duration δt , during an exposure time Δt , the slope can be expressed as follows.

$$I = \frac{\sum_{i=1}^N s_i \left(i - \frac{N+1}{2} \right)}{a}, a = \frac{N(N+1)\Delta t}{12} \quad (\text{D.5})$$

The up-the-ramp sampling technique is an efficient approach to reject cosmic rays and preserve the structure and photometric quality of the imaging object to well within the measurement error. It is valuable for space-based observatories which are exposed to high-energy radiation environments. Also, the readout noise is reduced to $\sqrt{\frac{6}{N}}\sigma_{rd}$

(Offenberg et al. 2001).

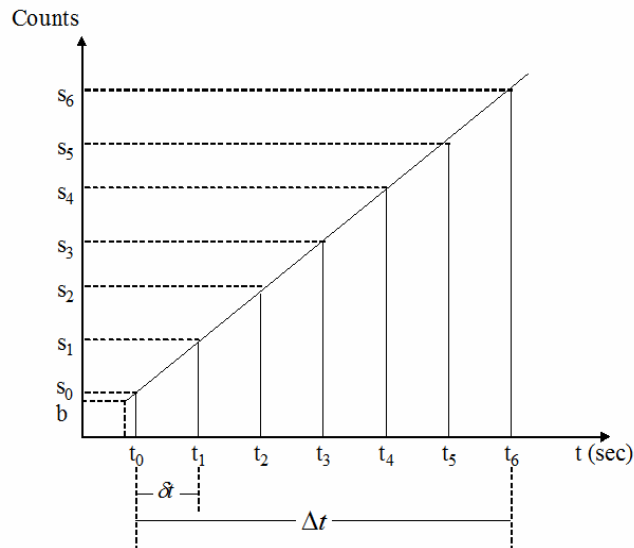


Figure D.2 Schematic of the signal recorded by an integrating node as a function of time with the up-the-ramp sampling.

Bibliography

Y. Bai, S. G. Bernd, and J. R. Hosack, et al., *Hybrid CMOS Focal plane array with extended UV and NIR response for space applications*, SPIE 48th annual meeting, San Diego, 2003.

Y. Bai, M. C. Farris, A. K. Petersen, et al., *Inter-pixel capacitance in fully-depleted silicon hybrid CMOS focal plane arrays*, Proc. SPIE, 6690, 669004, 2007.

M. G. Brown, M. Schubnell, and G. Tarle, *Correlated noise and gain in unfilled and epoxy underfilled hybridized HgCdTe detectors*, PASP, 118, 1443, 2006.

M. G. Brown, *Development of NIR detectors and science requirements for SNAP*, Ph.D. Thesis, the University of Michigan, 2007.

R. Bruggemann, C. Main, and S. Reynolds, *Depth profiling in amorphous and microcrystalline silicon by transient photoconductivity techniques*, J. Phys.: Condens. Matter, 14, 6909, 2002.

M. Caccia, S. Borghi, R. Campagnolo, et al, *Characterisation of hybrid pixel detectors with capacitive charge division*, 5th intl. Linear Collider Workshop, 2001.

R. J. Dorn, S. Eschbaumer, G. Finger, et al., *A CMOS visible silicon imager hybridized to a Rockwell 2RG multiplexer as a new detector for ground based astronomy*, Proc. SPIE, 6276, 07, 2006.

R. L. Easton, *Linear Imaging Mathematics I, II*, class notes, 2005.

D. F. Figer, B. J. Rauscher, M. W. Regan, et al, *Independent testing of JWST detector prototypes*, Proc. SPIE, 5167, 270, 2004.

G. Finger, J. Beletic, R. Dorn, et al., *Conversion gain and interpixel capacitance of CMOS hybrid focal plane arrays*, Scientific Detectors for Astronomy 2005, pp. 477-490, 2005.

G. Finger, R. Dorn, M. Meyer, et al, *Interpixel capacitance in large format CMOS hybrid arrays*, Proc. SPIE, 6276, 62760F, 2006.

G. Finger and J. W. Beletic, *Review of the state of infrared detectors for astronomy in retrospect of the June 2002 Workshop on Scientific Detectors for Astronomy*, Instrument Design and Performance for Optical/Infrared Ground-based Telescopes, Proc. SPIE, 4841, 839, 2003.

A. M. Fowler and I. Gatley, *Demonstration of an algorithm for read-noise reduction in infrared arrays*, ApJ, 353, L33, 1990.

D. Groom, *Cosmic rays and other nonsense in astronomical CCD imagers*, Experimental Astronomy, 14, 45, 2002.

B. J. Hanold and D. F. Figer, *Internal report on IPC measurement by changing V_{reset}* , Rochester Image Detector Laboratory, 2007

C. W. Helstrom, *Image restoration by the method of least squares*, J. Opt. Soc. Am, 57, 297, 1967.

S. B. Howell, *Handbook of CCD Astronomy*, Cambridge University Press, 2000.

T. H. Hsu, Y. K. Fang, C. Y. Lin, et al., *Light guide for pixel crosstalk improvement in deep submicron CMOS image sensor*, Electron Device Letters, IEEE, 25 (1), 22, 2004.

T. H. Hsu, Y. K. Fang, D. N. Yaung, et al., *Color mixing improvement of CMOS image sensor with air-gap-guard ring in deep-submicrometer CMOS technology*, Electron

Device Letters, IEEE, 26 (5), 301, 2005.

J. R. Janesick, *Charge coupled CMOS and hybrid detector arrays*, Proc. SPIE 5167, 1, 2003.

J. R. Janesick, *Scientific Charge-Coupled Devices*, SPIE Press monograph, Bellingham, Washington, 2001, (Chapter 2.2.10.2 “*Shutterless photon transfer*”).

S. Kavadias, K. Misiakos, and D. Loukas, *Calculation of pixel detector capacitances through three dimensional numerical solution of the Laplace equation*, IEEE Trans. Nucl. Sci. 40(2), 397, 1994.

D. Long and J. L. Scmit, *Mercury-Cadmium Telluride and Closely Related Alloys*, vol.5 Semiconductors and Semimetals, Infrared Detectors, edited by R. K. Willardson and A. C. Beer, Academic Press, New York, pp. 175, 1970.

A. C. Moore, Z. Ninkov, and W. J. Forrest, *Interpixel capacitance in nondestructive focal plane arrays*, Proc. SPIE 5167, 204, 2004.

A. C. Moore, *Operating, testing and evaluating hybridized Silicon P-I-N Arrays*, Ph.D. Thesis, Rochester institute of technology, 2005.

A. C. Moore, Z. Ninkov, and W. J. Forrest, *Quantum efficiency overestimation and deterministic cross talk resulting from interpixel capacitance*, Optical Eng. 45, 076402, 2006.

J. D. Offenber, D. J. Fixsen, B. J. Rauscher et al., *Validation of Up-the-Ramp Sampling with Cosmic-Ray Rejection on Infrared Detectors*, PASP, 113, 240, 2001.

P. Z. Peebles Jr., *Probability, Random Variables, and Random Signal Principles*,

McGraw-Hill Science, 2000.

H. Rhodes, G. Agranov, C. Hong, et al., *CMOS imager technology shrinks and image performance*, Microelectronics and Electron Devices, IEEE Workshop on, p. 7-18, 2004.

W. Romanishin, *An Introduction to Astronomical Photometry Using CCDs*, University of Oklahoma, 2002.

L. M. Simms, D. F. Figer, B. J. Hanold, et al, *First use of a HyViSI HARG for astronomical observations*, Proc. SPIE, 6690, 66900H 2007.

S. Seshadri and D. M. Cole, *Internsal report on IPC mapping experiment*, Jet Propulsion Laboratory, 2007.

C. Sterken and J. Manfroid, *Astronomical Photometry: A Guide*, Kluwer Academic Print, 1999.

D. Stern, *Interactive Data Language*, Research Systems Inc., 1977.

V. Svorcik, J. Kralova, V. Rybka, et al, *Temperature dependence of the permittivity of polymer composites*, Polym. Sci. B: Polym. Phys. 39, 831, 2001.

A. J. Theuwissen, *Solid-State Imaging with Charge-Coupled Devices*, Springer, 1st edition, 1995.